Serviço Público Federal
Ministério da Educação
Fundação Universidade Federal de Mato Grosso do Sul

Investigação teórica de propriedades estruturais e físico-químicas de complexos de lantanídeos

Daniel Mungo Brasil

Orientador: Leandro Moreira de Campos Pinto

Campo Grande/MS

2023

Serviço Público Federal
Ministério da Educação
Fundação Universidade Federal de Mato Grosso do Sul

Investigação teórica de propriedades estruturais e físico-químicas de complexos de lantanídeos

Daniel Mungo Brasil

Tese apresentada ao Programa de Pós-Graduação em Química - Doutorado, do Instituto de Química da Fundação Universidade Federal de Mato Grosso do Sul como parte dos requisitos para a obtenção do título de Doutor em Química.

Orientador: Leandro Moreira de Campos Pinto

Campo Grande/MS

2023

Mungo Brasil, Daniel
Investigação teórica de propriedades estruturais e físico-químicas de complexos de lantanídeos / Daniel Mungo Brasil, 2023
79p. : il.

Orientador: Leandro Moreira de Campos Pinto

Tese (Doutorado)–Universidade Federal de Mato Grosso do Sul. Instituto de Química, Campo Grande/MS, 2023.

1. DFT. 2. lantanídeos. 3. espectroscopia. I. Universidade Federal de Mato Grosso do Sul. Instituto de Química. II. Título.

Serviço Público Federal
Ministério da Educação
Fundação Universidade Federal de Mato Grosso do Sul

ATA DE DEFESA DE TESE

PROGRAMA DE PÓS-GRADUAÇÃO EM QUÍMICA

DOUTORADO

Aos dezesseis dias do mês de outubro do ano de dois mil e vinte e três, às sete horas e trinta minutos, no INQUI, da Fundação Universidade Federal de Mato Grosso do Sul, reuniu-se a Banca Examinadora composta pelos membros: Leandro Moreira de Campos Pinto (UFMS), Adriana Pereira Duarte (UFMS), André Luis de Jesus Pereira (ITA), Gilberto Maia (UFMS) e Rafael Aparecido Ferreira (IFSP), sob a presidência do primeiro, para julgar o trabalho do aluno: DANIEL MUNGO BRASIL, CPF 03770884124, do Programa de Pós-Graduação em Química, Curso de Doutorado, da Fundação Universidade Federal de Mato Grosso do Sul, apresentado sob o título "Investigação teórica de propriedades estruturais e físico-químicas de complexos de lantanídeos" e orientação de Leandro Moreira de Campos Pinto. O presidente da Banca Examinadora declarou abertos os trabalhos e agradeceu a presença de todos os Membros. A seguir, concedeu a palavra ao aluno que expôs sua Tese. Terminada a exposição, os senhores membros da Banca Examinadora iniciaram as arguições. Terminadas as arguições, o presidente da Banca Examinadora fez suas considerações. A seguir, a Banca Examinadora reuniu-se para avaliação, e após, emitiu parecer expresso conforme segue:

EXAMINADOR	AVALIAÇÃO
Dr. Leandro Moreira de Campos Pinto (Interno)	Aprovado
Dra. Adriana Pereira Duarte (Interno)	Aprovado
Dr. André Luis de Jesus Pereira (Externo)	Aprovado
Dr. Gilberto Maia (Interno)	Aprovado
Dr. Rafael Aparecido Ferreira (Externo)	Aprovado
Dr. Gleison Antonio Casagrande (Interno) (Suplente)	
Dr. Onofre Salgado Siqueira (Interno) (Suplente)	

RESULTADO FINAL:

Aprovação	X
Aprovação com revisão	
Reprovação	

OBSERVAÇÕES:

Avaliar as sugestões feitas pela banca.

Nada mais havendo a ser tratado, o Presidente declarou a sessão

encerrada e agradeceu a todos pela presença.

Assinaturas:
Dr. Leandro Moreira de Campos Pinto
Presidente da Banca Examinadora

Daniel Mungo Brasil
Aluno

Documento assinado eletronicamente por **Leandro Moreira de Campos Pinto**, **Professor do Magisterio Superior**, em 16/10/2023, às 10:51, conforme horário oficial de Mato Grosso do Sul, com fundamento no § 3º do art. 4º do Decreto nº 10.543, de 13 de novembro de 2020.

Documento assinado eletronicamente por **Gilberto Maia**, **Professor do Magisterio Superior**, em 16/10/2023, às 10:53, conforme horário oficial de Mato Grosso do Sul, com fundamento no § 3º do art. 4º do Decreto nº 10.543, de 13 de novembro de 2020.

Documento assinado eletronicamente por **Adriana Pereira Duarte**, **Professora do Magistério Superior**, em 16/10/2023, às 11:03, conforme horário oficial de Mato Grosso do Sul, com fundamento no § 3º do art. 4º do Decreto nº 10.543, de 13 de novembro de 2020.

Documento assinado eletronicamente por **Rafael Aparecido Ferreira**, **Usuário Externo**, em 19/10/2023, às 08:50, conforme horário oficial de Mato Grosso do Sul, com fundamento no § 3º do art. 4º do Decreto nº 10.543, de 13 de novembro de 2020.

Documento assinado eletronicamente por **Daniel Mungo Brasil**, **Usuário Externo**, em 24/10/2023, às 17:14, conforme horário oficial de Mato Grosso do Sul, com fundamento no § 3º do art. 4º do Decreto nº 10.543, de 13 de novembro de 2020.

Documento assinado eletronicamente por **André Luis de Jesus Pereira**, **Usuário Externo**, em 25/10/2023, às 14:03, conforme horário oficial de Mato Grosso do Sul, com fundamento no § 3º do art. 4º do Decreto nº 10.543, de 13 de novembro de 2020.

A autenticidade deste documento pode ser conferida no site https://sei.ufms.br/sei/controlador_externo.php?acao=documento_conferir&id_orgao_acesso_externo=0, informando o código verificador **4393015** e o código CRC **5E6DFF16**.

COLEGIADO DE PÓS-GRADUAÇÃO EM QUÍMICA
Av Costa e Silva, s/nº - Cidade Universitária
Fone:
CEP 79070-900 - Campo Grande - MS

Agradecimentos

À minha família e amigos.

Ao Prof. Dr. Leandro Moreira de Campos Pinto pela paciência e orientação.

Aos colegas de grupo Sarah Fonseca da Silva e Lucas da Rocha Sandim.

Ao Programa de Pós-Graduação em Química do Instituto de Química da UFMS.

Ao Centro Nacional de Processamento de Alto Desempenho em São Paulo (CENAPAD–SP) pela disponibilização da infraestrutura computacional, proj669.

À Coordenação de Aperfeiçoamento de Pessoal de Nível Superior (CAPES) pela provisão da bolsa de doutorado.

Resumo

A química computacional utiliza recursos de computação para a resolução de equações matemáticas de elevado grau de complexidade que dão informações sobre as propriedades físico-químicas de sistemas multieletrônicos. Estas equações podem ser originadas da mecânica clássica, método chamado de mecânica molecular, ou da mecânica quântica, métodos *ab initio* e teoria do funcional da densidade (DFT). Este último foi escolhido para desenvolvimento do presente trabalho. A teoria DFT foi desenvolvida para cálculos de propriedades do estado fundamental e para cálculos envolvendo estados excitados se utilizada a sua extensão, a teoria do funcional da densidade dependente do tempo (TD-DFT). Estas técnicas computacionais permitem melhorar a compreensão da relação estrutura-propriedade do sistema estudado, como é o caso dos complexos de lantanídeos que são discutidos neste trabalho. Os complexos de lantanídeos possuem diversas aplicações, desde fármacos a dispositivos conversores de luz, por isso existe um grande interesse nestes materiais. Neste trabalho foram estudados cinco complexos de lantanídeos, um formado pelo íon gadolínio(III) com o ligante usnato, dois formados pelo ligante 3,5-dimetoxibenzoato monocarboxilato com os íons lantânio(III) e cério(III), um complexo de európio(III) com fenantrolina e 2-tenoiltrifluoroacetona e um complexo análogo com a fenantrolina sililada. Os cálculos foram feitos utilizando os programas Gaussian16 e ORCA 4.0.1, o funcional híbrido de troca e correlação eletrônica B3LYP e as bases def2-SVP para os átomos leves. Já para os lantanídeos foi empregada a base def2-TZVP em conjunto com o potencial efetivo de caroço adequado. Foram realizados cálculos de otimização de energia, cálculos de obtenção do espectros infravermelho e de absorção na região do ultravioleta-visível para todos os complexos. Também foram obtidas representações dos orbitais moleculares de fronteira para analisar e fazer a atribuição do espectro eletrônico. Para os cinco compostos estudados, o espectro teórico de infravermelho condiz com seu respectivo espectro experimental, o espectro de absorção apresenta um pequeno deslocamento comparados aos espectros experimentais, mas o formato das bandas são correspondentes. Os dados teóricos apresentaram boa concordância com os dados experimentais comprovando que os métodos computacionais podem ser utilizados para o entendimento da geometria, da estrutura eletrônica e na elucidação dos espectros de absorção.

Palavras-chave: DFT; TD-DFT; lantanídeos; espectroscopia

Abstract

Computational chemistry uses computational resources to solve highly complex mathematical equations to give information about the physicochemical properties of multielectronic systems. These equations originated from classical mechanics, a method called molecular mechanics, or from quantum mechanics, *ab initio* methods and density functional theory (DFT). The latter was chosen to develop the present work. DFT was developed for calculations of fundamental state properties and for those calculations involving excited states one uses its extension, the time-dependent density functional theory (TD-DFT). These computational techniques allow us to improve our understanding of the structure-property relationship, as in the case of the lanthanide complexes discussed in the present work. Lanthanide complexes have several applications, from drugs to light-converting devices, therefore there is great interest in such materials. In this work, five lanthanide complexes were studied, one formed by the gadolinium(III) ion with the usnate ligand, and two of them formed by the 3,5-dimethoxy benzoate monocarboxylate ligand with the lanthanum(III) and cerium(III) ions, a europium(III) complex with phenanthroline and 2-thenoyltrifluoroacetone and a similar complex but silylated phenanthroline. The calculations were performed using the Gaussian16 and ORCA 4.0.1 programs, the B3LYP exchange-correlation hybrid functional, and the def2-SVP basis set for light atoms. For lanthanides, the def2-TZVP basis set was used with the effective core potential. Geometry optimization and calculations for obtaining the infrared spectra and absorption of the ultraviolet-visible region were carried out for all complexes. Frontier molecular orbital diagrams were also obtained to analyze and assign the electronic spectrum. For the five studied compounds, the theoretical infrared spectra agree with the experimental spectra, the absorption spectra present a small displacement compared to the experimental spectra, but the structure of the bands matches. The theoretical data showed good agreement with the experimental data, proving that the computational methods can be used to understand the geometry and electronic structure and elucidate the absorption spectra.

Keywords: DFT; TD-DFT; lanthanides; spectroscopy

Lista de abreviaturas e siglas

acac: acetilacetonato

ala: alanina

DFT: teoria do funcional da densidade (do inglês, *density functional theory*)

DMBz: 3,5-dimetilbenzoato

ECP: potencial efetivo de caroço (do inglês, *effective core potential*)

fen: fenilalanina

hfac: hexafluoroacetilacetonato

HOMO: orbital molecular ocupado de maior energia (do inglês, *highest occupied molecular orbital*)

ILCT: transferência de carga intra-ligante (do inglês, intra-ligand charge transfer)

LED: diodos emissores de luz (do inglês, *light-emitting diode*)

LLCT: transferência de carga ligante-ligante (do inglês, ligand-ligand charge transfer)

LMCT: transferência de carga do ligante para o metal (do inglês, ligand to metal charge transfer)

Ln: lantanídeo

LUMO: orbital molecular desocupado de menor energia (do inglês, *lowest unoccupied molecular orbital*)

MOF: estruturas organometálicas (do inglês, *metal organic framework*)

phen: fenantrolina

phensi: fenantrolina sililada

ser: serina

TD-DFT: teoria do funcional da densidade dependente do tempo (do inglês, *time-dependent density functional theory*)

tta: 2-tenoiltrifluoroacetona

UV-vis: ultravioleta-visível

Lista de figuras

Lista de tabelas

Sumário

1 Introdução

1.1 Teoria do funcional da densidade

A química computacional tornou-se uma importante ferramenta para o estudo de fenômenos físico-químicos e na análise e determinação de propriedades moleculares, tais como: energia eletrônica do estado fundamental e estados excitados [1], determinação de estrutura [2], propriedades vibracionais [3], polarização magnética e elétrica [4], energia de ionização [5], afinidade eletrônica, entre outras [6]. Ela se baseia no uso de computadores para resolver equações matemáticas com elevado grau de complexidade, com aproximações para a resolução da equação de Schrödinger, que descrevem um sistema eletrônico, como átomos, moléculas ou cristais e assim acessar informações comparáveis aos resultados obtidos através de técnicas experimentais e mesmo aquelas que seriam inacessíveis de outra forma. Nos últimos 30 anos, a teoria do funcional da densidade (DFT, sigla em inglês) vem se destacando como o método mais usado nesta área [7, 8]. O desenvolvimento de *softwares* e *hardwares* mais avançados facilitou seu acesso e permitiu o estudo de sistemas cada vez mais complexos. As aplicações do DFT incluem: *design* de diodos emissores de luz (LED) [9], auxílio na racionalização de reações químicas [10], estudo de mudança de fase [11], estudo de catalisadores [12], e desenvolvimento de células solares [13].

As metodologias computacionais de primeiros princípios (*ab initio*) utilizam uma função de onda para obter a energia do sistema. A teoria DFT, porém, propõe obter a energia do sistema através da densidade eletrônica. Esta teoria é fundamentada em dois teoremas propostos por Hohenberg e Kohn (1964) [14]. O primeiro teorema propõe que as propriedades de um sistema multi-eletrônico no estado fundamental depende apenas da densidade eletrônica n(x,y,z). Então, conhecendo a densidade eletrônica qualquer propriedade pode ser obtida a partir desta. Com isso, uma grande vantagem da teoria DFT é redução da dimensionalidade do sistema. Para resolver a equação de Schrödinger empregando outros métodos, cada elétron do sistema terá três dimensões independentes, desta forma, para um cálculo da molécula de CO_2, por exemplo, seria necessário um cálculo envolvendo 66 dimensões. Ou ainda, para um composto metálico como o complexo [Eu(phen)$_3$(tta)] seriam necessárias 1470 dimensões. Usando a densidade, ao invés da função de onda, o cálculo pode ser reduzido para um sistema tridimensional.

O segundo teorema de Hohenberg e Kohn diz que a densidade eletrônica correta para um sistema no estado fundamental é aquela que minimiza sua energia total quando a energia é calculada em termos de um funcional da densidade eletrônica E[n(x,y,z)]. Este funcional descreve como a densidade varia com a energia do sistema. Este termo é obtido na formulação da teoria do funcional da densidade a partir da equação de Schrödinger.

$$E\Psi = \Psi[T(r) + V_{en}(r) + J(r)] \tag{1.1}$$

onde $T(r)$ é o termo de energia cinética, $V_{en}(r)$ é a energia de atração elétron-núcleo e $J(r)$ é a energia de repulsão elétron-elétron e r é a variável espacial. Com a formulação de Hohenberg e Kohn, a energia total do sistema pode ser equacionada como:

$$E_e[\rho(r)] = T[\rho(r)] + V_{en}[\rho(r)] + J[\rho(r)] + Q[\rho(r)] \tag{1.2}$$

onde $Q[\rho(r)]$ é a energia de interação quântica elétron-elétron devido ao princípio da exclusão de Pauli, também chamada de energia de troca. Importante ressaltar que todos os termos são dependentes da densidade eletrônica total, $\rho(r)$.

O cálculo das energias de atração elétron-núcleo (V_{en}) e a energia clássica para atração elétron-elétron (J) já eram conhecidas. Kohn e Sham [15] usaram um modelo de gás de elétrons, onde os elétrons não interagiam, para determinar $T[\rho(r)]$. A energia cinética obtida, então, não considerava a interação entre elétrons, mas pode ser determinada de maneira exata e um termo de correção passa a ser necessário. A combinação deste termo de correção da energia cinética, chamado de energia de correlação, com a interação quântica elétron-elétron $Q[\rho(r)]$ dá origem ao funcional de troca e correlação eletrônica [16]:

$$E_{xc} = [T[\rho(r)] - T_s[\rho(r)]] + Q[\rho(r)] \tag{1.3}$$

E a equação final fica:

$$E_e[\rho(r)] = T[\rho(r)] + V_{en}[\rho(r)] + J[\rho(r)] + E_{xc} \tag{1.4}$$

Porém, a forma exata de E_{xc} não é conhecida, ou seja, não sabemos qual equação o representa. Desta maneira, uma série de funcionais de troca e correlação eletrônica foram e têm sido criados visando uma boa aproximação das propriedades calculadas quando comparadas às propriedades obtidas experimentalmente. A escolha do funcional depende do sistema a ser estudado e é auxiliada pela literatura, já que ainda não existe um funcional versátil o suficiente que funcione para todas as situações. Para realizar um cálculo baseado na teoria DFT, primeiramente devemos escolher um programa computacional. Existem vários disponíveis, por exemplo: ORCA, NWChem, ADF, Gaussian, Psik, Molcas, Molpro e muitos outros, tanto livres quanto comerciais. Com o programa definido, são fornecidas as informações básicas necessárias para que este possa realizar os cálculos:

- estrutura inicial da molécula – composta pela localização espacial de cada átomo, podendo ser simplesmente pontos no espaço cartesiano (x,y,z)

- funcional de troca e correlação eletrônica, solicitado através de um código, por exemplo: BLYP, B3LYP, PBE, M06
- função de base (*basis set*), a qual descreve os orbitais atômicos, por exemplo: def2-SVP, 6-311G, cc-pVTZ
- carga e multiplicidade do composto
- propriedade a ser calculada

Um exemplo de *input*, arquivo de entrada contendo as informações necessárias para o início do cálculo, para o programa ORCA está representado na Figura 1. Mais comandos podem ser fornecidos, como aumentar a precisão do cálculo ou até mesmo diminuir a precisão, se o cálculo inicial não obter êxito na convergência dos parâmetros estabelecidos. No início do cálculo o programa irá executar a otimização da geometria, ou a minimização da energia. Esta etapa é necessária para a determinação da estrutura química do estado fundamental. Será calculada a energia eletrônica da estrutura fornecida e então pequenas modificações nas posições dos átomos serão feitas por um algoritmo e a energia será calculada novamente, quando se obter uma estrutura de menor energia esta é salva e o processo se repete até a minimização da energia total do sistema. A Figura 2 mostra um gráfico obtido a partir deste processo de otimização usando como exemplo a molécula de fenol. Cada ponto do gráfico representa uma estrutura, já o eixo y apresenta a variação de energia. A obtenção da estrutura do estado fundamental, porém, deve ser verificada já que existe a possibilidade de a estrutura encontrada ser um mínimo local e não um mínimo global. Isto é feito com o cálculo das frequências vibracionais (espectro de infravermelho), em que pelo menos uma frequência negativa indica um estado transitório ou virtual. Se isto acontecer, é necessário realizar pequenas modificações na última estrutura obtida até que seja possível determinar o mínimo global.

1.2 Teoria do funcional da densidade dependente do tempo

A teoria DFT só pode ser usada para cálculos no estado fundamental, mas ela pode ser estendida para a teoria do funcional da densidade dependente do tempo (TD-DFT, sigla em inglês), a qual permite o estudo de estados excitados. Com cálculos baseados na teoria TD-DFT é possível fazer determinação da geometria de estados excitados, acoplamento vibrônico, estrutura de transição de uma reação química, transferência de cargas, de espectros de absorção no ultravioleta-visível, infravermelho, raman, ressonância magnética nuclear e outros [17].

O uso mais comum da teoria TD-DFT é a modelagem do espectro de absorção molecular [18]. A utilização de métodos computacionais nos permite uma melhor compreensão da relação estrutura-propriedade ao analisar como a energia dos orbitais e a forma

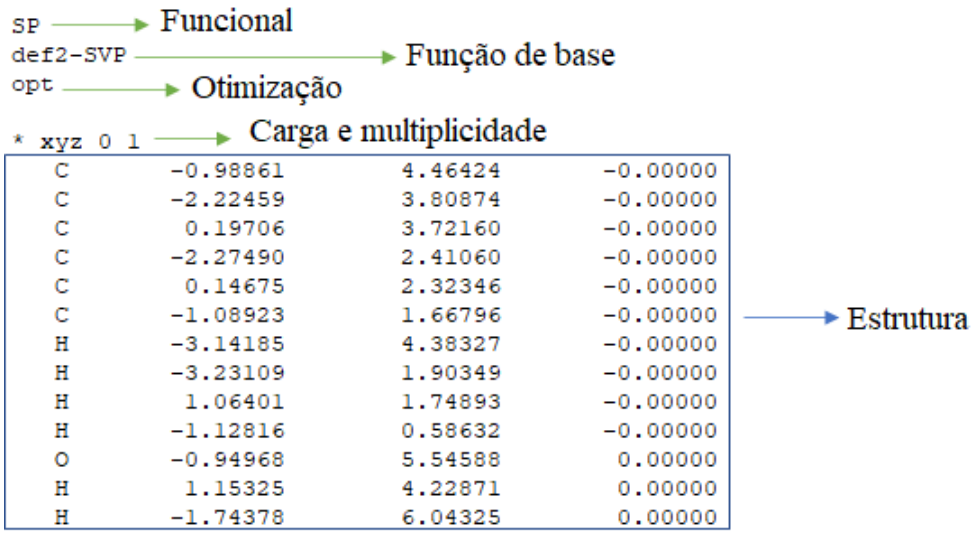

Figura 1 – Exemplo de *input* com os parâmetros básicos para o cálculo de otimização da estrutura de uma molécula de fenol.

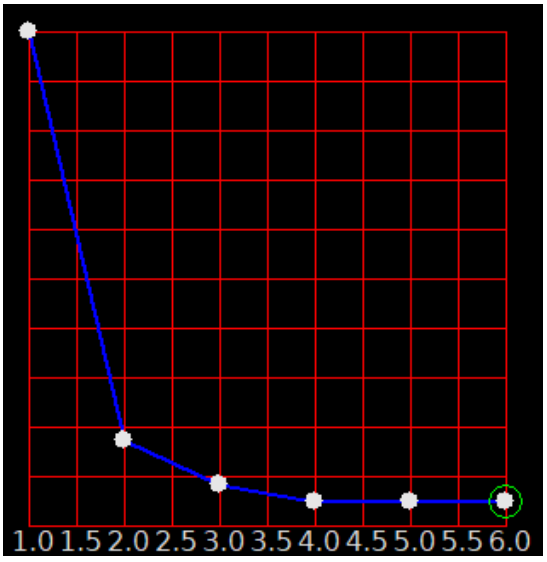

Figura 2 – Exemplo de gráfico de energia *versus* número de interações obtido a partir da otimização de geometria de uma molécula de fenol. Cada interação representa um ciclo do processo de otimização.

do espectro muda em relação à pequenas alterações na estrutura molecular. Como por exemplo, determinando a localização do orbital HOMO (*highest occupied molecular orbital*) e do orbital LUMO (*lowest unoccupied molecular orbital*) pode-se pensar na inclusão de grupos doadores ou receptores de elétrons e determinar como eles irão afetar o formato do espectro e a energia dos orbitais de fronteira.

As diferentes transições eletrônicas de interesse em cálculos de absorção estão esquematizadas na Figura 3. A excitação de um elétron no mínimo do estado fundamental (na ausência de vibrações) para um estado excitado é chamada de uma absorção vertical (ΔE_{vert}). A transição adiabática, ΔE_{ad}, é a transição entre os dois estados em seus

respectivos mínimos. Já a transição 00 (zero-zero) é a transição do elétron entre os pontos de mínimo vibracional, energia de ponto 0 (ΔE^{ZP}), entre os dois estados. O espectro de absorção pode ser descrito somente pelas energias de transição vertical ou pelas transições 00, que inclui a transição adiabática [18]:

$$\Delta E_{00} = \Delta E_{\mathrm{ad}} + \Delta E^{\mathrm{ZP}} \tag{1.5}$$

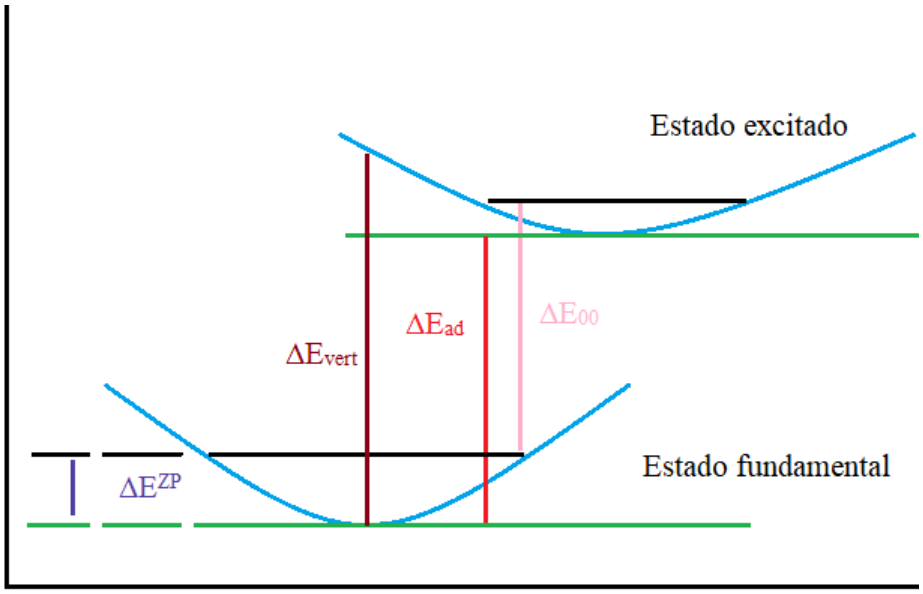

Figura 3 – Esquema representando o processo de absorção na região do ultravioleta-visível.

O espectro obtido pela energia 00 fornece uma melhor comparação com o experimento já que não existe um experimento equivalente à obtenção da energia vertical, mas devido a erros numéricos e dificuldades da implementação deste método em TD-DFT, a energia vertical ainda é muito usada e fornece bons resultados, principalmente quando a intenção é a comparação de estruturas semelhantes em busca de tendências na alteração estrutural [17].

O primeiro passo para se executar um cálculo baseado na teoria TD-DFT é ter a estrutura teórica do estado fundamental obtida por cálculos DFT no mesmo nível de teoria, com o mesmo funcional de troca e correlação eletrônica, mesma função de base e parâmetros de correção.

A seguir será apresentada a classe de compostos objeto de estudo no presente trabalho.

1.3 Lantanídeos

Compostos de lantanídeos apresentam propriedades espectroscópicas únicas, as quais são provenientes das transições f-f, tais como: alto deslocamentos de Stokes, emissões

finas, que podem ir do ultravioleta ao infravermelho próximo e longo tempo de vida [19, 20]. Estas propriedades são explicadas pela distribuição radial dos orbitais $4f$ em relação aos orbitais $5s$ e $5p$, e suas densidades eletrônicas se estendem mais pelo espaço resultando na blindagem dos orbitais $4f$ em elação ao ambiente químico, mesmo eles sendo os orbitais de valência. Uma grande dificuldade neste tipo de composto é encontrar uma forma de aumentar a intensidade da emissão dos íons de lantanídeos já que as transições f-f são proibidas pela regra de seleção de paridade de LaPorte [21, 22]. Uma forma de contornar este problema é utilizar o efeito antena, em que um cromóforo é usado para absorver radiação e transferir a energia para um estado excitado do lantanídeo o que tornará a emissão parcialmente permitida [23]. Conforme demonstrado na Figura 4, o ligante é excitado para o nível singleto (S_1), e neste nível ele pode decair ao tripleto (T) ou transferir energia para o nível $^5D_4$ do Eu^{3+}, que posteriormente decai de forma não radiativa para o $^5D_1$ e depois para o nível $^5D_0$, onde finalmente o relaxamento radiativo (emissão de fóton) pode ocorrer.

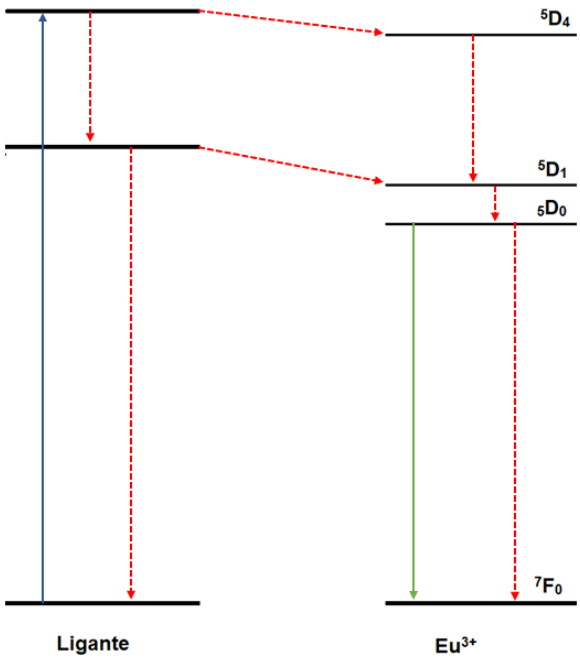

Figura 4 – Diagrama que representa os níveis de energia de um complexo de Eu^{3+} demonstrando o efeito antena.

Fonte: Adaptado de [19].

Estas características conferem aos lantanídeos diversas possibilidades de aplicações como sensores, sondas biológicas, em telecomunicações e outras [22]. Complexos de lantanídeos também são candidatos promissores para serem usados como LED: Shi et al. [24] sintetizou complexos de Nd^{3+}, com ácidos amino-carboxílicos, para serem usados como LEDs. O ácido octanoico foi modificado com aminos ácidos, DL-fenilalanina, DL-alanina e DL-serina resultando em três complexos: Nd(octo-fen), Nd(octo-ala) e Nd(octo-ser), respectivamente. Através dos espectros de emissão com excitação em 380 nm, o complexo Nd(octo-fen) foi o que apresentou maior intensidade. A análise de estabilidade térmica

avaliou a mudança da intensidade da luminescência em função da temperatura, avaliação importante para o uso como LEDs já que a temperatura de uso pode chegar a 150°C. Os três complexos apresentaram um comportamento satisfatório, sendo observado inclusive aumento de intensidade com o aumento da temperatura. Por fim, os autores identificaram o Nd(octo-fen) com um grande potencial para ser usado como diodo emissor de luz.

Outra área promissora é a conversão de energia solar. A eficiência da conversão de luz solar em energia nas células solares usadas atualmente fica em torno de 24%, isto ocorre por que o material utilizado absorve apenas parte da radiação emitida pelo sol. A função dos complexos de lantanídeos é de absorver essa radiação não aproveitada pelas células convencionais e convertê-la, através do processo de emissão, em radiação com um comprimento de onda que possa ser aproveitada na conversão de energia [24, 25].

Quando usados como sondas biológicas, os complexos de lantanídeos apresentam vantagens sobre moléculas orgânicas se aplicados como sensores químicos em matriz biológica. Por apresentarem maiores deslocamento de Stokes, evitam sua auto-excitação; fenômeno comum nas moléculas orgânicas [26]. Outra vantagem é a rápida transferência de energia do ligante para o íon lantanídeo evitando o foto-branqueamento, fenômeno onde ocorre a degradação do fluoróforo pela ação da luz [27]. Como o meio biológico também é luminescente ele pode causar interferência na medida. Muitas vezes é difícil diferenciar a emissão da sonda e do próprio meio, por possuírem maior tempo de vida, os complexos de lantanídeos ajudam a contornar este problema. Um intervalo de tempo pode ser definido entre o pulso de excitação e a leitura do sinal obtido, já que o tempo de vida da emissão das moléculas orgânicas é pequeno, e quando a leitura é feita, as moléculas orgânicas já voltaram para o estado fundamental. Estes sensores luminescentes podem ser usados em detecções de cátions como Al^{3+}, Zn^{2+}, Hg^{2+}, Pb^{2+}, e Co^{2+} [28, 29], ânions (I^-, Cl^-, Br^-,) [30–33] e moléculas orgânicas complexas (como os ácidos nucleicos) [26].

Diversos trabalhos têm sido reportados na literatura com a utilização da química computacional no estudo de complexos de lantanídeos, alguns deles serão discutidos a seguir. Shurygin et al. [34] estudaram uma série de complexos dos lantanídeos Ce(III), Nd(III), Eu(III) e Er(III) de fórmula geral $[Ln(NO_3)_3(phen)_2]$, onde phen representa o ligante 1,10-fenantrolina. Os complexos foram sintetizados e caracterizados por difração de raios-X e espectroscopia de absorção. A estrutura determinada foi usada como ponto de partida para os cálculos de otimização de geometria com a teoria DFT, que então foi submetida a cálculos baseados na teoria TD-DFT para a determinação da estrutura eletrônica para auxiliar na interpretação dos dados espectroscópicos. A partir dos dados obtidos, os autores previram que o único complexo que apresentara luminescência era o $[Eu(NO_3)_3(phen)_2]$, por apresentar o estado de tripleto dos ligantes próximos à região do estado $^5D_{0-3}$, para os quais a energia é transferida no efeito antena. O efeito antena também é favorecido pelo aumento do número de estados excitados devido à ligação com

o ligante 1,10-fenantrolina. O complexo de cério não apresenta luminescência uma vez que seus níveis de energia estão distantes dos estados excitados dos ligantes. E os complexos de érbio e neodímio tem a energia do estado excitado dissipada por múltiplas transições não radiativas.

Shurygin et al. [35] estudaram a influência da modificação estrutural de ligantes na estrutura eletrônica de complexos de európio. Os complexos [Eu(acac)$_3$(phen)] e [Eu(hfac)$_3$(phen)] foram comparados. A diferença entre as estruturas se dá pela substituição do grupo acetilacetonato (acac) por hexafluoroacetilacetonato (hfac). A substituição do grupo CH_3 em acac por CF_3 em hfac resulta em um decréscimo das energias dos orbitais moleculares do ligante 1,10-fenantrolina (phen), e um aumento da energia dos orbitais moleculares delocalizados nos sítios de complexação. Outra diferença é a energia do HOMO dos dois complexos, 5,28 eV para o [Eu(acac)$_3$(phen)] e 7,40 eV para o [Eu(hfac)$_3$(phen)]. Isto é explicado através dos dados de composição dos orbitais moleculares: para o complexo [Eu(hfac)$_3$(phen)] há a participação tanto de phen e de hfac para a formação do HOMO, enquanto que para o complexo [Eu(acac)$_3$(phen)] não há a participação de acac para a formação deste orbital molecular. A formação dos complexos também diminui a diferença HOMO-LUMO de phen, este decréscimo contribui para o fenômeno da luminescência.

Raymond e colaboradores [36] analisaram os complexos de Sm(III) e Eu(III) com 3,4,3-tetraazatetradecano(1,2-hidroxipiridinona) com o objetivo de estudar os estados excitados dos dois cromóforos deste ligante, (NH-1,2-hidroxipiridinona) e (N-1,2-hidroxipiridinona). Ao comparar os espectros de absorção e excitação experimentais com os cálculos teóricos, foi verificado que o cromóforo que absorve em região de maiores comprimentos de onda é melhor para a sensibilização do íon Eu(III). Através da análise dos orbitais moleculares é possível determinar quais deles estão envolvidos em cada transição eletrônica e então agrupá-los de acordo com os comprimentos de onda envolvidos na absorção de radiação.

2 Objetivos

2.1 Objetivo geral

Este trabalho tem como objetivo geral o estudo teórico de complexos de lantanídeos correlacionando a estrutura com as propriedades espectroscópicas para melhor entendimento dos resultados experimentais.

2.2 Objetivos específicos

Sendo assim, os objetivos específicos deste trabalho são:

- Estudar um complexo de gadolínio com o ânion usnato para determinação estrutural e para auxiliar na interpretação do espectro de infravermelho e de absorção, correlacionando as bandas com as transições eletrônicas envolvidas
- Estudar complexos de lantânio e de cério com o ânion 3,5-dimetoxibenzoato para determinação da estrutura otimizada, com comparação com a estrutura obtida pela técnica de difração de raios-X e refinada pelo método de Rietveld, e estudo dos espectros de infravermelho e de absorção
- Estudar complexos de európio com os ligantes fenantrolina e 2-tenoiltrifluoroacetona e um complexo análogo com a fenantrolina sililada. Realizar comparações entre os espectros de absorção teóricos e analisar as transições eletrônicas

3 Metodologia

Os cálculos apresentados neste trabalho foram realizados em computadores do Centro Nacional de Processamento de Alto Desempenho em São Paulo (CENAPAD–SP) localizado em Campinas/SP. Os cálculos foram realizados com os programas ORCA 4.0.1 [37] e Gaussian16 [38] e foram analisados utilizando os programas de visualização Avogadro (versão 1.2.0) [39] e Gabedit (versão 2.5.1) [40]. A sugestão inicial das estruturas foi desenhada no Avogadro e, então, esta estrutura foi submetida a um cálculo de otimização de geometria. Com o êxito deste passo, a estrutura obtida era usada para cálculos de frequência (espectro de infravermelho), absorção, e obtenção das imagens dos orbitais importantes para as transições eletrônicas.

3.1 Complexos de ácido úsnico e gadolínio

Os cálculos foram realizados utilizando o funcional híbrido de troca e correlação eletrônica B3LYP [41, 42]. Este funcional é um dos mais populares para cálculos baseados na teoria DFT e apresenta resultados satisfatórios para diversos sistemas. Para os átomos leves (C, H e O) optou-se pela função de base def2-SVP [43] e para o átomo de Gd foi escolhida a função de base def2-TZVP [43], em conjunto com o potencial efetivo de caroço (ECP/MBW53) [44]. Levando em consideração que os orbitais $4f$ não participam significativamente das ligações químicas, o método ECP trata explicitamente somente os oito elétrons mais difusos, enquanto o restante é tratado como um núcleo iônico (caroço) paralisado. A frequência e as energias verticais de transição foram calculadas por TD-DFT no mesmo nível de teoria.

3.2 Complexos de 3,5-dimetoxibenzóico monocarboxilato de cério e lantânio

Complexos de cério e lantânio com o ligante carboxilado 3,5-dimetilbenzoato (DMBz) foram obtidos e caracterizados pelo Grupo do Professor Cláudio Teodoro de Carvalho (UFGD). A partir de estruturas resolvidas pelo método Rietveld, cálculos baseados na teoria DFT de otimização de geometria, infravermelho e absorção foram realizados. O funcional de troca e correlação eletrônica escolhido foi o funcional híbrido B3LYP em conjunto com a função de base def2-SVP para os átomos leves (C, O, e H) e a função de base def2-TZVP para os lantanídeos, com o ECP (MBW28) para o La [44] e (MBW47) para o Ce [44, 45]. Após as otimizações, as estruturas foram confirmadas através

do cálculo vibracional. Os cálculos de otimização de infravermelho foram realizados no pacote Gaussian16 e os cálculos de absorção foram realizados no pacote ORCA 4.0.1.

3.3 Complexos de fenantrolina e fenantrolina sililada

A metodologia utilizada é a mesma apresentada na seção 3.1. Os cálculos de ambos os complexos foram realizados utilizando o funcional de troca e correlação eletrônica híbrido B3LYP. Para os átomos leves (C, H ,O, N, F e Si) foi utilizada a função de base def2-SVP e para o lantanídeo, Eu, foi utilizada a função de base def2-TZVP em conjunto com o potencial efetivo de caroço (ECP/MBW53). A frequência e as energias verticais de transição foram calculadas por TD-DFT no mesmo nível de teoria.

4 Resultados e discussão

4.1 Complexos de ácido úsnico e gadolínio

Nesta seção é apresentado o estudo publicado no periódico *Inorganica Chimica Acta*, intitulado *New complexes of usnate with lanthanides ions: La(III), Nd(III), Tb(III), Gd(III), synthesis, characterization, and investigation of cytotoxic properties in MCF-7 cells*. O artigo pode ser encontrado nos ANEXOS.

Um complexo de lantanídeo do isômero (R+) de ácido úsnico foi estudado a fim de se obter a estrutura teórica, assim como os espectros de infravermelho e absorção, e as respectivas transições eletrônicas envolvidas. O ácido úsnico (ver representação na Figura 5) é uma substância extraída de líquens. Este ácido e os íons lantanídeos têm sido reportados como compostos que apresentam atividade anticancerígena [46]. Uma série de complexos do ânion usnato (L) com lantanídeos foram sintetizados experimentalmente e o complexo de gadolínio foi escolhido para ser estudado com o emprego de métodos computacionais. Ao longo do trabalho será utilizada a letra "L" para designar os ligantes.

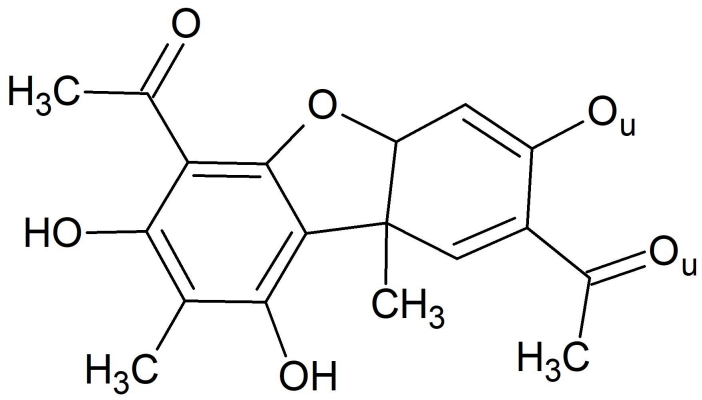

Figura 5 – Representação bidimensional da estrutura do ácido úsnico.

A geometria otimizada mostra que o íon de gadolínio é coordenado por seis átomos de oxigênio do ligante (O_u) e dois átomos de oxigênio de duas moléculas de água (O_a). A distância média da ligação $Gd-O_u$ é de 2,36 Å e $Gd-O_a$ é de 2,540 Å. A Figura 6 mostra a estrutura do otimizada obtida para o complexo $[GdL_3(H_2O)_2]$.

A estrutura teórica foi comparada com poliedros ideais que representam as seguintes geometrias: *bicapped* prisma trigonal, dodecaedro trigonal e anti-prisma quadrado no *software* SHAPE 2.1. Com este programa é possível fazer uma comparação da estrutura fornecida com poliedros ideais e, desta forma, é gerado o desvio médio para cada geometria. Esta análise revelou que a geometria mais provável para o complexo $[GdL_3(H_2O)_2]$ é o

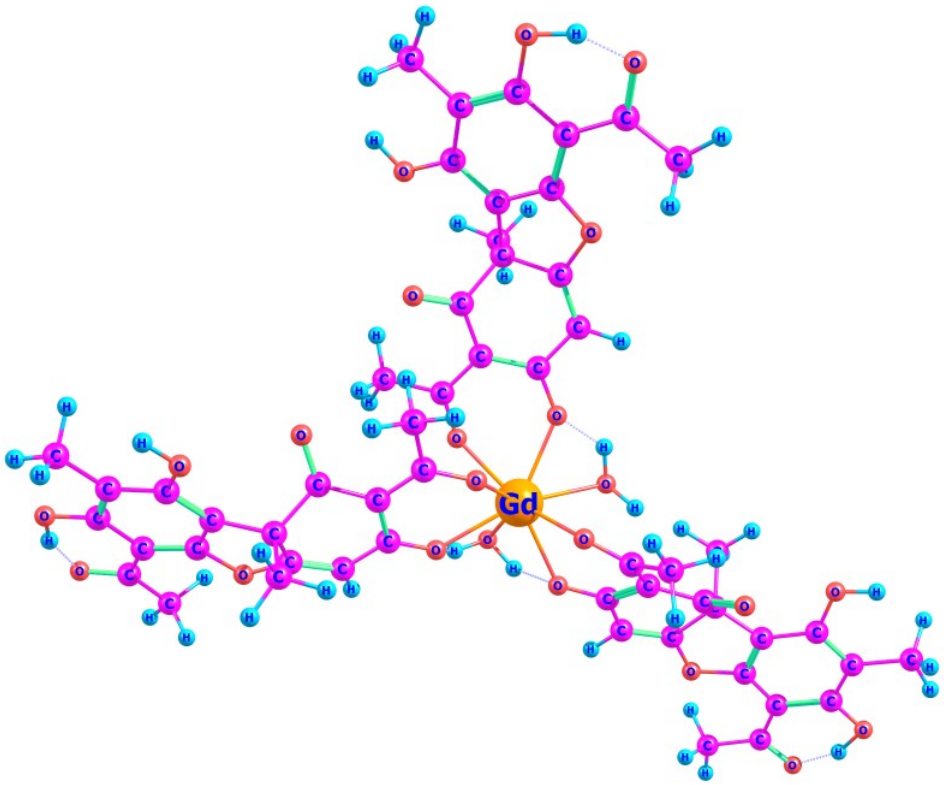

Figura 6 – Estrutura otimizada do complexo $[GdL_3(H_2O)_2]$.
Legenda: laranja (gadolínio); rosa (carbono); azul (hidrogênio); e vermelho (oxigênio).

anti-prisma quadrado distorcido. A Tabela 1 apresenta algumas distâncias de ligação e ângulos selecionados para a estrutura otimizada do complexo.

Tabela 1 – Comprimentos e ângulos de ligação selecionados da estrutura teórica do complexo $[Gd_3(H_2O)_2]$.

comprimento de ligação (Å)	
O(1)−Gd(III)	2,346
O(2)−Gd(III)	2,380
O(3)−Gd(III)	2,322
O(4)−Gd(III)	2,430
O(5)−Gd(III)	2,362
O(6)−Gd(III)	2,311
ângulo de ligação (graus)	
O(1)−Gd(III)−O(2)	68,4
O(3)−Gd(III)−O(4)	68,1
O(5)−Gd(III)−O(6)	69,2

Os espectros de infravermelho teórico e experimental são mostrados na Figura 7 e as atribuições estão presentes na Tabela 2. Os espectros experimental e teórico têm boa correspondência (considerado dentro do erro esperado para a metodologia empregada) com a maior diferença sendo na região de 4000 a 2800 cm^{-1}. No espectro experimental essa região apresenta uma banda larga enquanto no espectro teórico se observa seis bandas

finas e bem resolvidas. Isto ocorre porque no espectro teórico o cálculo é feito baseado em apenas uma molécula de complexo no estado gasoso, não estando presentes então efeitos intermoleculares como as ligações de hidrogênio, o que também explica a diferença de energia de uma das bandas do grupo OH.

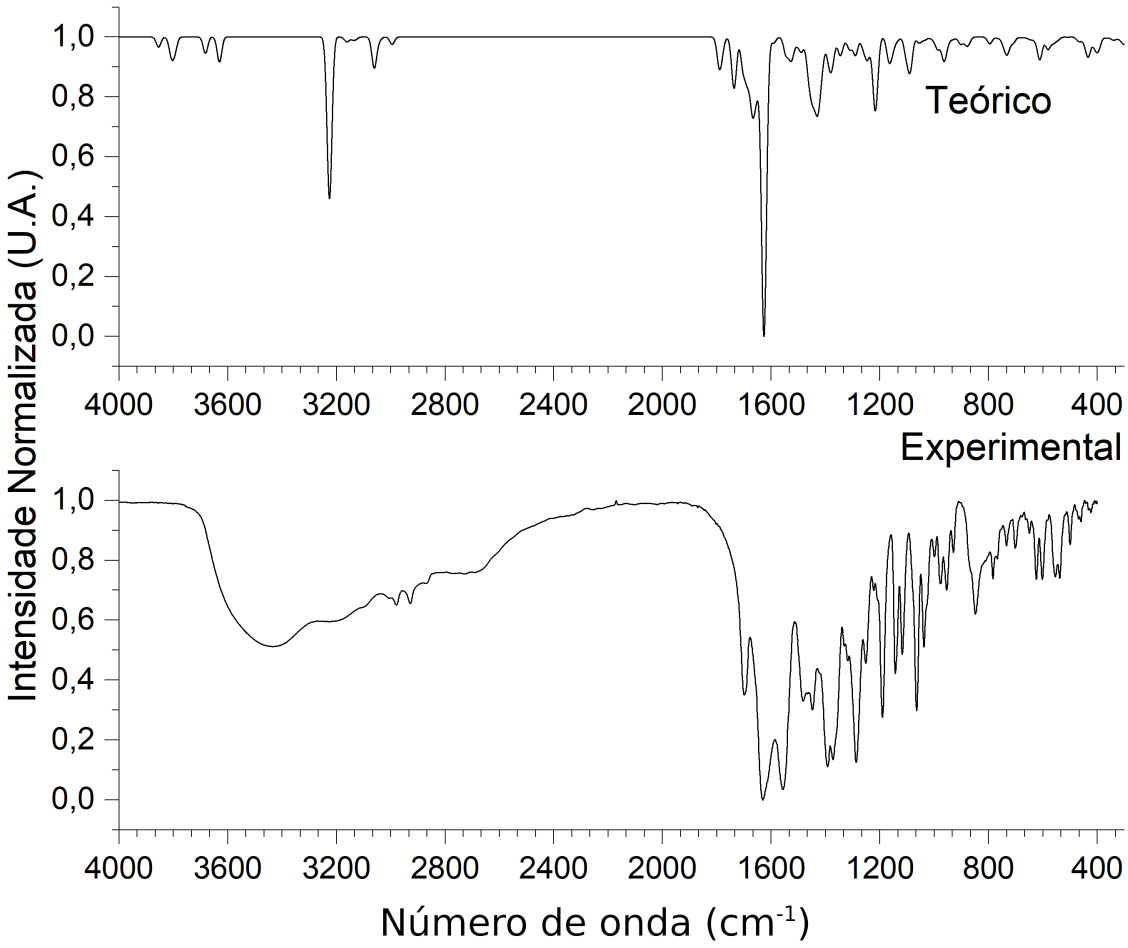

Figura 7 – Comparação dos espectros de infravermelho teórico e experimental do complexo $[GdL_3(H_2O)_2]$.

Tabela 2 – Atribuição dos espectros de infravermelho experimental e teórico para o complexo $[Gd_3(H_2O)_2]$.

atribuição	experimental (cm^{-1})	teórico (cm^{-1})
OH (água)	3448	3854
OH	3189	3223
OH	2731	3802
C=O	1064	1062
C=O	1700	1703
C=O	1631	1629
C=O	1557	1780
Gd−O	–	405

A Figura 8 mostra os espectros teórico e experimental de absorção para o complexo $[GdL_3(H_2O)_2]$. Novamente, no espectro teórico, as bandas são bem mais resolvidas,

permitindo ter uma melhor clareza das transições que ocorrem. Enquanto o espectro experimental apresenta uma banda larga, no espectro teórico quatro bandas são perceptíveis. Isto ocorre porque no cálculo do espectro teórico cada transição é tratada individualmente. Na Tabela 3 são apresentadas as atribuições das transições eletrônicas envolvidas neste espectro de absorção.

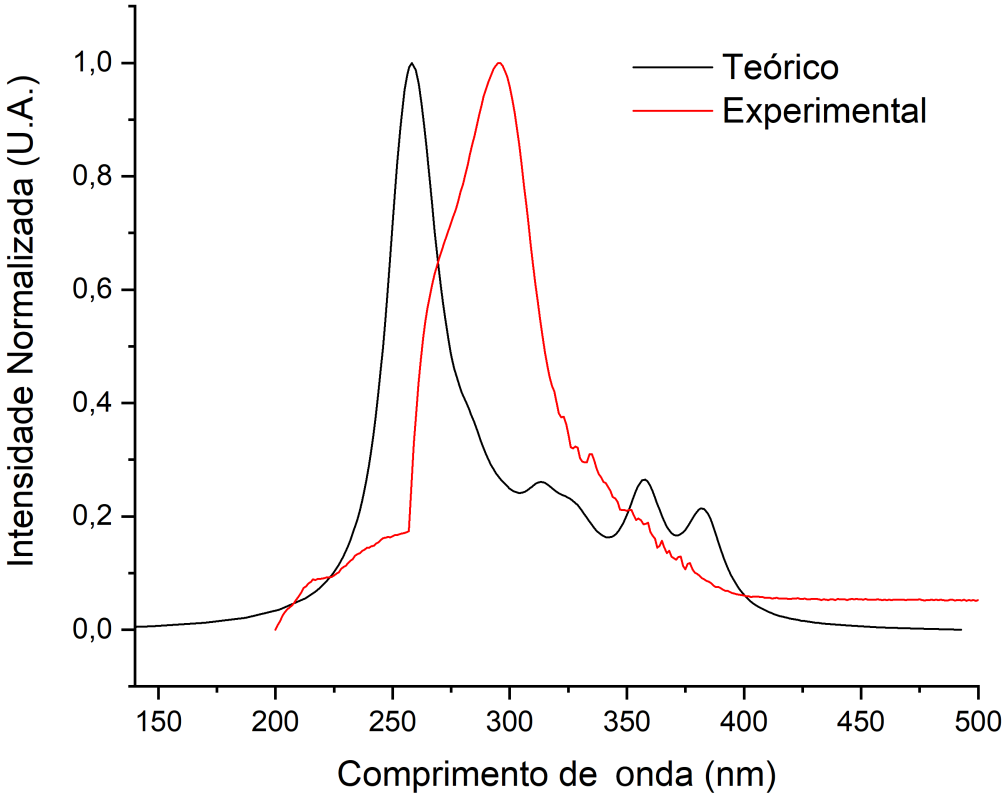

Figura 8 – Comparação do espectro de absorção teórico e experimental do complexo $[GdL_3(H_2O)_2]$.

A Tabela 3 apresenta as principais transições eletrônicas para a formação do estado excitado. A Figura 9 representa os principais orbitais moleculares envolvidos na espectroscopia de absorção do complexo. Na Figura 9 o ligante usnato é referido como fragmento de acordo com a sua posição. Observando-se as diferenças nas densidades eletrônicas dos orbitais do estado fundamental e do estado excitado correspondente, pode-se determinar o caráter da transição. A banda centrada em 259 nm é composta majoritariamente pela transição de H−08→L+05 (H: HOMO; L: LUMO) envolvendo os três fragmentos: a densidade eletrônica do fragmento 3 é transferida para os fragmentos 1 e 2. Somente o fragmento 1 é responsável pela transição de H−01→L+04. Na transição H−04→L+04, a densidade eletrônica é transferida da parte terminal do fragmento 1 para o sítio de coordenação deste mesmo fragmento e para o fragmento 2 envolvendo um caráter de transferência de carga do ligante para o metal (LMCT, sigla em inglês). Em 314 nm, a principal transição envolve a transferência de carga dos três fragmentos para o fragmento 3. Na transição H−07→LUMO, a densidade eletrônica permanece concentrada no fragmento

3. Em 357 nm ocorre a transição H−04→L+01 onde a transferência de carga ocorre da parte terminal do fragmento 1 para seu sítio de coordenação, transferência semelhante a que acorre em 382 nm.

Tabela 3 – Atribuições das transições eletrônicas, força do oscilador (f) e principais contribuições no espectro de absorção do complexo $[GdL_3(H_2O)_2]$.

λ_{max} (nm)	f	principais contribuições
259	0,278	H−08→L+05 (36%), H−09→L+05 (17%)
282	0,031	H−01→L+07 (12,5%), H−10→L+01 (11%), H−01→L+05 (10,5%)
295	0,018	H−04→L+04 (63%), H−04→L+05 (16%)
314	0,050	H−08→LUMO (17%), H−08→L+01 (15%)
325	0,062	H−07→LUMO (77%), H−03→L+03 (10%)
357	0,165	H−04→L+01 (79%)
382	0,082	H−01→L+01 (78%), H−03→LUMO (11%)

H: HOMO; L: LUMO

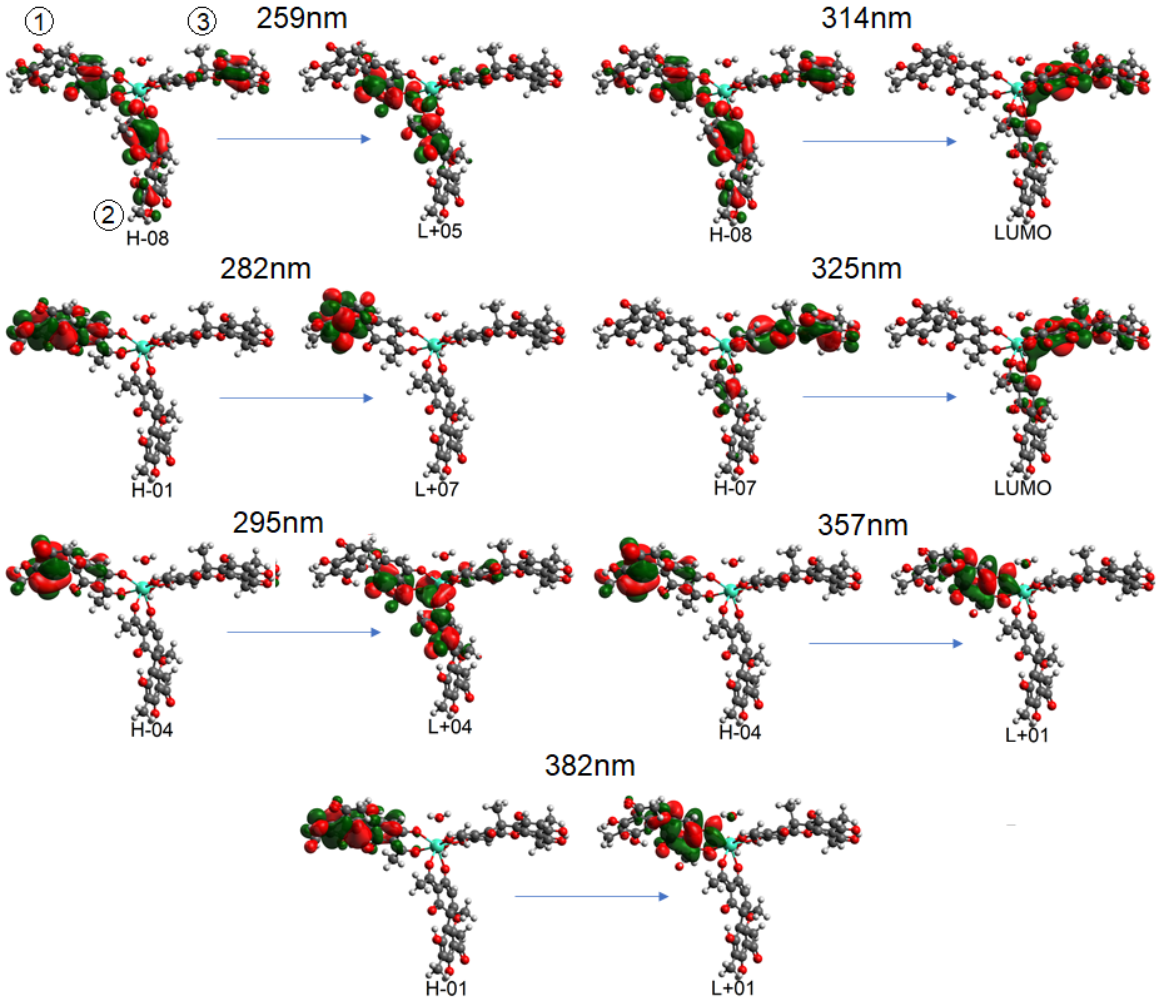

Figura 9 – Principais transições eletrônicas no espectro de absorção para o complexo $[GdL_3(H_2O)_2]$.
Verde indica a fase positiva da função de onda e vermelho indica a fase negativa.

Este trabalho auxiliou na caracterização estrutural e espectroscópica de um complexo de gadolínio com o ânion usnato. Dentro do erro esperado pela técnica utilizada, considera-se uma boa correspondência entre os dados obtidos teoricamente e os dados experimentais, e assim, pode-se levar em conta que os outros complexos de lantanídeo-usnato sintetizados têm a mesma estrutura devido às semelhanças apresentadas por estes elementos. Esta série de compostos está sendo estudada para atividade antitumoral e mais estudos teóricos serão realizados para a avaliação da estrutura eletrônica e possível luminescência onde os resultados já obtidos, principalmente o espectro de absorção, servirão como ponto de partida.

4.2 Complexos policristalinos de cério e lantânio

Nesta seção são apresentados os resultados publicados no periódico *Thermochimica Acta*, intitulado: *Thermal analysis combined with X-ray diffraction/Rietveld method, FT-IR and UV-vis spectroscopy: Structural characterization of the lanthanum and cerium (III) polycrystalline complexes*. O artigo pode ser encontrado nos ANEXOS.

Complexos de lantanídeos com ligantes carboxilados podem ser utilizados na produção de estruturas organometálicas (MOF) que possuem diversas aplicações. Porém, este tipo de composto é de difícil caracterização devido à dificuldade de se formar monocristais [47]. Este trabalho ajudou na caracterização de complexos de cério e lantânio com o ligante 3,5-dimetilbenzoato (DMBz) através de cálculos teóricos.

A Tabela 4 apresenta os comprimentos e ângulos de ligação da esfera de coordenação obtidos após a otimização da geometria dos complexos de lantânio e cério, $[Ln(DMBz)_3(H_2O)]$. Como esperado, devido à semelhança entre os íons, os complexos de La e Ce possuem comprimentos e ângulos de ligação muito próximos. Os comprimentos de ligação Ln−O variam de 2,453 Å à 2,587 Å.

Os complexos sintetizados foram obtidos experimentalmente através da reação de um sal de sódio do DMBz com os lantanídeos. Para o estudo de infravermelho, somente o espectro teórico do lantânio foi usado devido a sua similaridade com o complexo de cério.

As bandas do espectro de infravermelho teórico apresentam boa concordância com o espectro experimental (ver Tabela 5 e Figura 10). Esses resultados sugerem que as estruturas propostas estão muito próximas da estrutura real. Em 1645 e 1363 cm^{-1} são observadas as bandas características de estiramento C=C do anel benzênico. As bandas em 1211 e 1170 cm^{-1} correspondem à deformação no plano da ligação $C-H_3$ e ao estiramento $C-OCH_3$. Em 1542 e em 1399 cm^{-1} estão as bandas de estiramento simétrico e assimétrico COO^-, respectivamente.

Os espectros teóricos e experimentais de absorção são mostrados na Figura 11.

Tabela 4 – Comprimentos e ângulos de ligação selecionados da estrutura teórica dos complexos de La e Ce.

comprimento de ligação (Å)		
	La	Ce
O(1)−Ln(III)	2,497	2,453
O(2)−Ln(III)	2,551	2,515
O(3)−Ln(III)	2,516	2,509
O(4)−Ln(III)	2,587	2,544
O(5)−Ln(III)	2,543	2,464
O(6)−Ln(III)	2,573	2,547
ângulo de ligação (graus)		
	La	Ce
O(1)−Ln(III)−O(2)	51,9	52,7
O(3)−Ln(III)−O(4)	51,3	51,7
O(5)−Ln(III)−O(6)	51,0	52,3

Tabela 5 – Atribuição dos espectros de infravermelho experimental e teórico para os complexos DMBz-sódio e $[La(DMBz)_3(H_2O)]$.

atribuição	experimental (cm^{-1})	teórico (cm^{-1})	experimental (cm^{-1})	teórico (cm^{-1})
	DMBz-sódio		$[La(DMBz)_3(H_2O)]$	
ν C=C (anel)	1653, 1340	1645, 1363	1610, 1331	1646, 1317
δ XH_3 + δ C−H (anel) + ν C-OH_3	1205, 1148	1211, 1170	1202, 1148	1211, 1174
ν_{sim} COO^-	1561	1542	1526	1527
ν_{assim} COO^-	1385	1399	1381	1412

Os espectros experimentais apresentam uma banda larga centrada em 298 nm, já nos espectros teóricos há duas bandas, uma centrada em 300 nm e outra de maior energia em 255 nm. Esta diferença pode vir das condições experimentais, como a presença de solvente, o que não foi incluído nos cálculos aqui reportados. Além disso, pode ocorrer de as bandas nos espectros experimentais estarem sobrepostas.

A Figura 12 representa as principais transições eletrônicas observadas nos espectros de absorção. Pode-se dividir o espectro teórico em três regiões principais de acordo com as localizações das transições. Por volta de 225 nm observa-se as transições H−02→L+03 (98%) e H−01→L+03 (93%). Próximo de 258 nm tem-se as transições H−05→LUMO (86%) e H−04→LUMO (93%). E, em cerca de 302 nm vê-se as transições mais intensas H−02→LUMO (88%) e H−01→LUMO (69%). As porcentagens se referem à contribuição de cada transição para a formação do estado excitado.

Os estudos teóricos permitiram uma melhor compreensão da estrutura eletrônica e dos processos de excitação das moléculas estudadas e podem ser usados para estudar o processo de luminescência do complexo de cério.

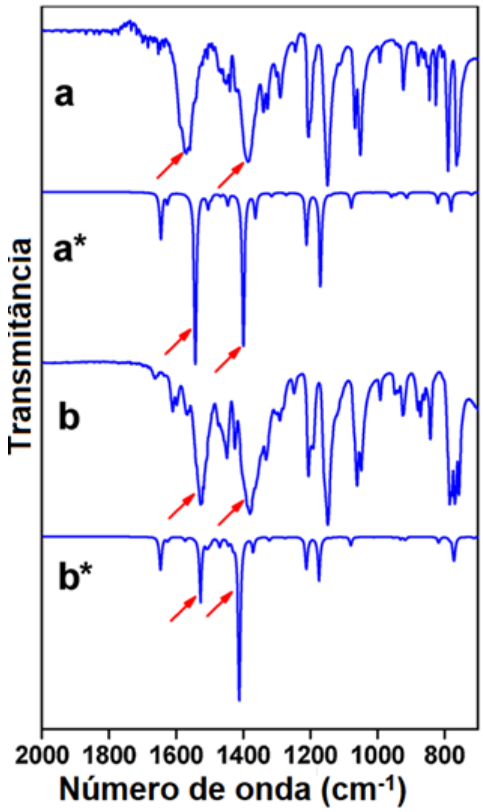

Figura 10 – Espectros de infravermelho experimentais e teóricos do complexo do ligante DMBz e seu sal de sódio.
a espectro experimental DMBz-sódio; **b** espectro experimental complexo com lantânio; **a*** espectro teórico DMBz-sódio; **b*** espectro teórico complexo com lantânio.

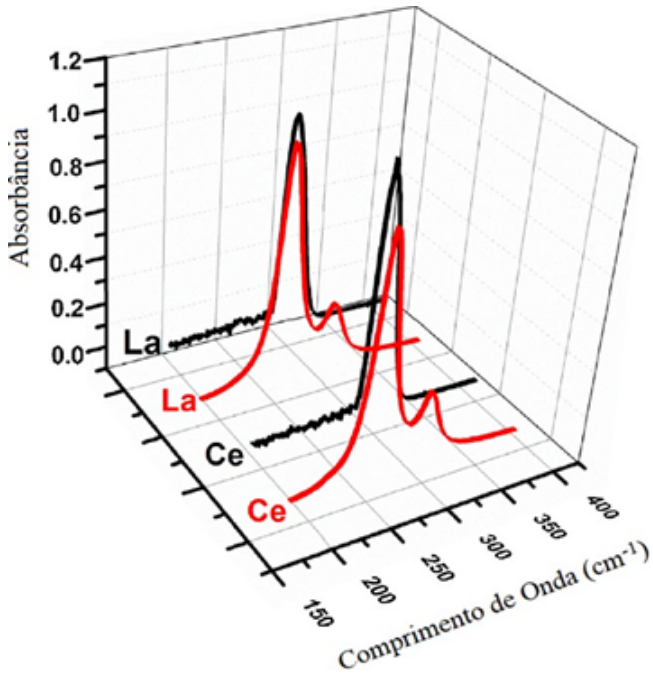

Figura 11 – Espectros de absorbância teórico (vermelho) e experimental (preto) dos complexos de La e Ce com o ligante DMBz.

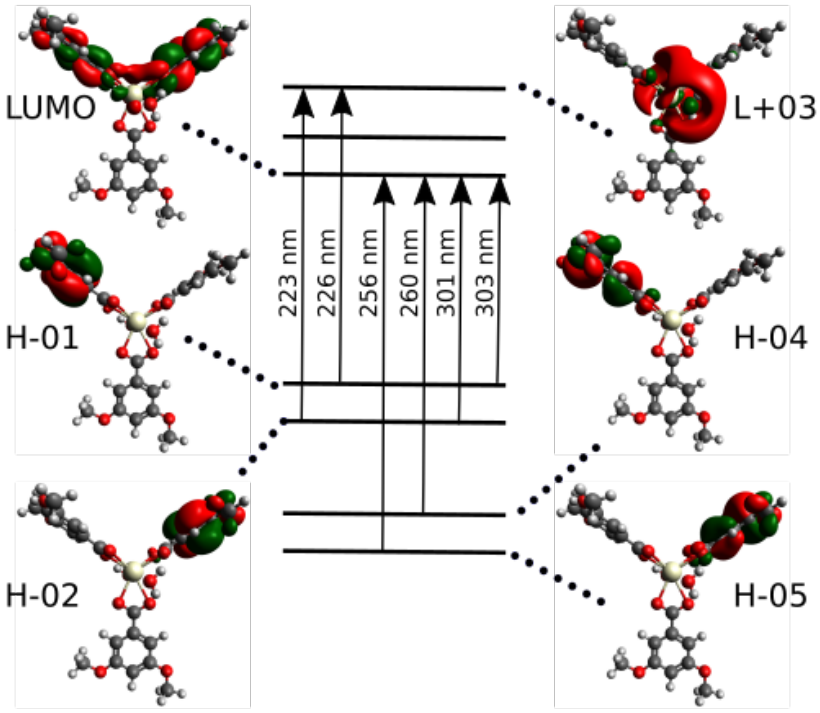

Figura 12 – Principais transições eletrônicas no espectro de absorção do complexo de Ce com o ligante DMBz.

4.3 Complexos de fenantrolina e fenantrolina sililada

Sílica mesoporosa incorporada com complexos luminescentes de lantanídeos apresentam potencial para ser aplicada como sonda biológica, para o diagnóstico e tratamento de câncer, entre outros usos [48]. Comumente a sílica mesoporosa é sintetizada e depois é realizada a incorporação de um complexo em sua superfície. Ao se sintetizar um complexo com o ligante modificado incluindo um grupo sililado a incorporação se torna mais eficiente.

O complexo de európio com os ligantes fenantrolina e 2-tenoiltrifluoroacetona (tta), $[Eu(phen)(tta)_3]$, foi comparado com a sua versão sililada, o complexo de európio com fenantrolina sililada e tta, $[Eu(phensi)(tta)_3]$. A Tabela 6 lista os comprimentos e ângulos de ligação da esfera de coordenação para a estrutura teórica de ambos os complexos.

Os comprimentos e ângulos de ligação na esfera de coordenação apresentam poucas diferenças entre os dois complexos. Estes valores estão compatíveis com experimentos de difração de raios-X apresentados na literatura [49]. Ambos os complexos são octacoordenados e apresentam comprimentos de ligação para Eu−O entre 2,328 Å e 2,402 Å e entre 2,658 Å e 2,687 Å para Eu−N. Os ângulos da ligação O−Eu−O ficam em torno de 71°. Para a ligação N−Eu−N o ângulo calculado para o complexo sililado tem um decréscimo de 0,1°.

A partir da Tabela 7 e da Figura 13 é possível comparar os dados de infravermelho calculados com dados obtidos experimentalmente. O espectro teórico do $[Eu(phen)(tta)_3]$ exibe uma banda com o máximo em 1659 cm^{-1} referente ao estiramento assimétrico da

Tabela 6 – Comprimentos e ângulos de ligação selecionados da estrutura teórica dos complexos [Eu(phen)(tta)$_3$] e [Eu(phensi)(tta)$_3$].

comprimento de ligação (Å)		
	phen	phensi
O(1)−Eu(III)	2,398	2,373
O(2)−Eu(III)	2,359	2,354
O(3)−Eu(III)	2,391	2,330
O(4)−Eu(III)	2,326	2,389
O(5)−Eu(III)	2,373	2,360
O(6)−Eu(III)	2,353	2,402
N(1)−Eu(III)	2,687	2,658
N(2)−Eu(III)	2,661	2,678
ângulo de ligação (graus)		
	phen	phensi
O(1)−Eu(III)−O(2)	71,0	71,3
O(3)−Eu(III)−O(4)	71,8	71,7
O(5)−Eu(III)−O(6)	71,2	70,9
N(1)−Eu(III)−N(2)	61,8	61,7

ligação C=O. Na região de 1580 cm^{-1} é observada a banda de estiramento assimétrico do anel tenoil, em seguida observa-se em 1618 cm^{-1} o estiramento simétrico C=C do anel benzênico presente na fenantrolina e em 1471 cm^{-1} o estiramento simétrico C=C do anel tenoil. A banda em 1201 cm^{-1} corresponde ao estiramento assimétrico C−F. As bandas em 1468 cm^{-1} e em 1311 cm^{-1} correspondem ao estiramento simétrico C=N, em seguida, a banda com máximo em 1352 cm^{-1} refere-se ao estiramento simétrico C=O. Entre 1055 cm^{-1} e 900 cm^{-1} existe uma série de bandas de intensidade muito baixa que são referentes à deformação no plano do anel tenoil, estiramento simétrico C−F e deformação no plano C=CH−C. As bandas em 860 cm^{-1} e 740 cm^{-1} correspondem à deformação fora do plano C−H do anel tenoil. Em 716 cm^{-1} observa-se uma banda de intensidade muito baixa que corresponde à deformação C−H. Por fim, a banda em 479 cm^{-1} corresponde ao estiramento simétrico Eu−O. Em comparação, o espectro do [Eu(phensi)(tta)$_3$] apresenta uma boa correspondência, com bandas deslocadas para a direita e a presença de bandas do grupo trietoxisiloxano: entre 3122 cm^{-1} e 2990 cm^{-1} referente ao estiramento simétrico, em 1501 cm^{-1} e 1315 cm^{-1} para a deformação no plano, em 1550 cm^{-1} para o estiramento assimétrico C−O−Si e entre 494 cm^{-1} e 397 cm^{-1} para a rotação C−O−Si.

Os espectros de absorção estão presentes na Figura 14. A partir da análise populacional de Mulliken foi realizado um estudo de transferência de estrutura eletrônica e de transferência de energia. Os resultados estão apresentados na Tabela 8 e nas Figuras 15 e 16.

A Figura 15 representa as principais transições eletrônicas no espectro de absorção do complexo [Eu(phen)(tta)$_3$]. Em 251 nm observa-se uma banda intensa cuja principal

Tabela 7 – Atribuição dos espectros de infravermelho experimental e teórico para os complexos [Eu(phen)(tta)$_3$] e [Eu(phensi)(tta)$_3$].

atribuição	experimental (cm^{-1}) [48]	teórico (cm^{-1})	experimental (cm^{-1}) [48]	teórico (cm^{-1})
	[Eu(phen)(tta)$_3$]		[Eu(phensi)(tta)$_3$]	
ν_{assim} C=O	1618	1659	–	1613
ν_{assim} C=C−C (anel tenoil)	1528, 1418	1580	–	1589
ν C=C	1618, 1508	1661, 1471	–	1523, 1449
ν_{assim} CF_3	1279	1201	–	1199
ν C=N	1440, 1385	1468, 1311	–	1431, 1336
ν C=O	1355	1352	–	1418
δ C=CH−C (phen)	850	900	–	892
ν CF_3	1030	961	–	1068
δ C−H (anel tenoil)	981	1055	–	1075
δ_f C−H (anel tenoil)	860, 740	828, 713	–	865, 726
δ C−H	716	762	–	778
ν Eu−O	581	479	–	494
ν Si−O−CH_2−CH_3	–	–	3000-2800	3122-2990
δ Si−O−CH_2−CH_3	–	–	1500-1200	1501, 1315
ν_{assim} C−O−Si	–	–	1200-1000	1150
ν C−O−Si	–	–	1000-600	939, 778
ρ C−O−Si	–	–	<500	494-397

contribuição vem da transição H−10→L+07. Como o orbital H−10 é constituído majoritariamente pelo ligante tta e o orbital L+07 é composto majoritariamente pelos orbitais *f* do európio, 89,2% de acordo com análise populacional de Mulliken, esta transição é do tipo LMCT. A banda com o máximo em 277 nm é constituída principalmente pela transição H−07→L+03. O orbital H−07 é composto pelos grupos tiofeno dos três ligantes tta, enquanto o orbital L+03 está localizado predominantemente em um dos ligantes tta, assim, esta transição apresenta caráter de transferência de carga ligante-ligante (LLCT, sigla em inglês) e de transferência de carga intra-ligante (ILCT, sigla em inglês). O orbital H−08 é composto pelos grupos dicarbonil dos ligantes tta e o orbital L+05 é composto principalmente pelos orbitais *f* do európio, com 90,8% de contribuição em sua composição. O orbital H−06 é composto principalmente pelos grupos dicarbonil dos ligantes tta e em menor grau pela fenantrolina, enquanto o LUMO é composto majoritariamente pela fenantrolina. Então, a transição H−06→LUMO, principal componente da banda em 306 nm,

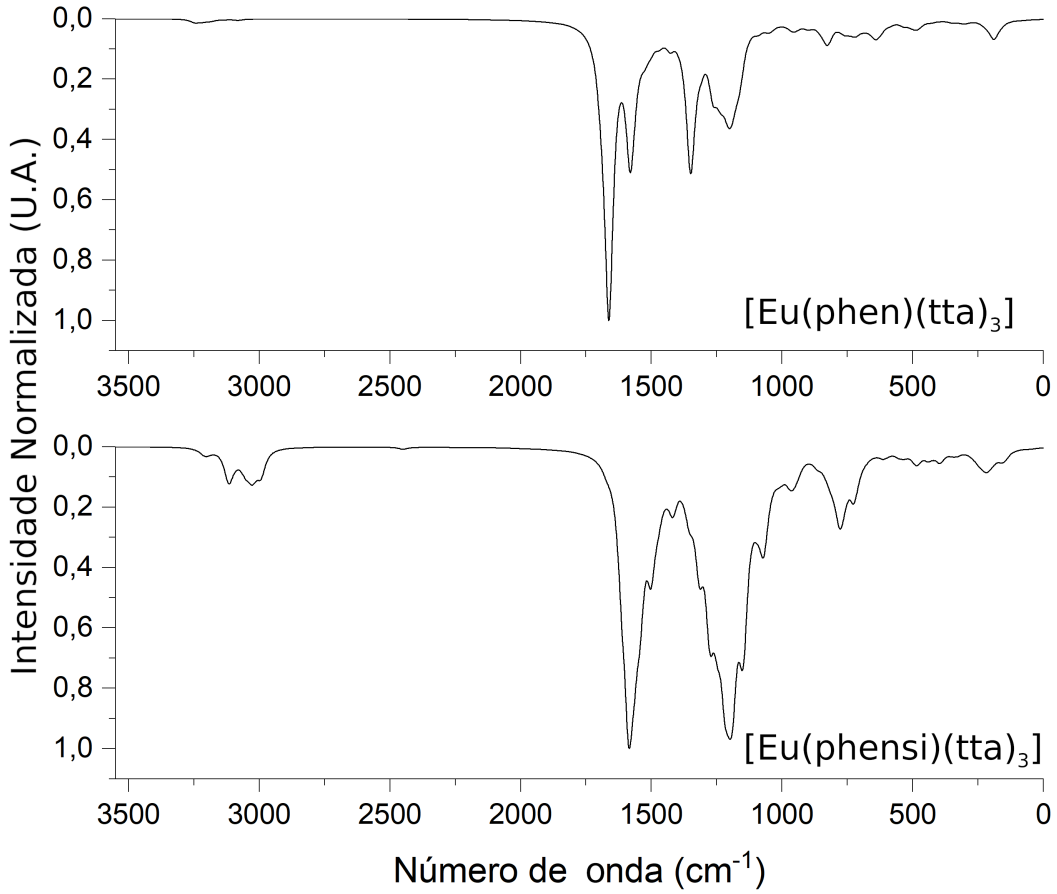

Figura 13 – Comparação dos espectros de infravermelho teóricos dos complexos $[Eu(phen)(tta)_3]$ e $[Eu(phensi)(tta)_3]$.

Tabela 8 – Atribuições das transições eletrônicas, força do oscilador (f) e principais contribuições no espectro de absorção dos complexos $[Eu(phen)(tta)_3]$ e $[Eu(phensi)(tta)_3]$.

$[Eu(phen)(tta)_3]$		
λ_{max} (nm)	f	principais contribuições
251	0,119	H−10→L+07 (55,5%)
277	0,041	H−07→L+03 (17%), H−09→L+01 (16%), H−3→L+4 (14%)
294	0,085	H−08→L+05 (14%), H−06→L+05 (11%)
306	0,254	H−06→LUMO (23%), H−05→LUMO (10%)
312	0,191	H−03→LUMO (19%)
$[Eu(phensi)(tta)_3]$		
λ_{max} (nm)	f	principais contribuições
249	0,080	H−16→L+05 (26%)
255	0,156	H−17→L+02 (11%)
276	0,025	H−10→L+01 (58%), H−11→L+01 (19%)
293	0,070	H−08→L+05 (31%), H−06→L+05 (18%)
306	0,167	H−04→LUMO (57%)
313	0,226	H−02→L+08 (21%), H−02→L+07 (11%), H−02→L+01 (11%)

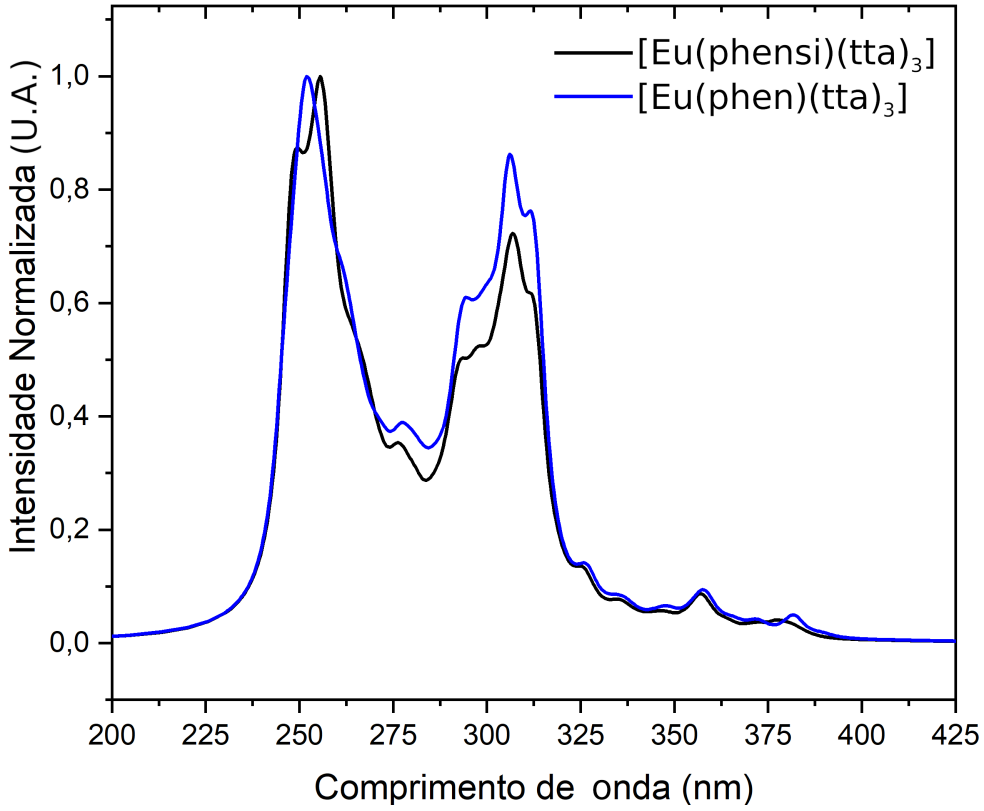

Figura 14 – Espectros de absorção dos complexos [Eu(phen)$(tta)_3$] e [Eu(phensi)$(tta)_3$].

tem caráter ILCT e LLCT. Por fim, na banda em 312 nm ocorre a transferência de carga dos ligantes tta para a fenantrolina, LLCT, na principal transição que a forma.

A Figura 16 representa as principais transições eletrônicas no espectro de absorção do complexo [Eu(phensi)$(tta)_3$]. A banda com o máximo em 249 nm é constituída principalmente pela transição H-16→L+5 (25,92%). O orbital H−16 é composto principalmente pelos grupos dicarnoil dos três ligantes tta e pelo grupo trimetiltrietoxisilano. Já o orbital L+05 é composto majoritariamente pelos orbitais f do európio, 91,5%, desta forma, esta transição é do tipo LMCT. A transição H−17→L+02 é a principal responsável pela banda em 255 nm. O orbital H−17 tem contribuição de todos os ligantes e o orbital L+02 é composto majoritariamente pela fenantrolina, assim, esta transição apresenta caráter de transferência dos tipos LLCT e ILCT. O orbital H−10 é composto principalmente pelo anel tiofeno e o orbital L+01 pela fenantrolina, com a transição H−10→L+01 sendo caracterizada como LLCT e é a principal transição da banda localizada em 276 nm. O orbital H−08 é composto majoritariamente pelo grupo trimetiltrietoxisilano e a transferência ocorre dele para o L+05, sendo a banda em 293 nm composta por esta transição do tipo LMCT. A banda em 306 nm tem a principal contribuição vindo da transição H−04→LUMO. Aqui ocorre a transferência de carga do grupo trimetiltrietoxisilano para a fenantrolina, uma transição do tipo LLCT. Por fim, a banda em 313 nm é caracterizada principalmente por uma transição LMCT. O orbital H−02 é composto pela fenantrolina e pelo grupo tiofeno e o orbital L+08 onde os orbitais f do európio são responsáveis por 88,5% de sua

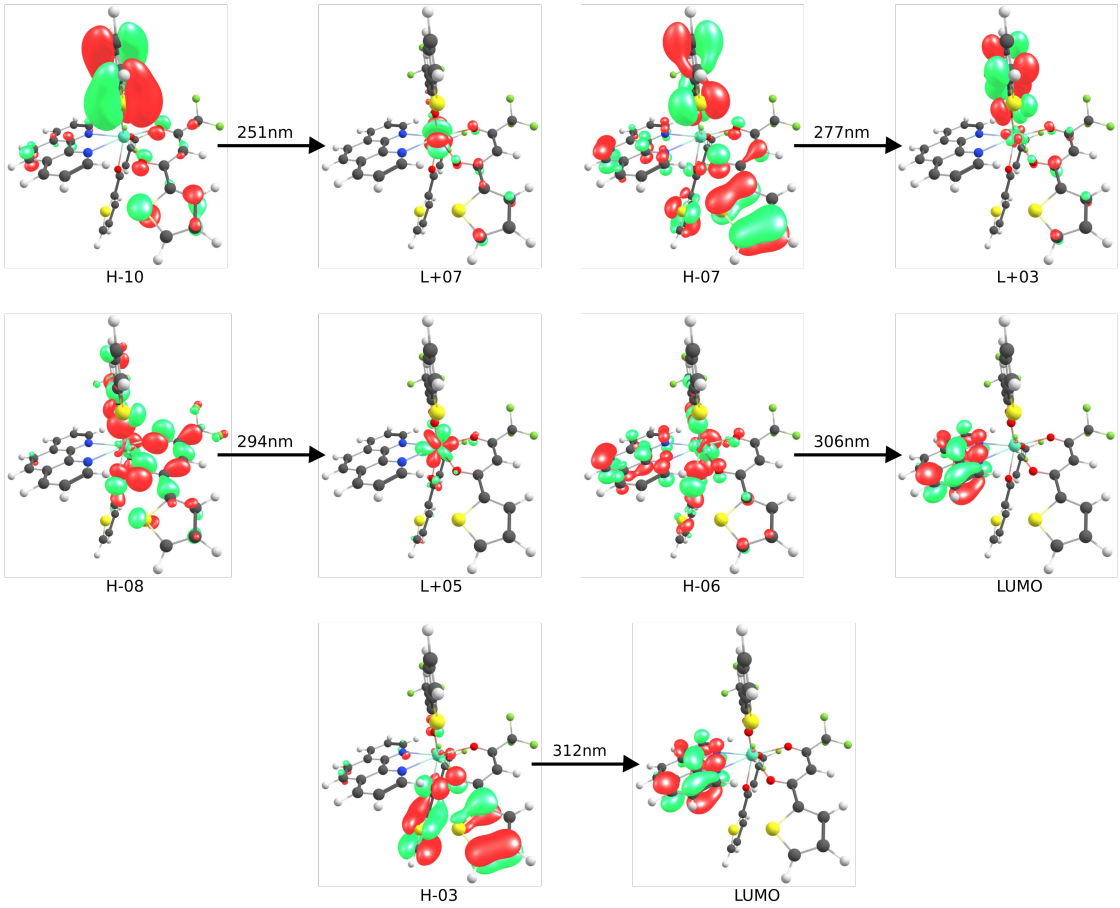

Figura 15 – Principais transições eletrônicas no espectro de absorção do complexo $[Eu(phen)(tta)_3]$.

composição.

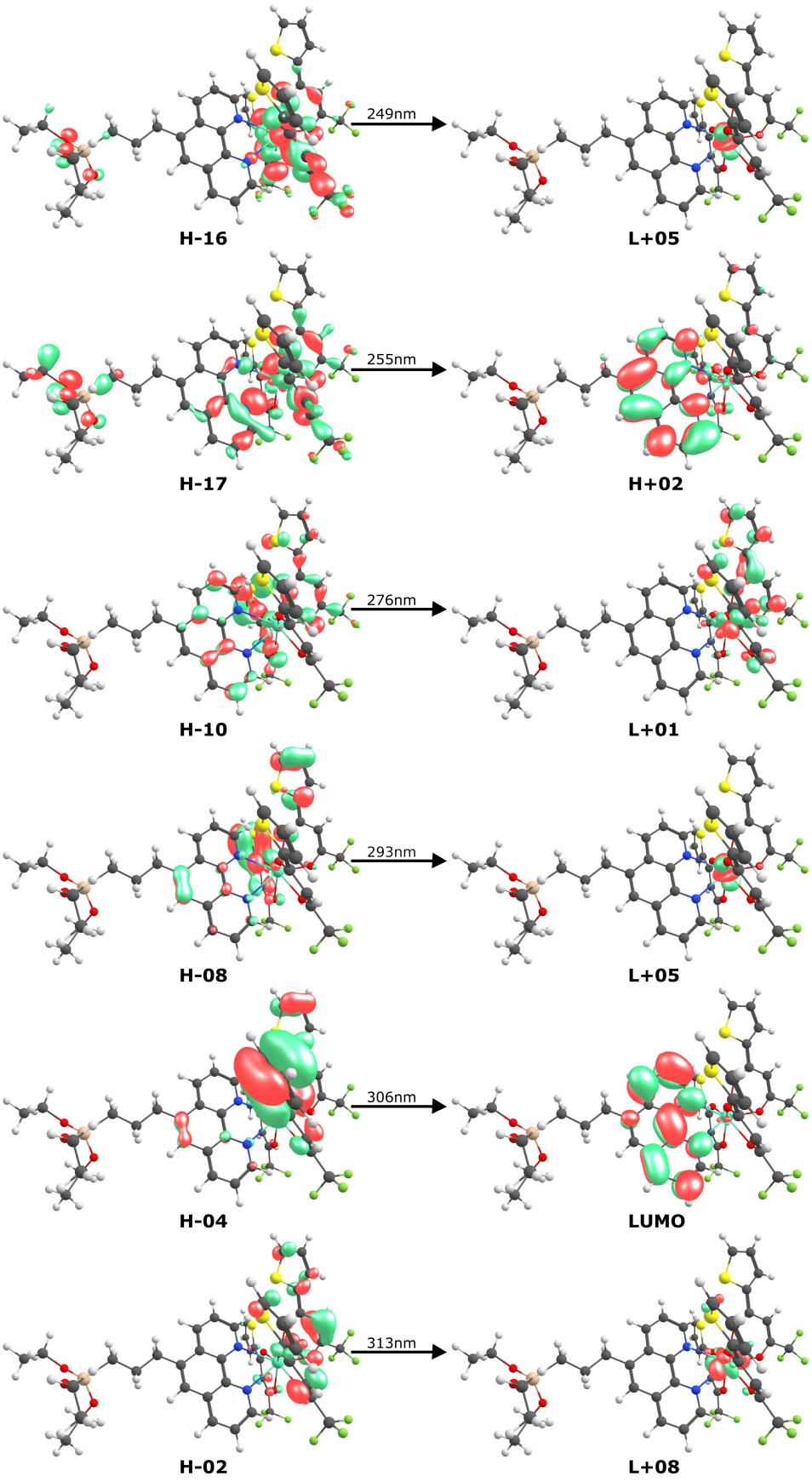

Figura 16 – Principais transições eletrônicas no espectro de absorção do complexo [Eu(phensi)(tta)$_3$].

5 Conclusão

O estudo teórico do complexo $[GdL_3(H_2O)_3]$ indicou a geometria mais provável sendo o anti-prisma quadrado distorcido através do cálculo teórico de sua estrutura. O espectro de absorção na região do ultravioleta-visível apresenta uma banda mais intensa em torno de 250 nm e mais três bandas de menor intensidade em torno de 300 nm, 350 nm e 375 nm. As principais transições eletrônicas foram analisadas e todas elas envolvem mudança de densidade eletrônica do ligante, com a transição em 290 nm apresentando um caráter LMCT. O espectro teórico de infravermelho apresenta boa correspondência com o experimental indicando que a estrutura obtida pelo cálculo de otimização de geometria deve apresentar também uma boa correspondência com o complexo sintetizado.

Os complexos de lantânio e de cério possuem comprimentos e ângulos de ligação muito próximos, o que já era esperado. A semelhança dos espectros teóricos com os experimentais também são um bom indicativo de que a estrutura obtida a partir dos cálculos se aproxima da estrutura real. O espectro teórico de UV-vis apresenta uma banda intensa centrada em torno de 250 nm e uma banda de menor intensidade em 300 nm para ambos os complexos. As transições de $H-01$ e $H-02$ para $L+03$ apresentam caráter LMCT e as restantes envolvem transferências de carga no ligante. Os espectros teóricos de infravermelho dos complexos apresentam boa concordância com os espectros experimentais.

Os complexos $[Eu(phen)(tta)_3]$ e $[Eu(phensi)(tta)_3]$ possuem espectros de absorção na região do UV-vis semelhantes. Porém, a análise da estrutura eletrônica revela que o $[Eu(phensi)(tta)_3]$ possui mais estados excitados, o que interfere nos orbitais moleculares envolvidos nas transições eletrônicas. Os espectros de infravermelho teóricos apresentam diferenças, indicando a presença do grupo sililado para o $[Eu(phensi)(tta)_3]$. Os dados também são comparáveis com os dados experimentos. A análise das transições eletrônicas ajuda a entender a formação dos estados excitados e revelam que estão presentes as transições do tipo LLCT, ILCT e LMCT.

6 Perspectivas

Os resultados teóricos obtidos a partir dos cálculos baseados na teoria DFT e TD-DFT tiveram uma boa concordância em comparação com os estudos experimentais para os complexos aqui apresentados. Assim, os métodos computacionais podem ser pensados para a previsão das propriedades de outros compostos semelhantes. É possível fazer estudos no estado tripleto destes complexos e com isso obter informações sobre possíveis processos de emissão. A partir de todas essas informações, será possível propor mecanismos de luminescência para complexos deste tipo. O complexo de fenantrolina e fenantrolina sililada serão posteriormente estudados com modificações nos grupos ligantes. O grupo tta deverá ser gradualmente substituído por fenantrolina sililada até o complexo ser formado somente por este último ligante, resultando na série: [Eu(phensi)$(tta)_3$], [Eu$(phensi)_2(tta)_2$], [Eu$(phen)_3$(tta)]. Além disso, poderá ser feito o estudo teórico buscando determinar como estas mudanças nos ligantes afetam suas propriedades espectroscópicas e os dados obtidos serão comparados ao complexo já estudado experimentalmente [Eu$(phen)_3$(tta)].

Referências

[1] Moura, J.L., Costa, I.F., Santos, P.R.S., Silva, I.F., Moura, R.T.J., Carneiro Neto, A.N., Faustino, W.M., Brito, H.F., Sabino, J.R., and Teotonio, E.E.S. Enhancing the luminescence of Eu(III) complexes with the ruthenocene organometallic unit as ancillary ligand. *Inorganic Chemistry*, 61(34):13510–13524, 2022.

[2] Meyer, R. and Hauser, A.W. Geometry optimization using Gaussian process regression in internal coordinate systems. *Journal of Chemical Physics*, 152(8):084112, 2020.

[3] Kerkeni, B., García-Bernete, I., Rigopoulou, D., Tew, D.P., Roche, P.F., and Clary, D.C. Probing computational methodologies in predicting mid-infrared spectra for large polycyclic aromatic hydrocarbons. *Monthly Notices of the Royal Astronomical Society*, 513(3):3663–3681, 2022.

[4] Vigneresse, J.L. Revisiting immiscibility through DFT chemical descriptors. *Theoretical Chemistry Accounts*, 139(8):142(15), 2020.

[5] Al-Zaqri, N., Pooventhiran, T., Rao, D.J., Alsalme, A., Warad, I., and Thomas, R. Structure, conformational dynamics, quantum mechanical studies and potential biological activity analysis of multiple sclerosis medicine ozanimod. *Journal of Molecular Structure*, 1227:129685, 2021.

[6] Lewars, E.G. *Computational Chemistry: Introduction to the Theory and Applications of Molecular and Quantum Mechanics*. Springer International Publishing, Suiça, 3rd edition, 2016.

[7] Mardirossian, N. and Head-Gordon, M. Thirty years of density functional theory in computational chemistry: an overview and extensive assessment of 200 density functionals. *Molecular Physics*, 115(19):2315–2372, 2017.

[8] Ye, N., Yang, Z., and Liu, Y. Applications of density functional theory in COVID-19 drug modeling. *Drug Discovery Today*, 27(5):1411–1419, 2022.

[9] Lee, S. and Han, W.S. Cyclometalated Ir(III) complexes towards blue-emissive dopant for organic light-emitting diodes: fundamentals of photophysics and designing strategies. *Inorganic Chemistry Frontiers*, 7:2396–2422, 2020.

[10] Tantillo, D.J. Questions in natural products synthesis research that can (and cannot) be answered using computational chemistry. *Chemical Society Review*, 47(21):7845–7850, 2018.

[11] Nguyen, T.D., Nguyen, C.C., and Tran, V.H. Molecular dynamics study of microscopic structures, phase transitions and dynamic crystallization in Ni nanoparticles. *RSC Advances*, 7(41):25406–25413, 2017.

[12] Chen, X., Hou, T., Persson, K.A., and Zhang, Q. Combining theory and experiment in lithium-sulfur batteries: Current progress and future perspectives. *Materials Today*, 22:142–158, 2019.

[13] Cui, Y., Zhu, P., Liao, X., and Chen, Y. Recent advances of computational chemistry in organic solar cell research. *Journal of Materials Chemistry C*, 8:15920–15939, 2020.

[14] Hohenberg, P. and Kohn, W. Inhomogeneous electron gas. *Physical Review*, 136(3B): B864–B871, 1964.

[15] Kohn, W. and Sham, L.J. Self–consistent equations including exchange and correlation effects. *Physical Review*, 140(4A):A1133–A1138, 1965.

[16] Su, N.Q. and Xu, X. Development of new density functional approximations. *Annual Review of Physical Chemistry*, 68(1):155–182, 2017.

[17] Maitra, N.T. Perspective: Fundamental aspects of time-dependent density functional theory. *Journal of Chemical Physics*, 144(22):220901, 2016.

[18] Maitra, N.T. Double and charge-transfer excitations in time-dependent density functional theory. *Annual Review of Physical Chemistry*, 73(1):117–140, 2022.

[19] Abel, R., Wang, L., Harder, E., Berne, B.J., and Friesner, R. Advancing drug discovery through enhanced free energy calculations. *Accounts of Chemical Research*, 50(7): 1625–1632, 2017.

[20] Nehra, K., Dalal, A., Hooda, A., Singh, D., Kumar, S., Singh Malik, R., and Kumar, P. Influence of coordinating environment on photophysical properties of uv excited sharp red emitting material: Judd Ofelt analysis. *Journal of Photochemistry and Photobiology A: Chemistry*, 430:113999, 2022.

[21] Gregório, T., Leão, J.M., Barbosa, G.A., Ramos, J.L., Om Kumar Giese, S., Briganti, M., Rodrigues, P.C., de Sá, E.L., Viana, E.R., Hughes, D.L., Carlos, L.D., Ferreira, R., Macedo, A.G., Nunes, G.G., and Soares, J.F. Promoting a significant increase in the photoluminescence quantum yield of terbium(III) complexes by ligand modification. *Inorganic Chemistry*, 58(18):12099–12111, 2019.

[22] Josephine Kanimozhi, A., Abdul Sattar, M., Prajith, N., and Logu, N. Luminescent samarium(III) heteroleptic complex of naphthol functionalized imidazo[4,5-f][1,10]phenanthroline and dibenzoylmethane. *Materials Today: Proceedings*, 68: 478–482, 2022.

[23] Rousset, E., Piccardo, M., Gable, R.W., Massi, M., Sorace, L., Soncini, A., and Boskovic, C. Elucidation of LMCT excited states for lanthanoid complexes: A theoretical and solid-state experimental framework. *Inorganic Chemistry*, 61(35): 14004–14018, 2022.

[24] Shi, Y., Naren, G., Zhang, Y., Han, J., and Bohnuud, A. Synthesis, structures, optical properties and dft studies of neodymium complexes containing octanoyl amino carboxylic acids. *Optics & Laser Technology*, 155:108445, 2022.

[25] Fix, T., Nonat, A., Imbert, D., Di Pietro, S., Mazzanti, M., Slaoui, A., and Charbonnière, L.J. Enhancement of silicon solar cells by downshifting with Eu and Tb coordination complexes. *Progress in Photovoltaics: Research and Applications*, 24(9): 1251–1260, 2016.

[26] Sy, M., Nonat, A., Hildebrandt, N., and Charbonnière, L.J. Lanthanide-based luminescence biolabelling. *Chemical Communications*, 52(29):5080–5095, 2016.

[27] Ambiliraj, D.B., Francis, B., and Reddy, M.L.P. Lysosome-targeting luminescent lanthanide complexes: from molecular design to bioimaging. *Dalton Transactions*, 51: 7748–7762, 2022.

[28] Bai, C., He, S., Hu, H.M., Zeng, H., Zou, F., and Wang, J.J. Europium(III) complex-functionalized $SiO_2\alpha mTiO_2$ nanospheres for Al^{3+}-modulated multicolor emission. *Nanomaterials*, 11(11), 2021.

[29] Reddy, M.L.P., Divya, V., and Bejoymohandas, K.S. Luminescent lanthanide molecular materials as potential probes for the recognition of toxic and biologically important cations. *Dyes and Pigments*, 215:111248, 2023.

[30] Zheng, Y., Tan, C., Wang, Q., and Zhang, C.C. 2-(3-pyridyl)imidazole-4,5-dicarboxylic acid based lanthanide luminescent anion sensor. *Solid State Sciences*, 13(9):1687–1691, 2011.

[31] Piccinelli, F., Leonzio, M., Bettinelli, M., Melchior, A., Faura, G., and Tolazzi, M. Luminescent Eu^{3+} complexes in acetonitrile solution: Anion sensing and effect of water on the speciation. *Inorganica Chimica Acta*, 453:751–756, 2016.

[32] Okayasu, Y., Wakabayashi, K., and Yuasa, J. Anion-driven circularly polarized luminescence inversion of unsymmetrical europium(III) complexes for target identifiable sensing. *Inorganic Chemistry*, 61(38):15108–15115, 2022.

[33] Cataldo, A., Chvojka, M., Park, G., Šindelář, V., Gabbaï, F.P., Butler, S.J., and Valkenier, H. Transmembrane transport of fluoride studied by time-resolved emission spectroscopy. *Chemical Communications*, 59:4185–4188, 2023.

[34] Shurygin, A.V., Vovna, V.I., Korochentsev, V.V., Mirochnik, A.G., Kalinovskaya, I.V., and Sergienko, V.I. Electronic structure and optical properties of Ln(III) nitrate adducts with 1,10-phenanthroline. *Spectrochimica Acta Part A: Molecular and Biomolecular Spectroscopy*, 213:176–183, 2019.

[35] Shurygin, A.V., Korochentsev, V.V., Cherednichenko, A.I., Mirochnik, A.G., Kalinovskaya, I.V., and Vovna, V.I. Electronic structure and optical properties of Eu(III) tris-β-diketonate adducts with 1,10-phenanthroline. *Journal of Molecular Structure*, 1155:133–142, 2018.

[36] Daumann, L.J., Tatum, D.S., Snyder, B.E.R., Ni, C., Law, G.l., Solomon, E.I., and Raymond, K.N. New insights into structure and luminescence of Eu^{III} and Sm^{III} complexes of the 3,4,3-LI(1,2-HOPO) ligand. *Journal of the American Chemical Society*, 137(8):2816–2819, 2015.

[37] Neese, F. The ORCA program system. *Wiley Interdisciplinary Reviews: Computational Molecular Science*, 2(1):73–78, 2012.

[38] Frisch, M.J., Trucks, G.W., Schlegel, H.B., Scuseria, G.E., Robb, M.A., Cheeseman, J.R., Scalmani, G., Barone, V., Petersson, G.A., Nakatsuji, H., Li, X., Caricato, M., Marenich, A.V., Bloino, J., Janesko, B.G., Gomperts, R., Mennucci, B., Hratchian, H.P., Ortiz, J.V., Izmaylov, A.F., Sonnenberg, J.L., Williams-Young, D., Ding, F., Lipparini, F., Egidi, F., Goings, J., Peng, B., Petrone, A., Henderson, T., Ranasinghe, D., Zakrzewski, V.G., Gao, J., Rega, N., Zheng, G., Liang, W., Hada, M., Ehara, M., Toyota, K., Fukuda, R., Hasegawa, J., Ishida, M., Nakajima, T., Honda, Y., Kitao, O., Nakai, H., Vreven, T., Throssell, K., Montgomery, J.A., Jr., Peralta, J.E., Ogliaro, F., Bearpark, M.J., Heyd, J.J., Brothers, E.N., Kudin, K.N., Staroverov, V.N., Keith, T.A., Kobayashi, R., Normand, J., Raghavachari, K., Rendell, A.P., Burant, J.C., Iyengar, S.S., Tomasi, J., Cossi, M., Millam, J.M., Klene, M., Adamo, C., Cammi, R., Ochterski, J.W., Martin, R.L., Morokuma, K., Farkas, O., Foresman, J.B., and Fox, D.J. Gaussian 16 Revision B.01, 2016. Gaussian Inc. Wallingford CT.

[39] Hanwell, M.D., Curtis, D.E., Lonie, D.C., Vandermeersch, T., Zurek, E., and Hutchison, G.R. Avogadro: an advanced semantic chemical editor, visualization, and analysis platform. *Journal of Cheminformatics*, 4(1):17, 2012.

[40] Allouche, A.R. Gabedit–A graphical user interface for computational chemistry softwares. *Journal of Computational Chemistry*, 32(1):174 – 182, 2011.

[41] Lee, C., Yang, W., and Parr, R.G. Development of the Colle-Salvetti correlation-energy formula into a functional of the electron density. *Physical Review B*, 37(2): 785–789, 1988.

[42] Becke, A.D. Density-functional thermochemistry. III. The role of exact exchange. *Journal of Chemical Physics*, 98(7):5648–5652, 1993.

[43] Weigend, F. and Ahlrichs, R. Balanced basis sets of split valence, triple zeta valence and quadruple zeta valence quality for H to Rn: Design and assessment of accuracy. *Physical Chemistry Chemical Physics*, 7(18):3297–3305, 2005.

[44] Dolg, M., Stoll, H., and Preuss, H. A combination of quasirelativistic pseudopotential and ligand field calculations for lanthanoid compounds. *Theoretical Chimica Acta*, 85: 441–450, 1993.

[45] Dolg, M., Stoll, H., Savin, A., and Preuss, H. Energy-adjusted pseudopotentials for the rare earth elements. *Theoretical Chimica Acta*, 75:173–194, 1989.

[46] Nunes, D.M., Pessatto, L.R., Brasil, D.M., Oliveira, R.J., Pinto, L.M.C., da Costa Iemma, M.R., Altei, W.F., Martines, M.A.U., and Pereira Duarte, A. New complexes of usnate with lanthanides ions: La(III), Nd(III), Tb(III), Gd(III), synthesis, characterization, and investigation of cytotoxic properties in MCF-7 cells. *Inorganica Chimica Acta*, 506:119546, 2020.

[47] Tenório, K.V., Fortunato, A.B., Moreira, J.M., Roman, D., D'Oliveira, K.A., Cuin, A., Brasil, D.M., Pinto, L.M.C., Colman, T.A.D., and Carvalho, C.T. Thermal analysis combined with X-ray diffraction/Rietveld method, FT-IR and UV-vis spectroscopy: Structural characterization of the lanthanum and cerium (III) polycrystalline complexes. *Thermochimica Acta*, 690:178662, 2020.

[48] Lechevallier, S., Jorge, J., Silveira, R.M., Ratel-Ramond, N., Neumeyer, D., Menu, M.J., Gressier, M., Marçal, A.L., Rocha, A.L., Martines, M.A.U., Magdeleine, E., Dexpert-Ghys, J., and Verelst, M. Luminescence properties of mesoporous silica nanoparticles encapsulating different europium complexes: Application for biolabelling. *Journal of Nanomaterials*, 2013:918369, 2013.

[49] Wong, H.Y., Lo, W.S., Chan, W.T.K., and Law, G.L. Mechanistic investigation of inducing triboluminescence in lanthanide(III) β-diketonate complexes. *Inorganic Chemistry*, 56(9):5135–5140, 2017.

Anexos

Inorganica Chimica Acta 506 (2020) 119546

Contents lists available at ScienceDirect

Inorganica Chimica Acta

journal homepage: www.elsevier.com/locate/ica

Research paper

New complexes of usnate with lanthanides ions: La(III), Nd(III), Tb(III), Gd (III), synthesis, characterization, and investigation of cytotoxic properties in MCF-7 cells

Daniel Mendes Nunes[a,b], Lucas Roberto Pessatto[c,f], Daniel Mungo[a], Rodrigo Juliano Oliveira[c,f], Leandro Moreira de Campos Pinto[a], Monica Rosas da Costa Iemma[d], Wanessa Fernanda Altei[e], Marco Antonio Utrera Martines[a], Adriana Pereira Duarte[a,*]

[a] Institute of Chemistry, Federal University of Mato Grosso do Sul (UFMS), Campo Grande, MS, Brazil
[b] Faculty of Chemistry, State University of Mato Grosso do Sul (UEMS), Dourados, MS, Brazil
[c] Federal University of Mato Grosso do Sul (UFMS), Campo Grande, MS, Brazil
[d] Cell Testing and Regenerative Engineering Laboratory, University of Araraquara, SP, Brazil
[e] Department of Physiological Sciences, Federal University of São Carlos, SP, Brazil
[f] State University of Londrina (UEL), Londrina, PR, Brazil

A B S T R A C T

New lanthanides ions complexes were synthesized from the reactions of aqueous – ethanolic solution of the sodium usnate with an aqueous solution of the lanthanides ions. DFT data, UV–VIS spectroscopy, IR, ^{1}H NMR, ^{13}C NMR, HMBC, and elemental and thermal analyses, are consistent with the following general coordination formula: $[LnL_3(H_2O)_x]$, wherein L = $C_{18}H_{15}O_7^-$, Ln = Gd(III), Tb(III), x = 2 and Ln = La(III), Nd(III), x = 3. The chelates presented higher cytotoxic activity in breast cancer tumor cells (MCF-7) compared to organic and inorganic precursors. The two more potent compounds, complexes of La(III) and Gd(III), were tested in non-tumorigenic breast cells MCF-10A, showing less cytotoxicity, which evidenced their selectivity towards tumor cells.

1. Introduction

The usnic acid (2,6-diacetyl-7,9-dihydroxy-8,9-dimethyl-1,3(2*H*,9b*H*)-dibenzofurandione, is one of the most abundant substances extracted from lichens [1]. This molecule was first isolated in 1844 [2], and present R (+) S (−) isomers usnic acid [3] and keto-enol tautomers, being the most stable enol form [4]. In this work, the R(+) isomer was used, and the enolic tautomer was compatible with the data obtained experimentally (Fig. 1).

Usnic acid has a broad biological activity such as antibacterial, antiprotozoal, antiviral, anti-inflammatory, antipyretic and antitumor. Several works present diverse modifications in the structure of the molecule to potentiate these activities [2,5,6].

The antitumor activity of usnic acid was first reported in 1975 [7] in lung carcinoma in rats, and currently has being described in several types of cancers such as: leukemia (L1210) [8], cervix (HCT116) [9], cervical (HeLa) [9], liver (HepG2) [10], melanoma (B16-F10) [11], stomach (BGC823) [12], and breast (MCF-7) [13–16].

In order to increase water solubility and biological activity, the usnic acid has been converted to potassium [17] or sodium [18] salt, that are stable at a wide range of temperatures (40 °C – 70 °C) and pH (6 – 9) [19].

In the literature there is no record of the investigation of transition metals complexes (block d) and of lanthanides with usnate, however, there are reports of the synthesis of metal ions complexes: Cu(II), Pd(II), Ni(II),Co(II), Mn(II) with usnic acid and nitrogen-containing derivatives, in which we observe the formation of bidentade chelates with 1:2 (metal-ligand) stoichiometry of formulas: $[Cu(UA)_2]$, $[Cu(bpy)(UA)CH_3OH]^+$, $[Cu(bpy)(UA)NO_3]$, $[Pd(UA)_2]$, where UA is the usnic acid [20], $[CuL_2]$, $[NiL_2]$ (L = $C_{18}H_{15}NO_6$) [21], $[CuL_2]$, $[NiL_2]$, $[MnL_2]$, (L = $C_{24}H_{20}NO_7$) [22], and tridentades of formulas: $[CuLRCH_3COCH_2CH_3]$ [23] L = $C_{18}H_{15}N_2O_7$, R = $(CH_2)_6CH_3$, $[PdLRCH_3CH_2OH]$ (L = $C_{18}H_{15}N_2O_7$), R = $(CH_2)_6CH_3$ [23], being that the complexes showed activities: antimutagenic, antibacterial, antifungal [22] and cytotoxic in cervical carcinoma cells (HeLa) [23].

The lanthanides (elements that go from the lanthanum Z = 57 to lutetium Z = 71, are characterized by filling the sub-level 4f, (except the lanthanum) [24] form complexes that are cytotoxic in tumor cells. They activate the tumor suppressor gene P53 [25], increase the concentration of reactive oxygen species [26], and their ions can interact with DNA of tumor cells, leading to cell death [27].

Complexes: of La(III), Ce(III) and Nd(III) with coumarin derivatives

* Corresponding author. Tel.: +55 67 3345 3599.
E-mail address: adriana.duarte@ufms.br (A. Pereira Duarte).

https://doi.org/10.1016/j.ica.2020.119546
Received 12 December 2019; Received in revised form 20 February 2020; Accepted 20 February 2020
Available online 26 February 2020
0020-1693/

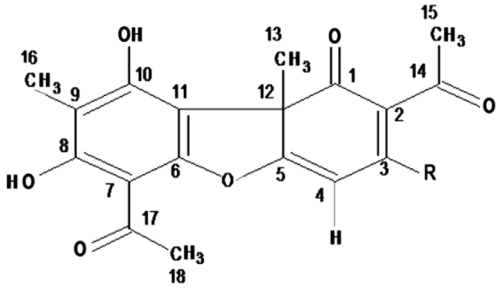

Fig. 1. Structural formula of usnic acid (R = OH) and sodium usnate (R = ONa), used in this work.

[28,29], with 3,5-pyrazolicarboxylic acid [30], and of Gd(III), Dy(III) [31], Sm(III) [31], Eu(III), Tb(III), Dy(III) [32] with 8-quinolinolate, showed cytotoxic activity, respectively in the tumor cells: leukemia (K-562) [28] and (P3HR1) [29], lymphoma (DOHH-2) [30], hepatoma (BEL 7404) [31], breast cancer (MCF-7) [32], being that the complexes of Nd(III) with curcumin and terpyridine have shown selectivity in MCF-7 tumor cells (breast cancer) comparing to normal breast tissue cells (MCF-10A) [33].

Considering the cytotoxic activity of usnic acid in tumor cells and of the lanthanides ions complexes described above, in the present study we describe new synthetic complexes of ions: La(III), Nd(III), Gd(III), Tb (III) with 1:3 lanthanide – ligand stoichiometry, aiming the improvement of cytotoxic profile of these compounds in MCF-7 tumor cells.

2. Experimental

2.1. Equipment, materials and reagents

The usnic acid (98%), sodium carbonate (99.9%), hexahydrate chlorides of lanthanides: Nd(III), Tb(III), Gd(III) and heptahydrate of La (III) (99.9%) as well as the solvents used in this work were purchased from Sigma Aldrich. Elemental analysis were recorded on the CHNS/O 2400 series II Perkin Elmer analyzer. The thermogravimetric curves were made in a TA Instruments Q 50 equipment with a heating rate of 20 °C/min, in an air atmosphere, of 25 °C – 900 °C using platinum crucible and the DSC curves were performed under the same conditions of the thermogravimetric curves, being made using crucible of aluminum in equipment TA Instruments, Q 20 with cooler TA 90. Infrared spectra were collected in Perkin Elmer Frontier FT-IR equipment using KBr inserts of 400 cm^{-1} at 4000 cm^{-1} and spectra in the ultraviolet–visible region were recorded in Perkin Elmer spectrophotometer. The NMR (^{1}H, ^{13}C, and HMBC) spectra were done in a Bruker DPX 300 NMR spectrometer, operating at the frequency of 300 MHz.

2.2. Computational details

DFT calculations were performed employing the hybrid functional B3LYP [34,35] and the def2-SVP [36] basis set for the light atoms (C, O, and H). Since the gadolinium 4f orbitals do not significantly participate in chemical bonding in lanthanides complexes the Stuttgart-Dresden Effective Core Potential (ECP/MBW53) [37] was used; 4f orbitals are much less diffuse (due to their lower radial extension) as compared to the 5d and 6s orbitals. The ECP method treats explicitly only the 8 outermost electrons while the inner electrons are treated as a single core. The basis set for the Gd atom was def2-TZVP [38]. The structure of the complex was optimized in the ground state without symmetry constrains and them further confirmed by a frequency calculation in the ORCA 4.0.1 package [39]. The vertical energies were calculated with time-dependent density functional theory (TD-DFT).

2.3. Synthesis

2.3.1. Synthesis of ligand

The sodium usnate was prepared as described in the literature [18] from the reaction of ethanolic suspension of the usnic acid (3 mmol) with sodium carbonate solution (1.5 mmol) under stirring at 40 °C for 4 h, followed by filtration and obtaining of yellow solid from evaporation of the solvent.

NaL.2.5H_2O color: yellow, yield: 81.8%, elemental analysis: found (calc.) C, 52.75 (52.55); H, 4.86 (4.86). FTIR (KBr, cm^{-1}) 3458 (O–H, water), 3235 (O–H, C_{10}), 2676 (O–H, C_8), 1700 (C_1=O), 1631 (C_{17}=O), 1568 (C_{14}=O), 1075 (C_3–O). NMR ^{1}H (DMSO-d_6) δ (ppm), 5.5 C(4), 14.2 C(8)OH, 13.4 C(10)OH, 1.5 C (13), 2.2 C(15), 1.88 C(16), 2.5 C(18). NMR ^{13}C (DMSO-d_6) δ (ppm), 197.3 C(1), 103.4 C(2), 186.4 C(3), 110.3 C(4), 172.4 C(5), 156.4 C(6), 100.8 C(7), 162.7 C(8), 106.8 C(9), 159.8 C(10), 105.9 C(11), 54.8 C(12), 7.9 C(13), 192.09 C(14), 33.1 C(15), 31.95 C(16), 200.9 C(17), 31.3 C(18).

2.3.2. Synthesis of complexes

Sodium usnate (0.3 mmol) was dissolved in a mixture of water–-ethanol (3:1) and 0.1 mmol of hexahydrate chlorides of lanthanides: Nd (III), Tb(III), Gd(III) and heptahydrate of La(III) were added to this solution under stirring for 8 h at 50 °C, occurring the formation of yellow precipitate which was washed with ice water and dried in a vacuum desiccator.

[$LaL_3(H_2O)_3$]. color: yellow, yield: 78.87%, elemental analysis: found (calc.) C, 53.17 (53); H, 4,29 (4.17); thermal analysis (TGA): found (calc.) La, 11.81 (11.36). FTIR (KBr, cm^{-1}): 3443 (O–H, water), 3179 (O–H,C_{10}), 2702 (O–H, C_8), 1701 (C_1=O), 1631 (C_{17}=O), 1557 (C_{14}=O), 1064 (C_3–O). NMR ^{1}H (DMSO-d_6) δ (ppm), 5.5 C(4), 13.25 C(8)OH, 12.26 C(10)OH, 1.47 C(13), 2.3 C(15), 1.85 C(16), 2.47 C(18). NMR ^{13}C (DMSO-d_6) δ (ppm), 197 C(1), 102.7 C(2), 187.12 C(3), 110.4 C(4), 173.18 C(5), 156.01 C(6), 100.9 C(7), 162.8 C(8), 106.13 C(9), 158.3 C(10), 105.9 C(11), 55.8 C(12), 7.9 C(13), 196.9 C(14) HMBC, 32.5 C(15), 32.4 C(16), 200.8 C(17), 31.2 C(18).

[$NdL_3(H_2O)_3$]. color: yellow, yield: 85.46%, elemental analysis: found (calc.) C, 52.72 (52.77), H, 4.28 (4.15), thermal analysis (TGA): found (calc.) Nd, 12.6 (11.75). FTIR (KBr, cm^{-1}) 3439 (O–H, water), 3209 (O–H,C_{10}), 2702 (O–H, C_8), 1700 (C_1=O), 1631 (C_{17}=O), 1557 (C_{14}=O), 1064 (C_3–O).

[$GdL_3(H_2O)_2$]. color: yellow, yield: 76.4%, elemental analysis: found (calc.) C, 52.96 (52.99), H, 4.02 (4.0), thermal analysis (TGA): found (calc.) Gd, 12.84 (12.86). FTIR (KBr, cm^{-1}) 3448 (O–H, water), 3189 (O–H,C_{10}), 2731 (O–H, C_8), 1700 (C_1=O), 1631 (C_{17}=O), 1557 (C_{14}=O), 1064 (C_3–O).

[$TbL_3(H_2O)_2$]. color: yellow, yield: 84.25%, elemental analysis: found (calc.) C, 52.95 (53.15), H, 4.33 (4.02), thermal analysis (TGA): found. (calc.) Tb, 12.58 (12.62). FTIR (KBr, cm^{-1}) 3441 (O–H, water), 3164 (O–H,C_{10}), 2740 (O–H, C_8), 1700 (C_1=O), 1631 (C_{17}=O), 1557 (C_{14}=O), 1065 (C_3–O).

2.4. Biological assays

2.4.1. Cell lines and culture conditions

In this study the human breast adenocarcinoma cell line MCF-7 and the non-tumorigenic epithelial cell line MCF-10A were used. MCF-7 cells were maintained in Dulbecco's Modified Eagle Medium (DMEM) (Gibco®, Life Technologies, Grand Island, NY, Lot 1875499) supplemented with 10% fetal bovine serum (SBF) (Gibco ®, Lot SPBB2353V), 0.1% antibiotic (penicillin/streptomycin – 10.000u/mL/10.000 µg/mL; LGC ®, Lot 150,317 TB). MCF-10A cells were cultured in DMEM-F12 supplemented with 5% of horse serum, insulin, EGF and hydrocortisone Cells were cultured in 75 cm^2 flasks (Kasvi- Model K11-2250) containing 10 mL of media in a 37 °C incubator and 5% CO_2 (ThermoScientif®; Model 3111).

Table 1
Percentage calculated and determined of carbon, hydrogen, and lanthanide, L = $C_{18}H_{15}O_7$–, AE = elemental analysis, TGA = thermal analysis.

Compound formula	C (calc.)	C (found) AE	C (found) TGA	H (calc.)	H (found) AE	H (found) TGA	M (calc.)	M (found) TGA
NaL.2.5 H_2O	52.55	52.75	52.48	4.86	4.86	4.70	5.6	6.03
$[GdL_3(H_2O)_2]$	52.99	52.96	52.99	4.00	4.02	4.01	12.86	12.84
$[NdL_3(H_2O)_3]$	52.77	52.72	52.39	4.15	4.28	4.06	11.75	12.60
$[LaL_3(H_2O)_3]$	53.00	53.15	52.90	4.17	4.29	4.11	11.36	11.81
$[TbL_3(H_2O)_2]$	53.13	52.95	53.20	4.02	4.33	4.01	12.62	12.58

2.4.2. Cytotoxicity assay

The cytotoxicity assay for 3-(4,5-dimethylthiazol-2-yl)-2,5-diphenyltetrazolium bromide (MTT) was performed according to Navarro et al. [40] and Oliveira et al. [41] with modifications. Cells were seeded in 96-well plates (Kasvi®, Model K12-096) in a density of 2.5×10^4 cells per well and incubated for 24 h for adhesion. After stabilization, cells were treated with the compounds for 24, 48 or 72 h. The compounds NaL·2.5H_2O, $NdCl_3$·6H_2O, $LaCl_3$·7H_2O, $TbCl_3$·6H_2O, $GdCl_3$·6H_2O, $[GdL_3(H_2O)_2]$, $[LaL_3(H_2O)_3]$, $[NdL_3(H_2O)_3]$ and $[TbL_3(H_2O)_2]$ were tested at concentrations of 1.56; 3.12; 6.25; 12.5; 25; 50; 100; 250; 500 and 1000 μg/mL in the MCF-7 cell line. The compounds $[GdL_3(H_2O)_2]$ and $[LaL_3(H_2O)_3]$ were also tested at concentrations of 1.95; 3.9; 7.81; 15.62; 31.25; 62.5; 125; 250; 500 and 1000 μg/mL in the MCF-10A cell line. Cisplatin (Faldicispla, 17A0660) was employed as a positive control at a concentration of 1.72 μg/mL. At the end of incubation times, MTT solution (Invitrogen® CAT No. M6494, Lot MKBW9500V, 0.005 g MTT, 5 mL phosphate-buffered saline, 10 mL HDMEM medium, no SBF) was added to the cells for 4 h in an greenhouse at 37 °C and 5% CO_2. Thereafter, the supernatant was removed and then 100 μL dimethylsulfoxide (DMSO) was added to each well to dilute the formazan salt.

The reading was performed in a spectrophotometer with a 540 nm filter (ELISA Plate Analyzer ROBONIK®). Cell viability (expressed as percentage) was calculated according to the following formula:

$$\text{Cell Viability}\,(\%) = \frac{(\text{Mean Absorbance of the treated group} \times 100)}{(\text{Mean Absorbance of the untreated group})}$$

The experiments were performed in three independent experiments with quadruplicates.

2.4.3. Calculation of the selectivity index (IS)

The selectivity index (IS) between the MCF-10A non-tumor line and the MCF-7 tumor line was calculated according to the following formula:

$$\text{IS} = \frac{(IC_{50}\,\text{of MCF - 10A})}{(IC_{50}\,\text{of MCF - 7})}$$

Samples with IS ≥ 2.0 were considered selective, indicating that the sample is twice more cytotoxic to the neoplastic line when compared to non-tumor cells [42].

2.4.4. Statistical analysis

Cell viability results were expressed as mean ± standard deviation. Statistical analysis were performed by ANOVA with Tukey's post-test and paired *t*-student, where different letters and asterisks indicate statistical differences ($p \leq 0.05$; GraphPad InStat® version 3.10). For the determination of IC_{50} concentration values of the tested compounds, the Graph-Pad Prism software (version 7; Graph-Pad Software Inc., San Diego, CA, USA) was used through non-linear regression curve parameters based on cell viability values.

3. Results and discussion

3.1. Synthesis of ligand and complexes

The synthesis of sodium usnate was done as described in the literature [18] with yielding of 81.88%. The chemical reaction (complexation) between the ligand (usnate) and the lanthanides ions: La(III), Gd(III), Tb(III), Nd(III) was evidenced by the formation of yellow precipitate resulting from the addition of aqueous solution of the lanthanide salt in an aqueous – ethanolic solution of sodium usnate. The complexes presented similar chemical (precipitation reaction) and physical (thermal, solubility) properties since the lanthanides ions present the same oxidation number (III), similar ionic radius and the 4f orbitals are internal with little participation in chemical bonds [43,24].

The complexes were insoluble in polar protic and nonpolar solvents, but soluble in polar aprotic and coordinating solvents (DMSO, DMF).

The thermogravimetric behavior of sodium usnate (Fig. SI-1, Table SI-1) was characterized by the loss of water in the first stage (24.36 °C – 170 °C), break of the metal-ligand bond and decomposition of the ligand (170 °C – 939 °C) with formation of sodium oxide (940 °C).

The thermogravimetric behavior of the complexes (Fig. SI-1, Table SI-1) were similar to that of the sodium usnate, with the following steps: loss of coordination water: Gd(III) (29 °C – 146 °C), Tb(III) (29 °C – 152.24 °C), Nd(III) (24.36 °C – 213.5 °C), La(III) (24.36 °C – 204 °C), break of the coordinated ligand and lanthanide – ligand bond: Gd(III) (146 °C – 651.29 °C), Tb(III) (152.24 °C – 674.38 °C), Nd(III) (213.5 °C – 801.37 °C), La(III) (204 °C – 682 °C), and formation of oxide: Gd_2O_3 (651.29 °C), Tb_4O_7 (674.38 °C), Nd_2O_3 (801.37 °C) and La_2O_3 (682 °C).

The DSC curves showed a broad endothermic peak (25 °C – 300 °C) with high enthalpy values of dehydration compatible with coordinated water molecules in the lanthanide ion [44,45] (Fig. SI-2, Table SI-1).

Based on the correlation of elemental and thermal analysis data (Table 1) we can infer that the complexes present 1:3 lanthanide - ligand stoichiometry with coordinated water molecules.

Comparing the infrared spectra (Fig. SI-3) of the complexes and of

Table 2
Vibration frequency (cm^{-1}) in the infrared region of the ligand and of the synthesized complexes, L = $C_{18}H_{15}O_7^-$ w = water.

Functional group	NaL.2.5 H_2O (cm^{-1})	$[GdL_3(H_2O)_2]$ (cm^{-1})	$[LaL_3(H_2O)_3]$ (cm^{-1})	$[NdL_3(H_2O)_3]$ (cm^{-1})	$[TbL_3(H_2O)_2]$ (cm^{-1})
OH (w)	3458	3448	3443	3439	3441
OH (C_{10})	3235	3189	3179	3209	3164
OH (C_8)	2676	2731	2702	2702	2740
C_3–O	1075	1064	1064	1065	1065
C_1=O	1700	1700	1701	1700	1700
C_{17}=O	1631	1631	1631	1631	1631
C_{14}=O	1568	1557	1557	1557	1557
Ln-O + C-CH_3		424	431	429	422

Table 3
Usnic acid complexes and nitrogen-containing derivatives (d) with transitions metals found in the literature.

Coordination formula	Coordination sites	References
$[Cu(UA)_2]$	C_1═O	20
$[Cu(bpy)(UA)CH_3OH]^+$	C_{14}═O, C_3═O	20
$[Cu(bpy)(UA)NO_3]$	C_1═O, C_{14}═O, C_3═O	20
$[Pd(UA)_2]$	C_1═O, C_{14}═O, C_3═O	20
$[CuL_2]$	C_3–O, N (d)	21
$[NiL_2]$	C_3–O, N (d)	21
$[CuL_2]$	C_3–O, N (d)	22
$[CoL_2]$	C_3–O, N (d)	22
$[MnL_2]$	C_3–O, N (d)	22
$[NiL_2]$	C_3–O, N (d)	22
$[CuLCH_3CH_2OH]$	C_3–O, N (d), O(d)	23
$[PdLCH_3CH_2OH]$	C_3–O, N (d), O(d)	23

the ligand (Table 2) we observed that there was no significant change in the frequency of carbonyls vibration (C_1═O) and (C_{17}═O), indicating that theses carbonyls do not bind to the lanthanide ion; however, there was a reduction of approximately 11 cm^{-1} in the frequencies of carbonyl (C_{14}═O) and C_3–O bond, indicating a reduction in the constant of the force and the increase in the length of the carbon-oxygen bond, compatible with bidentate bond of the lanthanide ion at these sites, what are in agreement with the works found in the literature, Table 3, (considering that the difference between sodium usnate and usnic acid, consists of the removal of an enolic hydrogen atom) that indicate the formation of bidentade [20,21] and tridentade [23] chelates.

The wide and intense OH bands of the complexes in the region between 3430 and 3450 cm^{-1} are in accordance with the presence of coordinated water molecules in the lanthanide ion. The wide and low intensity of the OH bands of the complexes in the region between 2700 and 2740 cm^{-1} are consistent with the presence of intramolecular hydrogen bonding of the OH (C_8) with C_{17}═O, while the bands in the region between 3160 and 3210 cm^{-1} are suitable to the presence of intramolecular hydrogen bonding of OH (C_{10}) with (C_1═O) [46].

The bands in the region between 420 and 431 cm^{-1} are compatible with Ln-O + C-CH_3 combination bands, consistent with lanthanide ion binding to the ligand [47].

Both experimental and calculated spectra are in good agreement (Fig. SI-4), the major difference is in the region 4000–2900 cm^{-1} (Table SI-2) where there is a single broad O–H band in the experimental spectrum while in the calculated spectrum there are six well-resolved bands. The reason is that the calculation was done for a single molecule in the gas phase, therefore intermolecular hydrogen bonds are not considered.

Those bands in the calculated spectrum corresponds to O–H and C–H vibrations, which are overlapped in the experimental spectrum.

The values of ε (transition probability) in M^{-1} cm^{-1} of the ligand (10.10^4) and of the complexes: Gd(III) $6.96.10^4$, Tb(III) $8.55.10^4$, La(III) $9.49.10^4$, Nd(III) $13.1.10^4$ are high, compatible with the high absorption of the organic ligand; however the f-f transitions of lanthanides ions are prohibited by the Laporte rule ($\Delta L = 0$), generating to small values of ε, no were bands detected in the visible region of the complexes, in the ultraviolet and visible spectra (Fig. SI-5) [48,49].

Frontier molecular orbitals of the $[GdL_3(H_2O)_2]$ complex are shown in the additional Supplementary material (Fig. SI-6). In the experimental UV–vis spectrum, there is a broad band with a shoulder on the right, while in the calculated spectrum this shoulder appears as a single band and the rest of the broad band is resolved into six other bands (Fig. SI-7). The calculated spectrum also indicates that the broad band found in the experimental spectrum is an overlap of the six bands. Considering the main excitation (higher values of *f*) of each absorption band the assigned are listed in Table SI-3, all excitation corresponds to a $\pi \rightarrow \pi^*$ transition of usnate, except for H-4 → L + 4, where there is a charge transfer from usnate to Gd^{3+}.

Analysis of the data obtained from the hydrogen nuclear magnetic resonance spectrum of the ligand (Fig. SI-8) and of complex of the Lanthanum(III) (Fig. SI-9) demonstrates the absence of the peak of the enolic hydroxyl of the C_3 (δ = 18 ppm) confirming the formation of sodium usnate, which also agrees with the more acidic character of this hydroxyl (pKa = 4,4) if compared to the phenolic hydroxyls of C_8 (pKa = 10,7) and of C_{10} (pKa = 8,8) [2], and also compatible with the increasing of solubility in polar protic solvents (water and ethanol).

The integration (area) of the peaks in the ^{1}H NMR spectrum is consistent with the presence of 15 hydrogen atoms, with the relative ratio of the peak areas (of carbon methyl hydrogens 13, 15, 16, 18 relative to carbon hydrogen 4) 3:1, consistent with the proposed coordination and structural formulas for the La(III) complex with usnate. Table 4 shows δ values, in ppm, of the ligand and the La(III) complex.

Signals of the peaks found in ^{13}C nuclear magnetic resonance spectra of the sodium usnate (Fig. SI-10) and the complex La(III) – usnate (Fig. SI-11) indicate that the carbon skeleton was preserved after the conversion of the usnic acid into salt and also preserved after the

Table 4
Values of δ in ppm of ^{13}C and ^{1}H NMR, correlation (^2J) and (^3J) of HMBC, of the complex: $[LaL_3(H_2O)_3]$.

Carbon atom	Salt usnate (^{13}C) δ (ppm)	Lanthanum complex (^{13}C) δ (ppm)	Salt usnate (^{1}H) δ (ppm)	Lanthanum complex (^{1}H) δ (ppm)	Lanthanum complex (HMBC) ^2J	Lanthanum complex (HMBC) ^3J
C_1	197.30	197.00				
C_2	103.40	102.70				
C_3	186.40	187.12				
C_4	110.30	110.40	5.5 (1H)	5.5 (1H)		
C_5	172.40	173.18				
C_6	156.40	156.01				
C_7	100.80	100.90				
C_8	162.70	162.80	14.2 (1H)	13.25 (1H)	162.8 (C_8)	106.1 (C_9) 100.8 (C_7)
C_9	106.80	106.13				
C_{10}	159.80	158.30	13.4 (1H)	12.26 (1H)		
C_{11}	105.90	105.90				
C_{12}	54.80	55.80				
C_{13}	7.90	7.90	1.5 (3H)	1.47 (3H)	55.8 (C_{12})	173.2 (C_5) 105.9 (C_{11})
C_{14}	192.09	196.90				
C_{15}	33.10	32.50	2.22 (3H)	2.3 (3H)	196.9 (C_{14})	
C_{16}	31.95	32.40	1.88 (3H)	1.85 (3H)	106.1 (C_9)	162.8 (C_8) 158.3 (C_{10})
C_{17}	200.90	200.80				
C_{18}	31.30	31.20	2.5 (3H)	2.47 (3H)	200.8 (C_{17})	

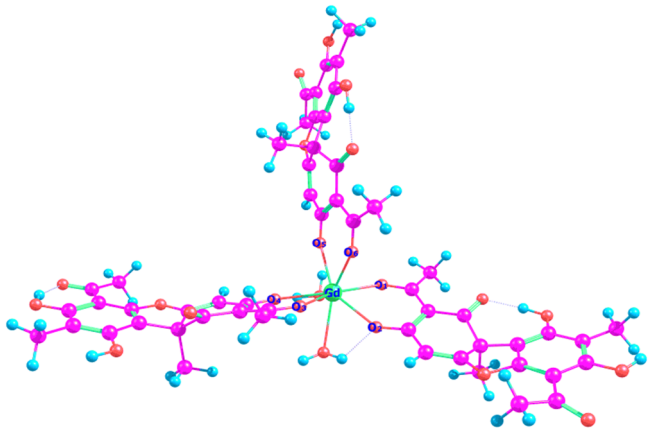

Fig. 2. Coordinating sphere of the $[GdL_3(H_2O)_2]$ complex determined by DFT.

complexation with the lanthanum(III) ion, indicating that there was no precipitation of hydroxides and carbonates but rather the precipitation of the chelate.

Analyzing Table 4, we observe that the values of δ (in ppm), of the carbonyl carbons C_1═O (197.3) and C_{17}═O (200.9) of the sodium usnate practically do not displace with the formation of the complex, suggesting that the metal ion does not bind to these sites.

The HMBC (Heteronuclear Multiple Bond Correlation) spectrum was used to confirm the presence of carbonyl carbon peak signals, usually not very intense due their long relaxation time [50]. From the correlation of ^{13}C nuclear magnetic resonance spectrum with the HMBC spectrum (Fig. SI-12) we observed that the C_{14}═O carbonyl carbon of the sodium usnate was shifted from 192.09 ppm to 196.9 ppm with the formation of the complex, being that bond C_3–O shifts from 186.4 ppm to 187.12 ppm compatible with the La(III) ion binding at these sites with bidentate chelate formation, since the lanthanide ion acts as a Lewis acid removing electron density from the ligand causing unblocking at the atoms of carbons 14 and 3 [51].

The gadolinium ion is coordinated by six oxygens (O_u) from three usnate ligands and two oxygens (O_w) from water molecules (Fig. 2). The average bond distance Gd – O_u is 2,36 Å and Gd – O_w is 2,540 Å. The bond lengths and angles are consistent with a distorted square antiprism (Table 5).

The calculated structure was compared with three ideal eight-coordinated polyhedra: bicapped trigonal prism, trigonal dodecahedron and square antiprism with the aid of the SHAPE 2.1 software. The software compares a given structure with stored ideal polyhedral, resulting in the mean deviation path for each. The results show that the more suitable polyhedra for this complex is the distorted square antiprism. Based on our results and considering that lanthanides ions have similar chemical properties (ionic radius, oxidation number III, solubility, thermal properties) we can propose the following coordination formulas for the synthesized complexes: $[GdL_3(H_2O)_2]$ and $[TbL_3(H_2O)_2]$ with coordination number eight and $[NdL_3(H_2O)_3]$, $[LaL_3(H_2O)_3]$ with coordinating number nine.

Table 5
Lanthanide-ligand bond length and angles of the bidentate bonds of the $[GdL_3(H_2O)_2]$ complex, obtained from DFT calculations.

Bond	Length (Å)	Bond	Angle (°)
O(1) – Gd	2.346	O(1) – Gd – O(2)	68.4
O(2) – Gd	2.380	O(3) – Gd – O(4)	68.1
O(3) – Gd	2.322	O(5) – Gd – O(6)	69.2
O(4) – Gd	2.430		
O(5) – Gd	2.362		
O(6) – Gd	2.311		

3.2. Cytotoxic activity of sodium usnate in MCF-7 breast tumor cells

3.2.1. Effects of organic ligand, sodium usnate, $NaL{\cdot}2.5H_2O$ on MCF-7 cells

Analysis of the organic ligand, $NaL.2.5H_2O$ on MCF-7 cells demonstrated that cytotoxicity may be time-dependent. For the incubation times of 24 and 48 h, significant alterations were observed at concentrations higher than 250 μg/mL, however, after 72 h of incubation, there was a significant decrease in cell viability at the concentrations of 25 μg/mL or higher. Moreover, it was observed that cytotoxicity effect of compounds was concentration-dependent (Fig. 3A). Considering different concentrations of the ligand within a settled time, the cytotoxicity was observed at concentrations higher than 25, 50 and 250 μg/mL, for treatment times of 24, 48 and 72 h, respectively (Fig. SI-13). IC_{50} values determined for the three intervals were 440.1, 235.4 and 20.72, respectively.

3.2.2. Effects of salt $GdCl_3{\cdot}6H_2O$ and complex $[GdL_3(H_2O)_2]$ on MCF-7 cells

$GdCl_3{\cdot}6H_2O$ salt was cytotoxic at the concentrations of 500 and 1000 μg/mL for the 24, 48 and 72 h incubation times (Fig. SI-14A–C). Additionally, the concentration of 50 μg/mL increased the cytotoxicity in 72 h (Fig. SI-14C). On the other hand, the complex $[GdL_3(H_2O)_2]$ was cytotoxic in the concentration range of 100 – 1000 μg/mL in 24 h. In 48 and 72 h experiments, this complex showed cytotoxicity at concentrations of 1.56 μg/mL and higher (Fig. SI-14A–C). All tested concentrations showed a more evident cytotoxicity effect in 48 and 72 h when compared with 24 h treatment. Moreover, in 72 h conditions, cytotoxicity increased at concentrations of 6.25 – 50 μg/mL, compared to 48 h (Fig. 3B).

When comparing the salt $GdCl_3{\cdot}6H_2O$ and the complex $[GdL_3(H_2O)_2]$, statistically significant differences were observed for concentrations equal to and greater than 100 μg/mL in the 24 h analysis. In the 48 h assay, differences were found for the concentrations of 6.25, 25, 50, 100, 250, 500 and 1000 μg/mL and in the 72 h analysis, all concentrations of the complex were more cytotoxic than the salt (Fig. SI-14A–C).

3.2.3. Effects of $LaCl_3{\cdot}7H_2O$ salt and $[LaL_3(H_2O)_3]$ complex on MCF-7 cells

The $LaCl_3{\cdot}7H_2O$ was cytotoxic at concentrations of 500 and 1000 μg/mL in 24 h and 250, 500 and 1000 μg/mL in 48 h and 72 h (Fig. SI-15A–C). Also, a significant increase in cell proliferation was observed at concentrations from 1.56 to 25 μg/mL in 72 h when compared to control (Fig. SI-15C). The $[LaL_3(H_2O)_3]$ complex showed cytotoxicity at concentrations of 100 – 1000 μg/mL in 24 h ($p < 0.05$), whereas in 48 and 72 h, it showed cytotoxicity at concentrations equal to and higher than 3.12 μg/mL (Fig. SI-15B, C). A higher cytotoxic effect was observed in 48 and 72 h for all the tested concentrations except for the concentration of 1.56 μg/mL. The concentration of 3.12 μg/mL caused the same effect in treatments of 48 and 72 h (Fig. 3C). Comparison between $LaCl_3{\cdot}7H_2O$ salt and $[LaL_3(H_2O)_3]$ complex cytotoxic profile revealed that in 24 h both compounds showed statistically significant differences at concentrations equal to and higher than 100 μg/mL (Fig. SI-15A). However, for the other incubation times (48 and 72 h), the complex showed a significant reduction of cell viability in all tested concentrations, when compared with the salt $LaCl_3{\cdot}7H_2O$ (Fig. SI-15A–C).

3.2.4. Effects of $NdCl_3{\cdot}6H_2O$ salt and $[NdL_3(H_2O)_3]$ complex on MCF-7 cells

Statistical analysis of the cellular viability of the different concentrations of the $NdCl_3{\cdot}6H_2O$ salt demonstrated significant cytotoxic activity at concentrations equal to and greater than 100 μg/mL at 24, 48 and 72 h. On the other hand, the complex $[NdL_3(H_2O)_3]$ presented cytotoxicity at concentrations equal to and greater than 12.50 in 24 and 48 h, while in 72 h it decreased cell viability at concentration of

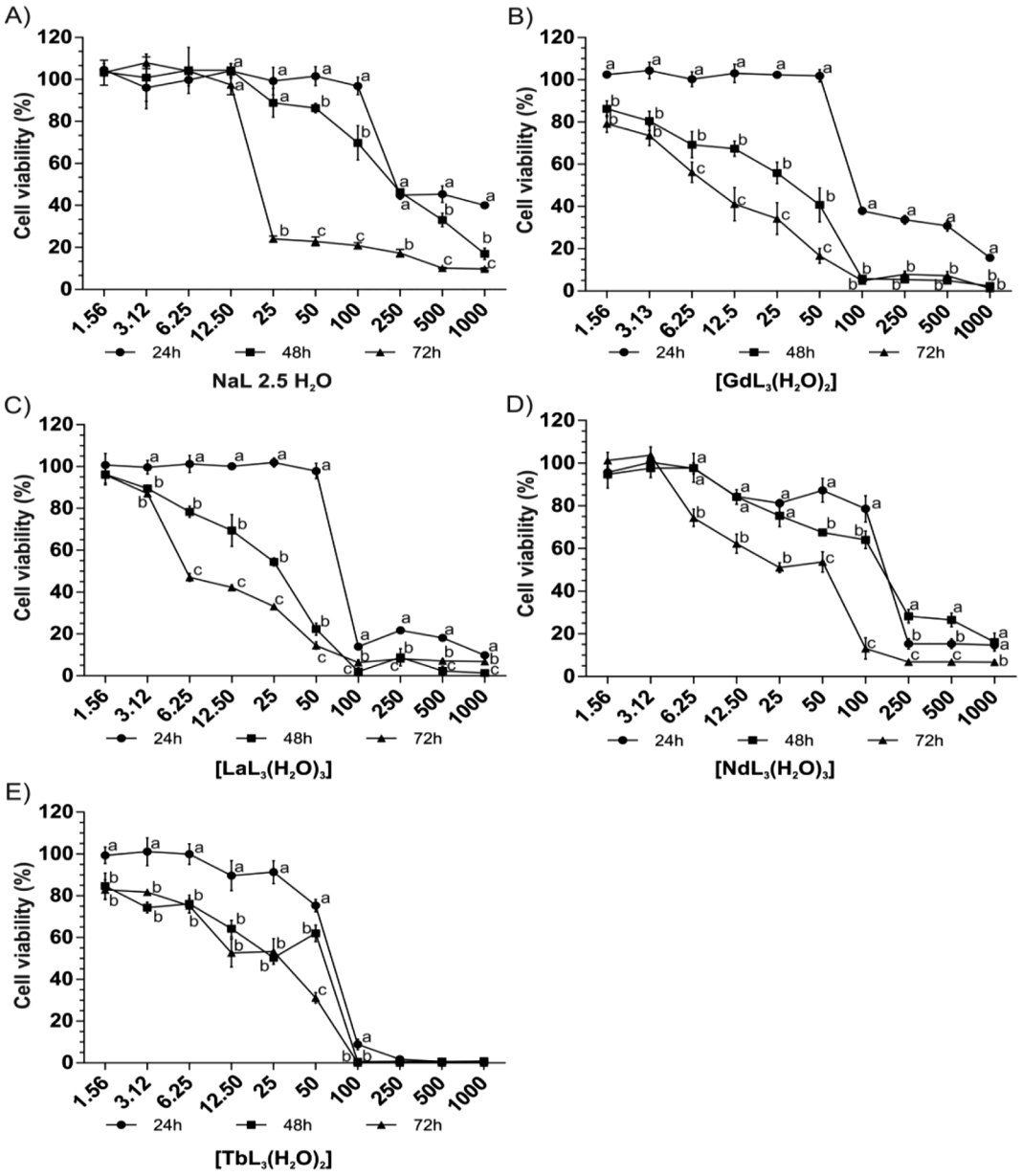

Fig. 3. Cytotoxic activity (Cell viability (%) × μg/mL) of the ligand and of the lanthanides complexes in MCF-7 cells at times of 24 h, 48 h and 72 h.

6.25 μg/mL (Fig. SI-16A–C). Comparing the same concentrations at different treatment times, it was observed that in 72 h the complex is more cytotoxic for all concentrations except for the two lowest ones (1.56 and 3.12 μg/mL). Comparing times of 24 and 48 h, concentrations of 50 μg/mL and higher increased the cytotoxicity over time, except for the concentration of 1000 μg/mL. For 48 and 72 h, all concentrations increased cytotoxicity over time, with exception for the 1.56 and 3.12 μg/mL (Fig. 3D). Comparing the $NdCl_3{\cdot}6H_2O$ salt and the complex $[NdL_3(H_2O)_3]$, a significant difference was observed between 12.50, 250, 500, and 1000 μg/mL in 24 h. At time 48 h, significant differences were observed at concentrations equal to and higher than 12.5 μg/mL, except for the concentration of 1000 μg/mL. For the time of 72 h, significant differences were observed at concentrations equal to and greater than 6.25 μg/mL (Fig. SI-16A–C).

3.2.5. Effects of the salt $TbCl_3{\cdot}6H_2O$ and the complex $[TbL_3(H_2O)_2]$ on MCF-7 cells

The $TbCl_3{\cdot}6H_2O$ salt showed cytotoxicity at concentrations equal to or greater than 100 μg/mL in times 24 h and 72 h (Fig. SI-17A and C). In 48 h, cytotoxicity was observed at concentrations of 25 μg/mL or higher and 6.25 μg/mL (Fig. SI-17B).

Statistical analysis of the cellular viability of the $[TbL_3(H_2O)_2]$ complex showed that there was cytotoxicity ($p < 0.05$) at concentrations of 50 – 1000 μg/mL in 24 h. In 48 and 72 h, the complex was cytotoxic at all concentrations tested ($p < 0.05$) (Fig. SI-17B, C). In the statistical analysis of concentrations between 24 h, 48 h, and 72 h, significant differences ($p < 0.05$) were observed at concentrations of 1.56 – 100 μg/mL. At higher concentrations, the cell viability reached zero in the three times tested, thus without statistical differences between them ($p > 0.05$).

Comparing times the 48 and 72 h, a significant difference was observed only at the concentration of 50 μg/mL (Fig. 3E).

In the comparison between the salt $TbCl_3{\cdot}6H_2O$ and $[TbL_3(H_2O)_2]$, a statistical difference ($p < 0.05$) was observed in concentrations of 25 – 1000 μg/mL in 24 h ($p < 0.05$), 3,12 – 1000 μg/mL in 48 h ($p < 0.05$) and at all concentrations in 72 h (Fig. SI-17A–C). In the comparison between the salt $TbCl_3{\cdot}6H_2O$ and the $[TbL_3(H_2O)_2]$ complex, a statistical difference ($p < 0.05$) was observed in concentrations

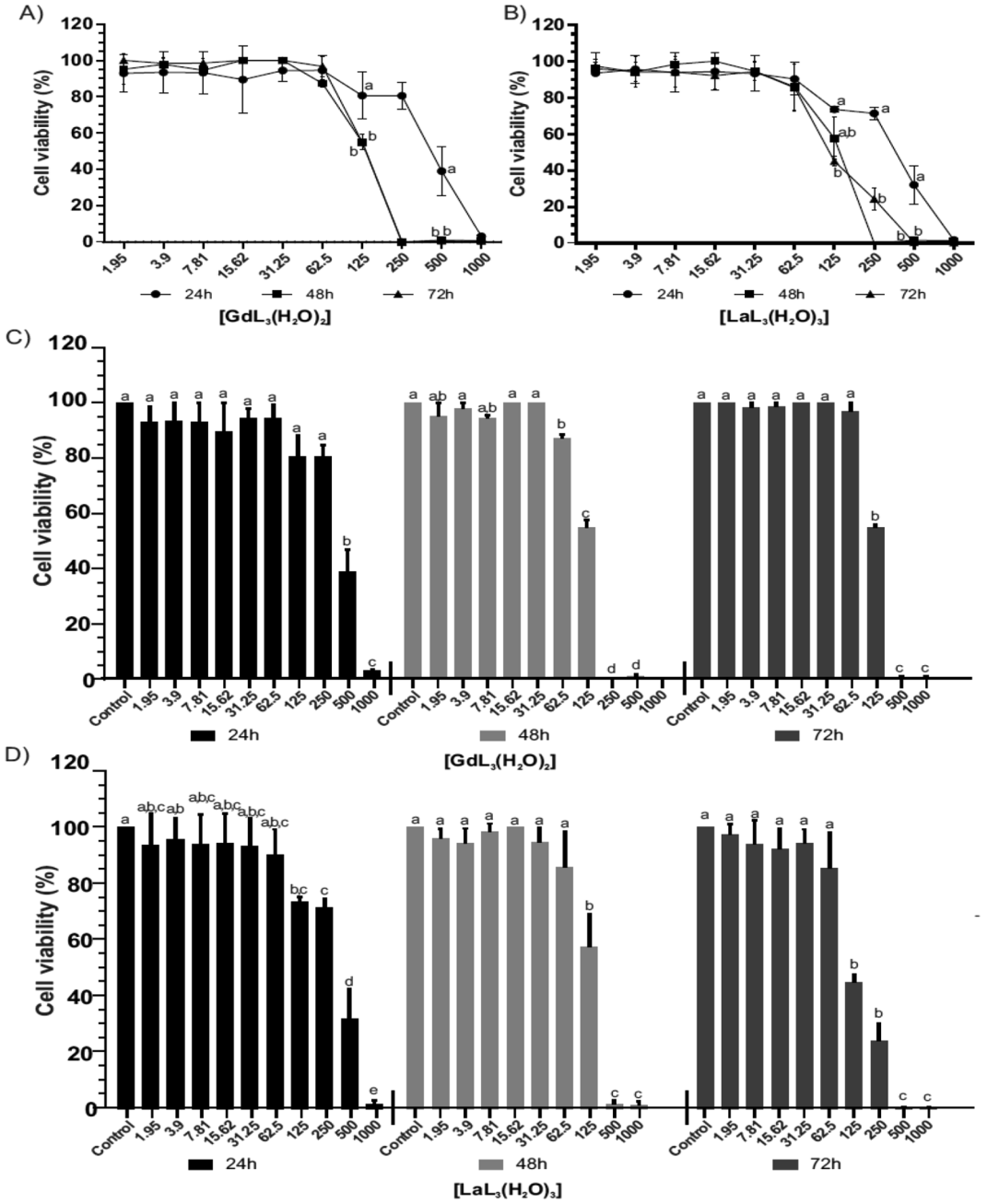

Fig. 4. Cytotoxic activity (Cell viability (%) × μg/mL) of the complexes $[LaL_3(H_2O)_3]$ and $[GdL_3(H_2O)_2]$ in MCF-10 cells.

of 25 – 1000 μg/mL in 24 h ($p < 0.05$), 3.12 – 1000 μg/mL in 48 h ($p < 0.05$) and at all concentrations in 72 h (Fig. SI-17A–C).

3.2.6. Effects of the $[GdL_3(H_2O)_2]$ and $[LaL_3(H_2O)_3]$ in non-tumorigenic cells

Considering the higher activity of $[GdL_3(H_2O)_2]$ and $[LaL_3(H_2O)_3]$ complexes on tumor cells, they were selected for evaluation in healthy breast cells MCF-10A in order to obtain the selectivity index (SI) for these compounds.

The $[GdL_3(H_2O)_2]$ complex was more cytotoxic to MCF-10A cells at concentrations of 125, 250 and 500 μg/mL in 24 h, 48 and 72 h experiments (Fig. 4A). At the concentration of 1000, at the three times tested, cell viability was close or equal to zero. The lower cytotoxic concentrations for this complex were 500 μg/mL in 24 h, 62.5 μg/mL in 48 h and 125 μg/mL in 72 h (Fig. 4C).

A comparison between each concentration in the three treatment times for the $[LaL_3(H_2O)_3]$ complex showed differences for the concentrations of 250 and 500 μg/mL in 24, 48 and 72 h. For the concentration of 125 μg/mL, there was a difference only in the comparison of the 24 and 72 h (Fig. 4B). When the different concentrations were evaluated at the same treatment time, an increase in cytotoxicity was observed from concentration of 125 μg/mL (Fig. 4D).

3.2.7. Potency (IC_{50}) and selectivity index (SI) determination

From the results of the MTT assays, the IC_{50} concentration values were determined for the three incubation times 24, 48 and 72 h, see Table 6.

The selectivity of complexes towards MCF-7 cells was obtained by the determination of the selectivity index. This index was determined from the ratio of IC_{50} values found in the MCF-10A and MCF-7 cells (Table 7).

Both complexes showed selectivity indexes higher than 2, which

Table 6
IC_{50} values for complexes in tumorigenic MCF-7 and non-tumorigenic MCF-10A cell lines.

Incubation time	Complexes				
	IC_{50} – MCF-7 (μg/mL)				
	NaL.2.5 H_2O	$[GdL_3(H_2O)_2]$*	$[LaL_3(H_2O)_3]$*	$[NdL_3(H_2O)_3]$	$[TbL_3(H_2O)_2]$
24 h	400.4	158.8	149.6	148.8	62.7
48 h	235.6	22.1	28.3	127.5	23.4
72 h	20.8	9.04	11.5	29.47	17.1
	IC_{50} – MCF-10A (μg/mL)				
	$[GdL_3(H_2O)_2]$		$[LaL_3(H_2O)_3]$		
24 h	467.9		434.2		
48 h	135.8		144.0		
72 h	130.4		135.5		

*Compounds selected for cytotoxicity test in healthy cells.

Table 7
Selectivity index of the lanthanides complexes.

Incubation time	Selective index values (IC_{50} MCF-10A/IC_{50} MCF-7)	
	$[GdL_3(H_2O)_2]$	$[LaL_3(H_2O)_3]$
24 h	2.94	2.90
48 h	6.14	5.08
72 h	14.42	11.78

configures selectivity of the compounds in the tumor cells. Both, usnic acid and lanthanides ions have antitumoral activity, which aroused interest in our research group to investigate the complexation of this acid (in the form of salt) with lanthanides ions to potentiate cytotoxic activity in tumor cells (MCF-7). So far, there are no studies in literature describing the cytotoxic activity of lanthanides ions complexes: La(III), Tb(III), Nd(III), Gd(III) in MCF-7 tumor cells, being this investigation a pioneering work. Our results agree with the literature descriptions about enhancement cytotoxic activity of chelated compounds in MCF-7 tumor cells when compared with their organic and inorganic precursors, especially in the four highest tested concentrations. Moreover, complexation also decreases the toxicity of lanthanides ions, since the ions will not be free but bound to the ligand [52].

We emphasize that the action of chelates is time-dependent since, in general, cytotoxicity increases according increment on incubation times. The complexes $[GdL_3(H_2O)_2]$ and $[LaL_3(H_2O)_3]$ were chosen for test in healthy cells and SI determination due to their smaller IC_{50} values. The cytotoxicity assays conducted on MCF-10A cells were very promising and highlighted the a decreased ability of these compounds in killing non-tumorigenic cells.

Our results show for the first time complexed usnic acid molecules preferentially killing tumor cells MCF-7 towards the healthy correspondent MCF-10A cells. Despite its antitumor activity, usnic acid is known by its hepatotoxic effects in vitro, that are attenuated on in vivo conditions. Based on our findings in this work we have as a future perspective expand our investigations in order to evaluate whether the complexation of usnic acid changes its hepatotoxic profile. Thus, we believe the results presented so far can contribute significantly for development of new antitumor classes of compounds based on usnate-lanthanides ions complexes.

4. Conclusions

In this work, we synthesized and characterized new complexes of usnate with lanthanides ions. The correlation of the elemental and thermal analyses indicates that the chelates were precipitated with lanthanide-ligand 1:3 stoichiometry, from the reaction of the aqueous-ethanolic solution of the ligand (3:1) with an aqueous solution of the ions: La(III), Gd(III), Tb(III), Nd(III). The correlation of the data of UV–VIS, infrared spectroscopy, nuclear magnetic resonance of hydrogen and carbon 13 indicate the formation of bidentate chelates with the following coordination formulas: $[GdL_3(H_2O)_2]$, $[NdL_3(H_2O)_3]$, $[LaL_3(H_2O)_3]$, $[TbL_3(H_2O)_2]$, where L = $C_{18}H_{15}O_7^-$. The cytotoxic activity in MCF-7 tumor cells (breast cancer) of the complexes was higher than activity of the sodium usnate (except for the neodymium complex) and also higher than the activity of the inorganic precursors (lanthanides salts).

The complexes of La(III) and Gd(III) were more toxic in tumor cells MCF-7 than in normal breast tissue cells (MCF-10A), demonstrating selectivity.

As we modified the structure of the usnic acid, transforming it into salt and chelates, future studies are necessary to evaluate cytotoxic activity in MCF-7 and MCF-10A cells in vivo and the hepatoxicity in vitro and in vivo, in order to consider these complexes as potential candidates to chemotherapy.

Declaration of Competing Interest

The authors declare that they have no known competing financial interests or personal relationships that could have appeared to influence the work reported in this paper.

Acknowledgments

This study was financed in part by the Fundação Universidade Federal de Mato Grosso do Sul – UFMS/MEC-Brasil. This study was financed in part by the Coordenação de Aperfeiçoamento de Pessoal de Nível Superior – Brasil (CAPES) – Finance Code 001. The authors are also grateful to Fundação de Apoio ao Desenvolvimento do Ensino, Ciência e Tecnologia do Estado de Mato Grosso do Sul – Brasil (FUNDECT-MS/PPSUS-MS) – grants 036/2017 and grants 59/300.036/2015 for providing financial support for undertaking this project. The authors wish to thank Photonics Materials Lab – Unesp for the elemental analysis facilities.

Appendix A. Supplementary data

Supplementary data to this article can be found online at https://doi.org/10.1016/j.ica.2020.119546.

References

[1] T.H. Nash III, Lichen Biology, second ed., Cambridge University Press, Cambridge, 2008, pp. 1–112.

[2] K. Ingolfsdottir, Phytochemistry 61 (2002) 729–736.
[3] N.K. Honda, A. Vilegas, Quim. Nova 21 (1998) 110–125.
[4] V. Galasso, Chem. Phys. 374 (2010) 138–145.
[5] O.A. Luzina, N.F. Salakhutdinov, Russ. J. Bioorg. Chem. 42 (2016) 115–132.
[6] O.A. Luzina, N.F. Salakhutdinov, Russ. J. Bioorg. Chem. 42 (2016) 249–268.
[7] S.M. Kupchan, H.L. Kopperman, Experientia 31 (1975) 625–752.
[8] C. Bezivin, S. Tomasi, I. Rouaud, J.G. Delcros, J. Boustie, Planta Med. 70 (2004) 874–877.
[9] M. Backorova, M. Backor, J. Mikes, R. Jendzelovsky, P. Fedorocko, Toxicol. In Vitro 25 (2011) 37–44.
[10] S.C. Sahu, M.A. Sakyi, M.W.O. Donnel Jr, R.L. Sprando, J. Appl. Toxicol. 32 (2012) 739–748.
[11] L.F.G. Brandão, G.B. Alcantara, M.F.C. Matos, D. Bogo, D.S. Freitas, N.M. Oyama, N.K. Honda, Chem. Pharm. Bull. 61 (2013) 176–183.
[12] X. Geng, X. Zhang, B. Zhou, C. Zhang, J. Tu, X. Chen, J. Wang, H. Gao, G. Qin, W. Pan, Med. Sci. Monit. 24 (2018) 556–566.
[13] F. Brisdelli, M. Perilli, D. Sellitri, M. Piovano, J.A. Garbarino, M. Nicoletti, A. Bozzi, G. Amicosante, G. Celenza, Phytother. Res. 27 (2013) 431–437.
[14] S.T. Zuo, L.P. Wang, Y. Zhang, D.N. Zhao, Q.S. Li, D. Shao, X.D. Fang, RSC Adv. 5 (2015) 153–162.
[15] M. Mayer, M.A.O. Neill, K.E. Murray, N.S.S. Magalhães, A.M.A.C. Leão, A.M. Thompson, V.C.L. Appleyard, Anticancer Drugs 16 (2005) 805–809.
[16] H. Draut, T. Rehn, G. Begemann, R. Schobert, Chem. Biodiversity 14 (2017) 1–12.
[17] M.C.B. Martins, M.C.C. Silva, L.R.S. Silva, V.L.M. Lima, E.C. Pereira, E.P.S. Falcão, A.M.A.A. Melo, N.H. Silva, PLoS One 9 (2014) 1–6.
[18] B. Ribar, A. Kapor, Gy. Argay, P. Engel, Z. Djarmati, R.M. Jankov, J. Cryst. Spectrosc. Res. 23 (1993) 107–111.
[19] C. Coiffard, L.J.M. Coiffard, F. Peigne, Y. De Roeck- Holtzhauer, Arch. Pharm. Med. Chem. 331 (1998) 128–132.
[20] M. Takani, T. Yajima, H. Masuda, O. Yamauchi, J. Inorg. Biochem. 91 (2002) 139–150.
[21] M.C. Krugler, S. Tomasi, P. Uriac, L. Toupet, P.V. Weghe, Dalton Trans. (2008) 6524–6526.
[22] S. Kocer, S. Urus, A. Cakir, M. Gulluce, M. Digrak, Y. Alan, A. Asian, M. Tumer, M. Karadayi, C. Kazaz, H. Dal, Dalton Trans. 43 (2014) 6148–6164.
[23] M. Natic, Z. Tesic, K. Andelkovic, N. Brceski, S. Radulovic, S. Manic, D. Sladic, Synth. React. Inorg. Met. Org. Chem. 34 (2004) 101–113.
[24] S. Cotton, Lanthanides and Actinides Chemistry, first ed., John Wiley & Sons, England, 2006, pp. 1–75.
[25] I. Kostova, Curr. Med. Chem. 5 (2005) 591–602.
[26] M.T. Kaczmarek, M. Zabiszak, M. Nowak, R. Jastrzab, Coord. Chem. Rev. 370 (2018) 42–54.
[27] R.D. Teo, J. Termini, H.B. Gray, J. Med. Chem. 59 (2016) 6012–6024.
[28] I. Manolov, I. Kostova, S. Konstantinov, M. Karaivanova, Eur. J. Med. Chem. 34 (1999) 853–858.
[29] I. Kostova, I. Manolov, I. Nicolova, S. Konstantinov, M. Karaivanova, Eur. J. Med. Chem. 36 (2001) 339–347.
[30] I. Kostova, G. Momerov, J. Coord. Chem. 61 (2008) 3776–3792.
[31] Z.F. Chen, X.Y. Song, Y. Peng, X. Hong, Y.C. Liu, H. Liang, Dalton Trans. 40 (2011) 1684–1692.
[32] Y.C. Liu, Z.F. Chen, X.Y. Song, Y. Peng, Q.P. Qin, H. Liang, Eur. J. Med. Chem. 59 (2013) 168–175.
[33] T. Sarkar, S. Banerjee, S. Mukherjee, A. Hussain, Dalton Trans. 45 (2016) 6424–6438.
[34] C. Lee, W. Yang, R.G. Parr, Phys. Rev. B 37 (1988) 785.
[35] A.D. Becke, J. Chem. Phys. 98 (1993) 5648.
[36] F. Weigend, R. Ahlrichs, Phys. Chem. Chem. Phys. 7 (2005) 3297.
[37] M. Dolg, H. Stoll, A. Savin, H. Preuss, Theor. Chim. Acta 75 (1989) 173–194.
[38] M. Dolg, H. Stoll, H. Preuss, Theor. Chim. Acta 85 (1993) 441.
[39] F. Neese, The ORCA program system, WIREs – Comput. Mol. Sci. 2 (2012) 73.
[40] S.D.N. Navarro, L.R. Pessato, A. Meza, E.J.T. Oliveira, S.A. Auharek, L.C. Vilela, D.P. Lima, R.B. Azevedo, C.A.L. Kassuya, O.I.A. Cáceres, R.S. Gomes, A. Beatriz, R.J. Oliveira, M.A.U. Martines, Life Sci. 209 (2018) 300–312.
[41] E.J.T. Oliveira, L.R. Pessatto, R.O.N. Freitas, B.I. Pelizaro, A.P.M. Rabacow, J.M. Vani, A.C.D. Monreal, M.S. Mantovani, R.B. Azevedo, A.C.M.B.A. Silva, R.S. Gomes, R.J. Oliveira, Toxicol. Appl. Pharmacol. 356 (2018) 127–138.
[42] M. Suffness, J.M. Pezzuto, Assays for Cytotoxicity and Antitumor Activity, first ed., (Hostettmann K.) Academic Press, London, 1991, pp. 71–133.
[43] S.P.C. Filho, A.O. Serra, Quim. Nova 37 (2014) 753–760.
[44] L. Zapala, M. Kosinska, E. Woznicka, L. Byczynski, W. Zapala, J. Therm. Anal. Calorim. 124 (2016) 363–374.
[45] Z.L. Wang, C.J. Niu, Z.H. Liu, J.Z. Ni, Thermochim. Acta 282 (1996) 353–358.
[46] S. Forsen, M. Nilsson, C.A. Wachtmeister, Acta Chem. Scand. 16 (1962) 583–590.
[47] K. Nakamoto, Infrared and Raman Spectra of Inorganic and Coordination Compounds, fourth ed., John Wiley & Sons, New York, 1986, p. 260.
[48] J.D. Lee, Inorganic Chemistry Not So Concise; Translation of: H.E. Toma, K. Araki, R.C. Rocha, fifth ed., Edgard Blücher, São Paulo, 1999, p. 443.
[49] V.S. Sastri, J.C. Bunzli, V.R. Rao, G.V.S. Rayudu, J.R. Perumareddi, Modern Aspects of Rare Earths and Their Complexes, first ed., Elsevier, Amsterdam, 2003, pp. 614–634.
[50] D.L. Pavia, G.M. Lampman, G.S. Kriz, J.R. Vyvyan, Introduction to Spectroscopy, fourth ed., Cengage Learning, São Paulo, 2010, pp. 1–202.
[51] A.A. Ansari, J. Coord. Chem. 61 (2008) 3869–3878.
[52] L. Zhang, R. Liu, H. Peng, P. Li, Z. Xu, A.K. Whittaker, Nanoscale 8 (2016) 10491–10510.

Thermochimica Acta 690 (2020) 178662

Contents lists available at ScienceDirect

Thermochimica Acta

journal homepage: www.elsevier.com/locate/tca

Thermal analysis combined with X-ray diffraction/Rietveld method, FT-IR and UV-vis spectroscopy: Structural characterization of the lanthanum and cerium (III) polycrystalline complexes

K.V. Tenorio[a], A.B. Fortunato[a], J.M. Moreira[a], D. Roman[a], K.A. D'Oliveira[b], A. Cuin[b], D.M. Brasil[c], L.M.C. Pinto[c], T.A.D. Colman[a], C.T. Carvalho[a,*]

[a] Federal University of Grande Dourados, UFGD, CP 364, 79.804-970, Dourados, MS, Brazil
[b] Federal University of Juiz de Fora, UFJF, 36036–330, Juiz de Fora, MG, Brazil
[c] Federal University of Mato Grosso do Sul, 79074-460, Campo Grande, MS, Brazil

ARTICLE INFO

Keywords:
Synthesis
Thermal analysis
X-ray diffraction
Polymeric structure
Theoretical calculation

ABSTRACT

In this work, structural, spectroscopical and thermal studies of lanthanum(III) and cerium(III) complexes with the 3,5-dimethoxybenzoate (DMBz) monocarboxylate ligand were performed. The metal-ligand minimum stoichiometry and polymeric arrangement of the complexes were respectively defined by TGA-DSC and X-ray powder diffraction as $[M(DMBz)_3.n]x$, wherein "M" represents the lanthanides, "n" the water molecules in the lanthanum compound and "x" the basic unit of repetition in monoclinic polycrystalline system with space group $P2_1/c$. The products of the thermal decomposition of the material were also monitored by TGA-DSC/FT-IR both in air and N_2 atmospheres in order to suggest the thermal decomposition mechanism. Theoretical calculations based in experimental results were performed to assess the coordination mode and spectroscopic properties of lanthanide complexes involving a monocarboxylate ligand. From theoretical calculations it was possible to generate FT-IR theoretical vibrational spectra and relate the level of correspondence to the experimental data inherent to the metal-ligand coordination mode. From the HOMO/LUMO orbitals obtained by TD-DFT calculations, the main electronic transitions responsible for the absorption and emission bands of the complexes were determined.

- TGA/DSC/FT–IR analysis and refinement by Rietveld method
- Polymeric structure of monoclinic system with space group P21/c
- Elucidation of the type of carboxylate-metal coordination in the complexes
- Computational calculations
- HOMO – LUMO molecular orbital contributions

1. Introduction

Lanthanides complexes obtained with carboxylate ligands in their structure have been extensively studied in the solid state. Characterization of most of these compounds has been done using thermal analysis techniques, mainly thermogravimetric, to establish the dehydration grade, thermal stability, thermal behavior, stoichiometric and purity, as well as infrared spectroscopy (FT-IR) technique to provide information concerning the coordination mode of mono or dicarboxylate ligands to the lanthanides. Among the research groups with an expressive number of scientific papers published on lanthanide carboxylates, it is worth mentioning those of the researchers Ionashiro and Ferenc and their collaborators, represented here by the references [1–3], which can support some of the characterizations used in this study.

In recent years, metal carboxylates, often referred to as coordinating polymers [3], have attracted interest from the scientific community around the world since they can be used to produce a fascinating class of materials, the MOFs (Metal-Organic Frameworks), promising structures for application in catalysis, gas separation, gas storage, ion exchange, luminescence, among others [4,5]. For application of these materials, it is equally interesting to know their structural arrangement, however, in most cases they are difficult to be obtained due to the absence of single crystals [1–4]. One way researchers have found to overcome this is by adding a nitrogenous co-ligand in the synthesis

* Corresponding author.
E-mail address: claudiocarvalho@ufgd.edu.br (C.T. Carvalho).

https://doi.org/10.1016/j.tca.2020.178662
Received 9 March 2020; Received in revised form 12 May 2020; Accepted 23 May 2020
Available online 26 May 2020

process [6,7]. In such syntheses, the researchers Zheng and collaborators and Ling-Yan and collaborators added the 2,2′-bipyridine and 1,10-phenanthroline co-ligands respectively, so that through this methodology they were able to obtain crystalline complexes. These materials were then characterized using x-ray diffraction for single crystal, thermal and spectroscopic techniques, as well as kinetic and luminescence studies.

On the other hand, the synthesis of complexes using only carboxylate ligands to obtain single crystals can also be found in the literature. Those syntheses carried out under hydrothermal conditions are made under high temperature and pressure, however it is not always easy to obtain crystals through this method [8,9].

Finally, an elegant way of elucidating the structure of metallic complexes obtained in powder form is using the Rietveld method for analysis of crystalline parameters.To take full advantage of this method in providing reliable information, though, it is important to make previous use of an appropriate thermogravimetric characterization to determine the stoichiometry of the material, especially carried out under air atmosphere, so that the XRD theoretical and experimental data obtained are convergent. In this sense, Katia and collaborators [10] using the 3,5-dimethoxybenzoate ligand as complexing agent for the praseodymium metal obtained this compound in the form of crystalline powder and resolved its structure combining theoretical calculations, TGA-DSC characterization techniques and powder X-ray diffraction (XRD) analysis and refinement by the Rietveld method.

Another study can be cited to exemplify this application, which is that of Roel and collaborators [5]. They synthesized lanthanide complexes using two different types of dicarboxylate ligand so that one compound was obtained in the form of monocrystal using hydrothermal synthesis, while another four compounds were obtained in the form of crystalline powder. The elucidation of the structures of the compounds, obtained in powder form, was solved using the Rietveld method accompanied by thermal and spectroscopic characterizations, as well as porosity analysis.

Based on the results presented in the literature and given the absence of studies on the elucidation of the crystalline structure of the 3,5 lanthanum(III) and cerium(III) dimethoxybenzoates in the literature, we were motivated to synthesize and characterize them using thermal and spectroscopic techniques as a basis for elucidation of the structure of these materials using X-ray powder diffraction and refinement by the Rietveld method. From the result obtained, other important theoretical-experimental correlations were evaluated using experimental and theoretical FT-IR data and Time-Dependent Density Functional Theory (TD-DFT) calculations in order to obtain insights related to the optical properties of the materials, not found in the literature, for future applications.

2. Experimental

2.1. Synthesis of the complexes

The DMBz, 3,5-dimethoxybenzoic acid $(CH_3O)_2C_6H_3CO_2H$ 97 % purity, was purchased from Sigma-Aldrich Brazil. For the synthesis, a solution of 0.100 mol L^{-1} of sodium salt [NaDMBz] was prepared at the pH of 8.0 from the DMBz acid using a 0.100 mol L^{-1}NaOH solution, whereas the metal salts (chloride or nitrate) solutions were prepared from lanthanum oxide with concentrated hydrochloric acid and from cerium nitrate by direct dissolution, both at the pH adjusted between 5 and 6. The pH measurements were assisted by a pH-meter with glass electrode [10]. Approximately 500 milligrams of each complex [M $(DMBz)_3$] in solid state, wherein M = lanthanum or cerium, were obtained by mixing both solutions at 27 °C so that the slight excess of the ligand aqueous solution was used until complete precipitation of the rare earth ion. The precipitate obtained was washed with distilled water for elimination of chloride or nitrate and sodium ions and filtered through Whatman® quantitative filter paper (Grade 42). After washing, the precipitate was dried in an oven at 60 °C for 10 h and then kept stored in a desiccator until the moment of the analyses.

2.2. Instrumental analysis

FT-IR/ATR spectra of the [NaDMBz] salt and complexes were performed using a Nicolet iS10 FT-IR spectrophotometer using ATR accessory with Ge window.

The TGA-DSC curves were obtained using a thermal analytical system, model STA 449 F3 Jupiter® and the experimental data were obtained by Proteus® Software. For the analysis of the samples, masses near to 10 mg and alumina crucibles under purge gas flow (air or N_2) of 50 ml min^{-1} with heating rate optimized to 10 °C min^{-1} were used.

The percentages of carbon, hydrogen, oxygen and metal were determined by the mass losses data in TGA curves, since the decomposition of the complexes occurs with total thermal decomposition of the organic content and further production of the respective metal oxides of known stoichiometry, La_2O_3 and CeO_2.

The gaseous fragments of the thermal decomposition of the complexes were monitored using a Mettler® TGA-DSC system coupled to a Nicolet® FT-IR spectrophotometer equipped with gas cell and DTGS KBr detector. The gas cell was kept at 250 °C and the 120 cm transfer line at 225 °C. The mass of the samples for the TGA-DSC curves recording were about 10 mg with heating rate of 10 °C min^{-1} in alumina crucibles. The online FT-IR spectra were recorded at 4 cm^{-1}resolution.

The sample image (DSC video) was obtained by the Mettler-Toledo DSC 1 Stare System equipment with a SC30 digital camera which incorporates a 3.3 Megapixel CMOS sensor, Navitar 1-6232D mechanical optical subassembly with 6.5X zoom. The sample mass used was approximately 2 mg heated at the ratio of 10 °C min^{-1}.

2.3. Crystal structure

The $[La(DMBz)_3{\cdot}2H_2O]$ complex, before being analyzed by powder X-ray diffraction, was dehydrated at 200 °C in a muffle furnace, temperature selected according to TGA-DSC previous data. Then, the [La $(DMBz)_3$] and $[Ce(DMBz)_3]$ samples were carefully grounded in an agate mortar and measured by powder diffraction methods, depositing them on a glass sample-holder plate. The diffraction data were collected by overnight scans in the 2θ range of $5-105^{\circ}$ with step of 0.02°, using a Bruker AXS D8 Da Vinci Advanced diffraction equipped with Ni-filtered CuK_{α} radiation (λ = 1.5418 Å) and Lynxeye linear position-sensitive detector (2.94°).The optical parameters were primary-beam Soller slits (2.94°), fixed divergence slit (0.3°) and receiving slit 8.0 mm. The unit cell parameters were checked using about 20 low-angle peaks, followed by indexing through the single-value decomposition approach by Coelho [11,12]. The space group $P2_{1/c}$ was chosen for both complexes and after checking the systematic absences and the cell parameters, they were then refined using diffraction data up to the range of 55° (2θ) using Pawley method [13]. In both cases, no higher symmetry transformations were suggested by Spek [14]. The structure solution process of each complex was performed by the simulated annealing technique [15], also implemented in TOPAS. The 3,5-dimethoxybenzate ion rigid body model based on single-crystal data [16] was defined by the Z-matrix formalism, Fig. 1, as well as in previous works [17,18].

The optical and specimen parameters and angles of torsion, translation and rotation of the lanthanide ions and ligands were adjusted by the Chebyshev polynomial function and refined by the Rietveld method [19]. The crystal structure models found were treated by SA routine in conjunction with new assays. The final Rietveld refinement plots of both complexes are described as supplementary material, Fig. S1a and S1b.

Absorption spectra in the ultraviolet/visible region were recorded using a Digital UV/Visible scanning spectrophotometer, Model IL-592S-BI – KASUAKI, in wavenumber range of 190–1000 nm and spectral band width of 2 nm.

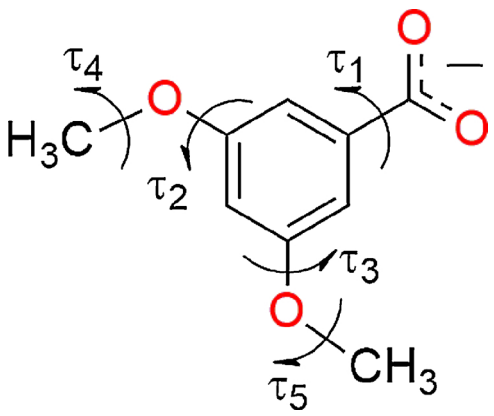

Fig. 1. Sketch of the 3,5-dimethoxybenzate ion. The 5 torsion angles required in the simulated annealing and refinement routines were defined as τ_1 to τ_5.

For the fluorescence studies, a Varian Cary Eclipse spectrofluorimeter was used applying an excitation scan in the range of 210 nm–600 nm at intervals of 10 nm. A xenon lamp with two monochromators was used as excitation source, one of which was intended to select the excitation wavelength and the other to select the wavelength emitted by the sample, with fluorescence detection by a photomultiplier tube. Solutions containing 5 mg of each compound in *N,N*-dimethylformamide (DMF) 99 % purity (J.T. Baker) were analyzed at the temperature of 25 °C.

For the FT-IR theoretical calculation, the quantum chemical approach employed to determine the molecular structure was Becke's three parameter hybrid exchange functional combined with Lee-Yang-Par correlation functional (B3LYP) [20,21]. The molecular calculations in this study were made using the Gaussian 09 routine [22] and the theoretical infrared spectrum was calculated using a harmonic field [23,24] based on C1 symmetry (electronic state 1A). The geometry optimization was computed using the Berny's optimization algorithm and the calculations of vibrational frequencies were also implemented to determine whether the optimized geometry constitutes minimum or saddle points. The principal assignments and descriptions of the infrared active fundamental mode were provided by Gauss View 5.0.2 W graphic routines [25].

Absorption theoretical calculations were performed within TD-DFT using the def2-SVP [26] basis set for the light atoms (C, O, and H), and the def2-TZVP [26] for the lanthanides with the Stutttgart-Dresden ECP (MBW28) for lanthanum [27] and (MBW47) for cerium [27,28] implemented in the ORCA 4.0.1 package (Neese F 2012). Molecular orbital diagrams were reproduced using Avogadro (version 1.2.0) [29,30].

3. Results and discussion

3.1. Thermal study

The TGA-DSC/DTG thermal analyses data, Fig. 2, under air and inert (N_2) atmospheres are shown in the summary form in Table 1 and Table S1 in supplementary material, so that it is possible to make a more accurate analysis of the material studied as follows. For the lanthanum complex under air atmosphere, a mass loss starting at 64 °C (TGA/DTG) is observed, which is associated with a small endothermic peak in the DSC at 91 °C. This event can be attributed to dehydration that occurs in a single step and through a slow process. After this mass loss step, the complex in the anhydrous form is thermally stable over a wide temperature range.

Therefore, from this point onwards the description of the thermal events for both complexes can be summarized in anhydrous form. Thus, by examining the TGA-DSC/DTG curves in the air atmosphere it can be stated that the complexes in their anhydrous form are thermally stable up to around 326 °C (La) and 315 °C (Ce). Above those temperatures, the thermal decomposition of the ligand occurs basically in two stages of mass loss. In these processes, a fact to be highlighted is that the thermal decomposition of the cerium complex occurs in a temperature range lower (315–381 °C) than that for the lanthanum complex (326–401 °C). Based on these experimental data, it can be suggested that the result shown is intrinsically linked to the change of the oxidation state of cerium metal from 3+ to 4+ during the thermal decomposition. This exothermic process probably occurs simultaneously with the decomposition of the organic matter (intense peak at 371 °C), so that it helps raising the temperature inside the sample and concomitantly contributes to the thermal decomposition of the organic matter occurring at a lower temperature and through a fast process when compared to other lanthanide ions complexed with the same ligand. These data can be observed in other studies [2,31,32].

The last two steps of mass loss (TGA/DTG) for lanthanum complex, which comprise a slow mass loss between 401 and 639 °C, is related to thermal decomposition of the carbonized material without peak associated with the DSC and DTG curves, while the mass loss between 639 and 700 °C, associated with an endothermic peak at 673 °C, is related to carbonate decomposition from the dioxycarbonates ($La_2O_2CO_3 \rightarrow La_2O_3 + CO_2$) mixture. In this reaction, as CO_2 is stable under oxidizing atmosphere, it is concluded, based on thermodynamic laws, that the absorbed energy (bond breaks) is greater than the energy released (product formation), that is, with delta H > 0 for this system. This thermal event at 673 °C can be better observed by the 5x magnified image on the y-axis for the DSC curve inserted in Fig. 2. In addition, dioxycarbonates formation, especially for the lanthanum metal coordinated to carboxylate ligands, is common to occur, so that a qualitative test of the residue, obtained at this temperature with diluted HCl solution was used to indicate the presence of carbonate [2,31]. For cerium complex, the last step between 381 and 560 °C (TGA) occurs associated with an exotherm (similar to an extended exothermic peak) in DSC curve between 465 and 550 °C. Furthermore, similarly to the slow stage of mass loss for lanthanum compound, the DTG curve also does not peak in this region, because gradual changes are produced without an inflection point. Lastly, considering the end of the steps for each of the complexes, the residues formed were the La_2O_3 and CeO_2 oxides, which at high temperatures and in an oxidizing atmosphere (air) are obtained free of carbonaceous material. Therefore, from the experimental results obtained using an oxidizing atmosphere in relation to the percentages of water loss, ligand and oxide formation per step (Table 1), when compared to the theoretical results (Table S1), it was possible to establish the empirical formula of these compounds as follows: $[La(DMBz)_3{\cdot}2H_2O]$ and $[Ce(DMBz)_3]$.

TGA-DSC/DTG analysis (Fig. 2) in N_2 inert atmosphere for the complexes shows a different profile of the curves when compared to that presented in air atmosphere. This difference is due to the interaction of oxygen with the released volatiles, resulting in degradation and/or combustion of the organic matter, while in nitrogen atmosphere there is only energy transference (heat) to the substance with higher production of volatile compounds at high temperatures. On the other hand, the thermal events related to the hydration water will always have similar profiles under both atmospheres. This observation ratifies the explanation of the interaction between the atmosphere and the volatile products, since the loss of hydration water only requires energy absorption. In relation to the thermal events of the second step, the differences in the decomposition profile of the organic matter (ligand) are significant under air and N_2. Under air atmosphere, it is possible to observe intense exothermic peaks, while in N_2 atmosphere; endothermic peaks of low intensity are noticed.

Another interesting result observed only in N_2 inert atmosphere is the sharp endothermic peak at 356 °C (La) in the DSC curve, Fig. 2, with no corresponding mass losses in the TGA/DTG curves. This type of event, identified as a physical one, is due to the phase transition of the

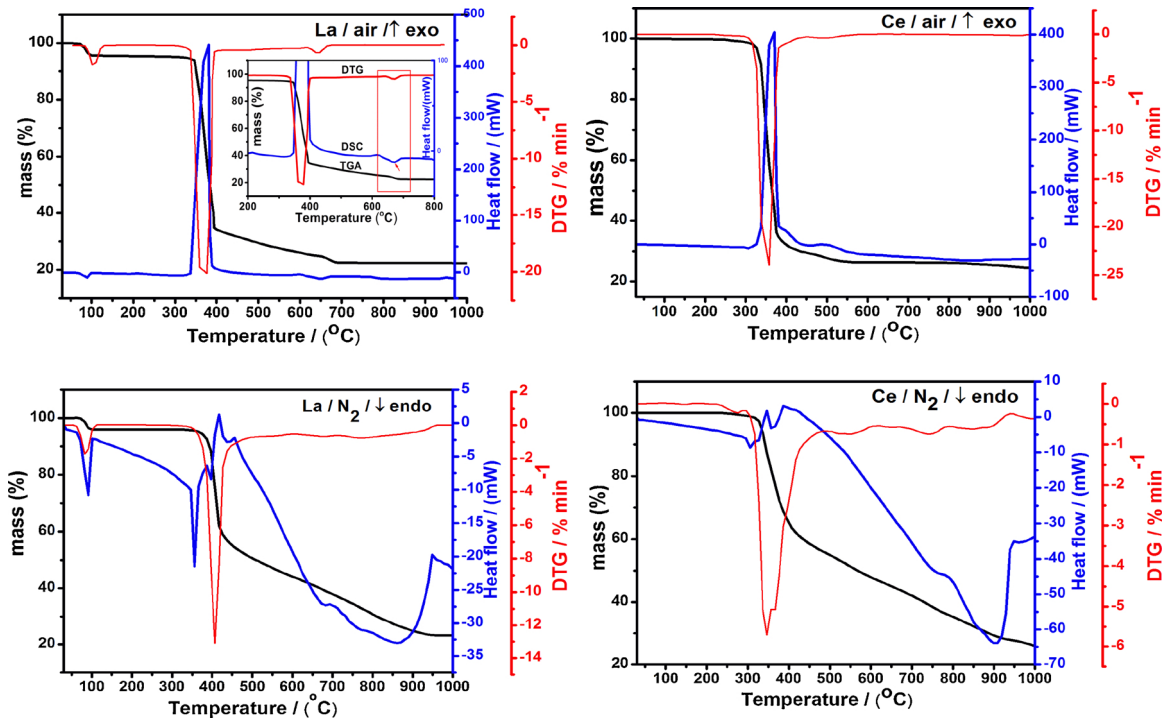

Fig. 2. TGA-DSC/DTG curves in air (for stoichiometry) and N_2 (pyrolysis) atmospheres using a heating ratio of 10 °C min^{-1} and initial mass near 10.0 mg for lanthanum and cerium complexes study. Peaks up (exo) and peaks down (endo).

lanthanum complex in its anhydrous form, as elucidated by DSC analysis coupled to a microscope shown in the video (supplementary material). In addition, the endothermic peaks at 396 and 436 °C (DSC) are probably related to the thermal decomposition/pyrolysis of the organic matter, which occurs within a single rapid step according to DTG peak, between 350 and 439 °C. Thus, examining the relationship between the thermal events observed in the DTG and DSC curves, it can be suggested that the rapid decomposition in this region seems to be favored by the physical event. The last mass loss step, above 439 °C without DTG peak, is related to the thermal decomposition of the pyrolyzed material (carbonaceous material), which is signaled by simultaneous endothermic events in the DSC curve between 670 and 943 °C.

Considering the first thermal decomposition step of the cerium complex, between 262–416 °C (TGA), unlike lanthanum complex, it is possible to observe three endothermic peaks in this region (DSC), being the first two at 306 and 326 °C overlapped, which coincide with a small mass loss in the TGA curve, as well as with the beginning of the opening of two large overlapping DTG peaks, Fig. 2. Thus, it is possible that the beginning of the thermal decomposition is associated with decarboxylation in parallel to the mass losses of the methoxy groups of the ligand, while the adjacent step with DSC peak at 356 °C and overlapping DTG peak (364 °C) can be possibly attributed to the thermal decomposition/pyrolysis of the organic matter, remaining aromatic residue. The last step, between 416 and 1000 °C (TGA) and without a defined

Table 1
TGA-DSC/DTG thermoanalytical data of the lanthanum and cerium complexes performed in air and N_2 atmospheres, where the mass losses and metal oxides formed in air were used for stoichiometric calculus.

Steps of mass loss	Events	$[La(DMBz)_3{\cdot}2H_2O]$ air	$[La(DMBz)_3{\cdot}2H_2O]$ N_2	$[Ce(DMBz)_3]$ air	$[Ce(DMBz)_3]$ N_2
1st	**θ ºC**	64 – 100	72 – 102	299 – 381	262 – 416
	***mg (%)**	0.45 mg (4.50 %)	0.41 mg (4.10 %)	6.61 mg (66.10 %)	3.8 mg (38.00 %)
	Tp (ºC)	91↓	91↓	371↑	306↓, 326↓,356↓
2nd	**θ ºC**	326 – 401	350 – 439	381 – 560	416 – 1000
	***mg (%)**	6.12 mg (61.30 %)	4.159 mg (41.59 %)	0.82 mg (8.20 %)	3.61 mg (36.10 %)
	Tp (ºC)	392↑	356↓↓, 396↓, 436↓	465 – 550 exotherm	909↓
3rd	**θ ºC**	401 – 639	439 – 943	–	–
	***mg (%)**	0.855 mg (8.55 %)	3.101 mg (31.01 %)	–	–
	Tp (ºC)	–	–	–	–
4th	**θ ºC**	639 – 700	–	–	–
	***mg (%)**	0.315 mg (3.15 %)	–	–	–
	Tp (ºC)	673↓	–	–	–
Residue	***mg (%)**	La_2O_3 2.25 mg (22.50 %)	La_2O_3 2.33 mg (23.30 %)	CeO_2 2.57 mg (25.70 %)	CeO_2 + R 2.59 mg (25.90 %)

Temperature range (θ), *mass loss observed in TGA curves in milligrams (mg) and percentage (%), peak temperature (Tp) observed in DSC curves, exothermic event↑, endothermic event↓, phase transition↓↓. DMBz = 3,5-dimethoxybenzoate and R = carbonaceous residue.

peak in the DTG, but with a wide and intense peak at 909 °C is due to partial decomposition of the pyrolyzed material.

In summary, from the TGA-DSC/DTG data in both atmospheres it was possible to observe physical and chemical events such as: thermal behavior, stoichiometric ratio of the complexes, phase transition, thermal stability, decomposition steps and stable residue formation temperature. For the identification of the decomposition products released in each step, a TGA-DSC/FT-IR system was used. Specifically for this analysis type, the nitrogen atmosphere is more efficient than the air atmosphere, since in air the fragmentation of the organic matter leads to an excessive production of carbon monoxide (CO) and carbon dioxide (CO_2), so that these excess can overlap the bands of organic fragments.

3.1.1. EGA - evolved gas analysis

In parallel with the thermal behavior study and stoichiometry determination by TGA-DSC, we also monitored the gaseous products from thermal decomposition in air and nitrogen atmospheres through a TGA-DSC/FT-IR system, so that in both atmospheres the same products were detected. However, as previously mentioned, the monitoring of gaseous products is more advantageous in an inert atmosphere because the amount of CO and CO_2 produced from the organic matter decomposition is lower, i.e., inherent only to the ligand decarboxylation. The combination of these results now offers us the possibility of obtaining a set of complementary information about the complexes that can be used to evaluate the likely thermal decomposition mechanism those complexes follow.

The gaseous products of the thermal decomposition of the complexes [La(DMBz)$_3$] and [Ce(DMBz)$_3$] in anhydrous form, Fig. 3 (a–d), were continuously monitored between 30 and 1000 °C (TGA). The experimental FT-IR spectra obtained were compared with literature data [33,34] as well as evaluated and compared through OMNIC® software with a broad spectral library of gaseous products. The bands identified in FT-IR spectra (numbered 1–6), Fig. 3(a–d), are also associated with illustrations of the possible position of fragmentation in the molecule of the ligand (1*, 2*, 3* and 4*). Among the products monitored under air atmosphere, observed in a relatively larger quantity, the fragments of two groups released simultaneously in the first mass loss steps (TGA) up to 360 °C stand out, which are methanol (CH_3OH), with peaks at 1008, 1033 e 1062 cm^{-1} originating from methoxy groups, and carbon dioxide (CO_2), Fig. 3(a), with characteristic peaks in doublet form at 2360, 2400 cm^{-1} and 666 cm^{-1}, assigned to the decarboxylation of the carboxylate group. In addition to these two main fragments, there is also the presence of peaks of very small intensity, inherent to fragments of dimethoxybenzene ($C_8H_{10}O_2$) with bands at 1046, 1150, 1202, 1286, 1486 and 1594 cm^{-1}, and methoxybenzene (C_7H_8O) with bands at 1054, 1254, 1498, 1602 cm^{-1} and 1062 cm^{-1}, as shown in Fig. 3 (b, c). From 360 °C, an increase in the proportion of CO_2 in relation to the other products is observed, so that from the slow mass losses steps at 401 °C (La) and 381 °C (Ce), Fig. 3(d), only methane (peaks at 2995 and 3018 cm^{-1}) and carbon dioxide (CO_2) are observed in the FT-IR spectra. Possibly, most of the gaseous products CH_4 and CO_2 originate from the fragmentation of the carbon skeleton.

The monitoring in nitrogen atmosphere, slightly different from that observed in air atmosphere, initially shows methanol as the only product released and, as mentioned earlier, it comes from the methoxy group of the ligand. This process occurs almost simultaneously with decarboxylation, Fig. 3(a), a coherent attribution because the atmosphere used was inert (N_2). Subsequently, with the increase in temperature, intense peaks attributed to fragments of dimethoxybenzene and methoxybenzene are observed, Fig. 3(b, c), which continue to be released in decreasing proportion until the end of this step together with fragments of methanol and carbon dioxide. The slow mass loss steps, for both compounds, starting at 439 °C (La) and 416 °C (Ce), show peaks for the fragments only in the 3000 cm^{-1} region, corresponding to C—H group stretching that may indicate the presence of different sizes of carbon chain. Furthermore, it is more likely that these fragments originated from the aromatic skeleton, since it was not possible to observe bands related to benzene in the FT-IR spectra, considering the monitoring between 30 and 1000 °C performed for both compounds.

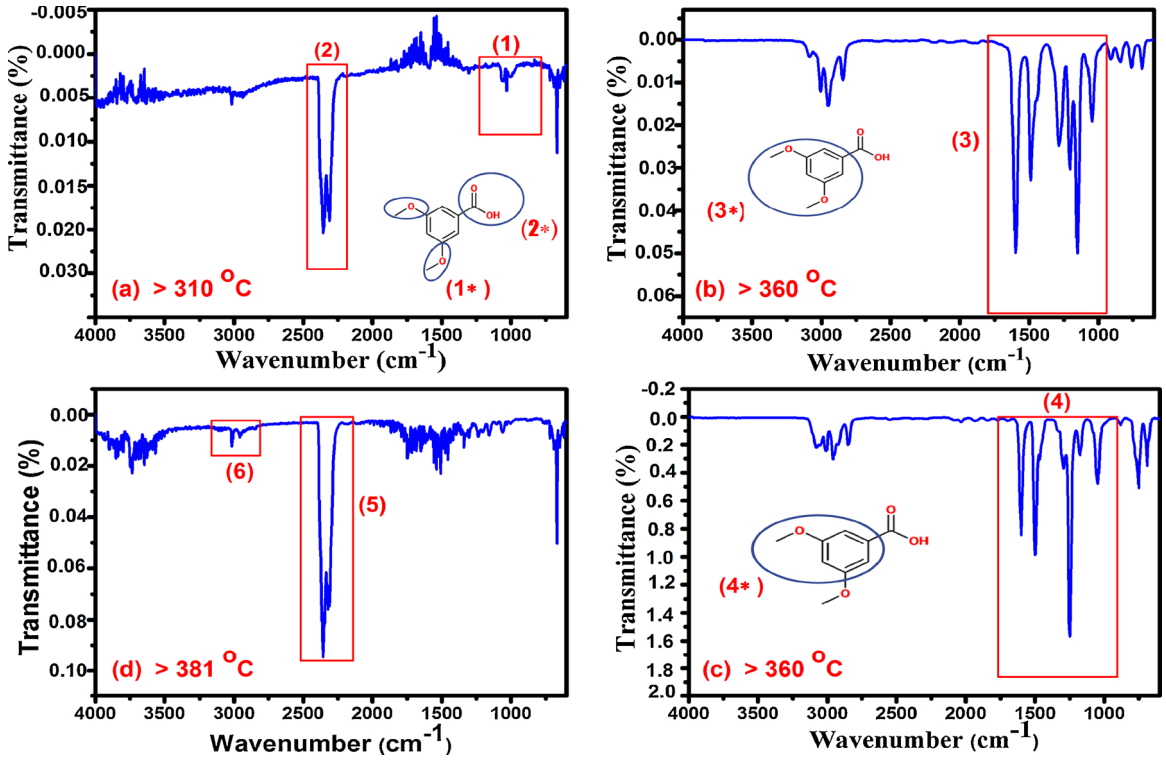

Fig. 3. a–d). FT-IR spectra of the main gaseous products monitored in air and N_2 atmospheres from the thermal decomposition of the complexes [La(DMBz)$_3$·2H$_2$O] and [Ce(DMBz)$_3$] at the temperatures (TGA): (a) > 310 °C (b and c) > 360 to 400 °C and (d) above 381 °C. DMBz: 3,5-dimethoxybenzoate.

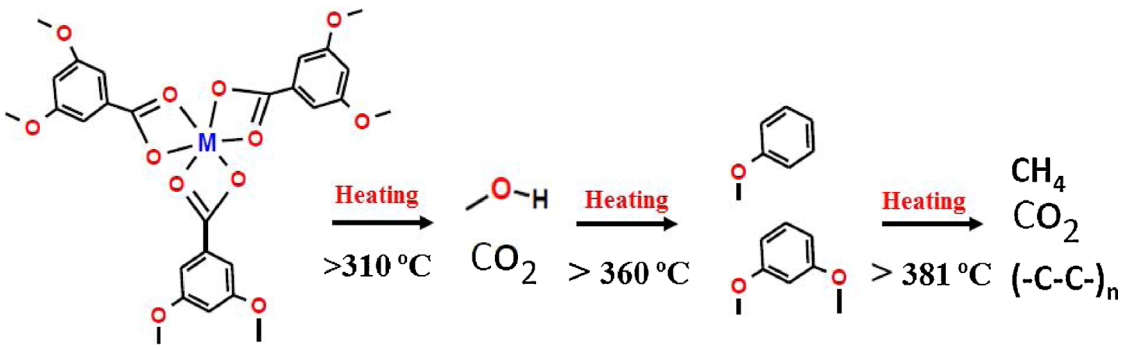

Fig. 4. Illustration based on the most products released, for the main path thermal decomposition follows in lanthanum and cerium 3,5-methoxybenzoate complexes, monitored by TGA-DSC / FT-IR in air and nitrogen atmospheres.

This statement can be made due to the absence of characteristic bands of benzene, located in 1802 and 1950 cm^{-1}. From these data, it was possible to qualitatively suggest, based on the gaseous products released in greater quantity, the main way in which fragmentation occurs, as shown in simplified form in Fig. 4.

3.2. Structural study

3.2.1. Infrared spectroscopy: theoretical and experimental

The experimental and theoretical FT-IR spectra for the ligand salt and lanthanum complex, as representatives of both complexes, are shown in Fig. 5 due to similarity of spectra. The optimized structures used to generate the theoretical vibrational spectra are shown in the supplementary material, Fig. S2. The identification of the main bands in the FT-IR spectra, Table 2, was performed from the spectroscopic correlations by computational animations and by checking the level of correspondence with the FT-IR experimental data. As it can be observed in Fig. 5, the positions of the main bands between the theoretical (a*, b*) and experimental (a, b) spectra are highly concordant, suggesting that the proposed structures are very close to the real structure. However, due to the approximate nature of the computational technique, small differences observed were expected, since the theoretical calculations do not include harmonic effects in the infrared vibrations, besides the complexes have been considered in the gaseous phase for the calculations [35]. In this work, as the experimental infrared spectra of the complexes are very similar, that allows us to state that the coordination occurs equally for both compounds.

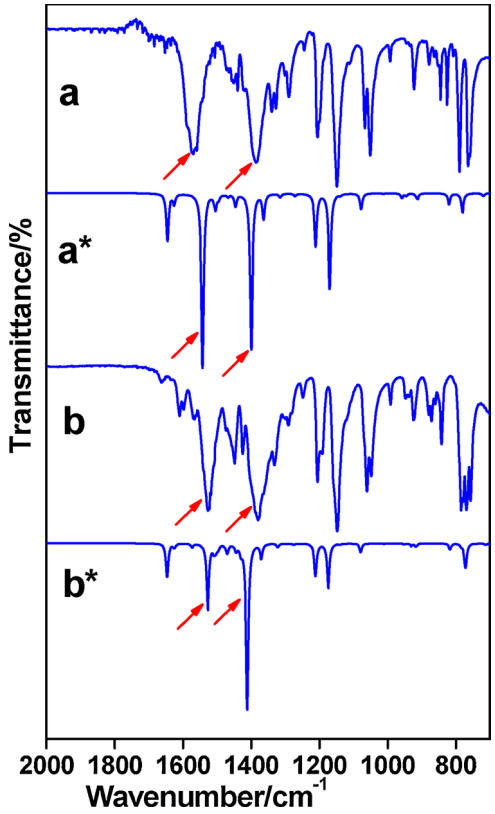

Fig. 5. Experimental FT-IR spectra of the 3,5-dimethoxybenzoate sodium salt (a) and lanthanum complex (b), correlated to the FT-IR theoretical spectra of 3,5–dimethoxybenzoate sodium salt (a*) and lanthanum complex (b*). The lanthanum complex was used as representative of cerium complex due to their similarity.

Table 2
Experimental and theoretical FT-IR data assigned to the 3,5-dimethoxybenzoate salt and lanthanum 3,5-dimethoxybenzoate complex as representative of all complexes.

Assignment	NaDMBz		$[La(DMBz)_3{\cdot}2H_2O]$	
	Exp.	Theor.	Exp.	Theor.
ν C = C (ring)	1653_w, 1340_m	1645, 1363	1610_m, 1331_m	1646, 1371
δ CH_3 + δ C– H (ring) + ν C–OCH_3	1205_s, 1148_s	1211, 1170	1202_m, 1148_s	1211, 1174
ν_{asym} COO–	1561_s	1542	1526_s	1527
ν_{sym} COO–	1385_s	1399	1381_s	1412
$\Delta\nu$ (ν_{asym} – ν_{sym})	176	157	145	115

ν: stretching vibration; δ: bending vibration; asym: asymmetrical; sym: symmetrical; w: weak; m: medium; S: Strong; Theor.: Theoretical; Exp.: Experimental; DMBz: 3,5–dimethoxybenzoate.

In order to study the coordination mode of the carboxylate groups to the metal centers, as indicated by the experimental and theoretical calculation results, the methodology described by Deacon and Phillips [36] was applied. The differences between the symmetric and asymmetric stretching values for carboxylate groups of complexes and the ionic compound (sodium salt) were compared. From the combined results, presented in Table 2, it can be suggested that the carboxylate group is coordinated to the lanthanide ions by bidentate chelating mode [33–35]. In addition to the complexation study by FT-IR data, further X-ray powder diffraction is intended to provide accurate structural information on the crystalline structures.

3.3. Crystalline structure

In the absence of suitable single crystals, the complexes were previously characterized by thermogravimetry and simultaneous differential scanning calorimetry (TGA-DSC) to determine stoichiometric ratio and thermal stability. From this data, the structural arrangement was determined using X-ray powder diffraction after dehydration of lanthanum compound at 200 °C.

Table 3
Principal data of crystalline parameters obtained for [Ce(DMBz)$_3$] and [La(DMBz)$_3$] complexes.

	[Ce(DMBz)$_3$]	[La(DMBz)$_3$]
Empirical formula	$C_{27}H_{27}O_{12}Ce$	$C_{27}H_{27}O_{12}La$
Formula weight (gmol^{-1})	683.61	682.40
T(K)	298	298
λ(CuKα) (Å)	1.5418	1.5418
Crystal system	Monoclinic	Monoclinic
Space group	$P2_1/c$	$P2_1/c$
a(Å)	14.829(8)	14.790(1)
b,(Å)	24.351(2)	24.294(3)
c(Å)	7.7758(1)	7.836(2)
$\alpha=\gamma$ (°)	90	90
β (°)	97.85(6)	98.16(1)
V (Å^3)	2775.2(4)	2787.0(9)
Z	4	4
d_{calc}(g cm^{-3})	1.636(2)	1.626(5)
μ (mm^{-1})	13.2(8)	12.4(4)
Number of parameters	78	73
R_{Bragg}, R_{wp}	0.069 / 0.0106	0.0359 / 0.0827

Table 4
Main Ln-O bond lengths of oxygen atoms around lanthanide ions (Ln).

[Ce(DMBz)$_3$]			
Lengths/Å			
O11	2.420(2)	O31	2.597(2)
O12	2.618(3)	O32	2.459(3)
O21	2.466(2)	O32^{i}	2.718(1)
O22	2.629(3)		
[La(DMBz)$_3$]			
O11	2.501(5)	O31	2.541(2)
O12	2.585(3)	O32	2.394(3)
O21	2.232(3)	O11^{i}	2.733(2)
O22	2.648(3)		

The crystal structure models of the [La(DMBz)$_3$] and [Ce(DMBz)$_3$] complexes in anhydrous form were solved using state-of-the-art powder diffraction data measured in conventional laboratory equipment. In order to solve the present crystal structures, a rigid body for organic moiety and a high number of parameters were extensively used. After a long procedure as described before, very important crystallochemical information could be afforded and the crystallographic parameters of both complexes were summarized in Table 3, while the eight oxigen-lanthanides bond distances present in the coordination sphere of cerium and lanthanum are given in Table 4. The molecular structure of both complexes, drawn using OLEX2 [37], are shown in Fig. 6(a, b), as well as the overall packing and hydrogen bond are presented in Figures S3 (a–d) and S4 (a–e) as supplementary material. The DMBz is a carboxylate ligand and there are three coordination modes for carboxylate ligands [16,17]. The bidentate chelating (mode a) is easily described as both oxygen atoms bonded to the same lanthanide ion. Another coordination mode is when a lanthanide ion carboxylate forms a monoatomic bridge or μ-oxo bridge (mode b). The third mode is when each oxygen in a carboxylate group binds to a different lanthanide ion, syn, syn-η1:η1:μ2 bidentate bridging fashion.

As described in Fig. 6(a, b), both structures show two ligands bonded to lanthanide ions through the carboxylate group in mode a and b only the other DMBz ligand is coordinated to lanthanide ion in mode b. Besides the lanthanide-oxigen bond lengths, both complexes also exhibit important and strong interaction, that is, 3.879 Å and 3.944 Å, between Ce-Ce and La-La metal ions respectively.

In the supplementary material, Figures S3 and S4 show the main hydrogen bonds for the [Ce(DMBz)$_3$] and [La(DMBz)$_3$] complexes, respectively. For [La(DMBz)$_3$], there are intramolecular H-bonds between H11 and H21 with O21, H31 and H38b with O31 and O32 with H21 and two other intermolecular H-bonds between H33…O64 and H13…O63. Similarly, H-bonds fashion are observed in [Ce(DMBz)$_3$], where the two intermolecular H-bonds are assembled by O31…H31 and O54…H18a and the intramolecular ones are located between O12…H21 and O31…H31.

3.4. UV–vis absorption study

For both complexes studied, the electronic experimental spectra recorded in DMF solution show a single absorption band that reaches its maximum at 298 nm. For the DFT calculations, unfolding in two bands of different intensities in the UV–vis spectra is observed; an intense band at 255 nm and a lower intensity one at 300 nm, as shown in Fig. 7, so that such differences may probably be due to experimental conditions like complex-solvent interaction or even by limitation of the monochromator system (bandpass limitation) in the equipment used. In addition, for the theoretical calculations a single molecule, free of interactions, is taken into account.

From HOMO → LUMO orbital transitions, Fig. S5, it is noticed that

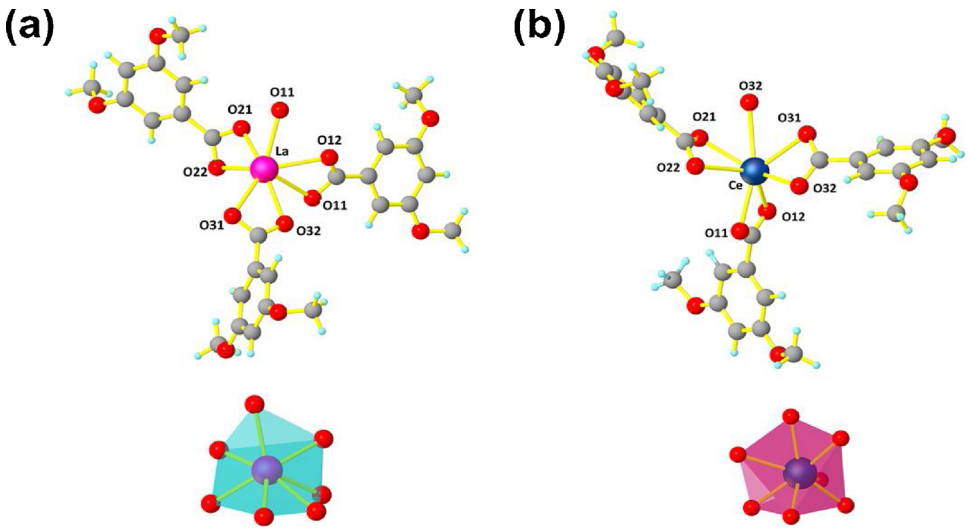

Fig. 6. (a, b). Asymmetric units and distorted pentagonal bipyramidal geometry around (a) La^{3+} and (b) Ce^{3+} respectively. Ln-O bonds are represented in both structures, whereas Ln represents La^{3+} and Ce^{3+} lanthanide ions.

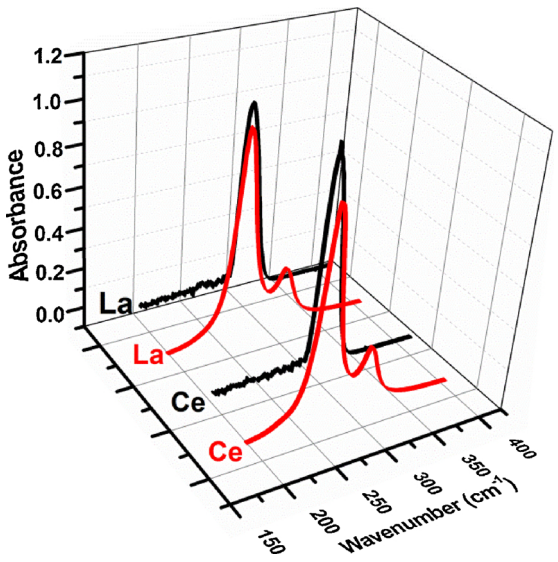

Fig. 7. Absorption spectra in UV–vis (experimental: black; theoretical: red) for the $[La(DMBz)_3{\cdot}2H_2O]$ and $[Ce(DMBz)_3]$ complexes. DMBz: 3,5-dimethoxybenzoate (For interpretation of the references to colour in this figure legend, the reader is referred to the web version of this article).

the charge density on the organic part of the complex is due to π-π* and n-π* transitions, the latter being usually of low intensity. According to literature, π-π* transitions for organic ligands are recorded in the region between 196 and 313 nm and correspond to the C═C chromophore group of aromatic ring [38]. The overlapped band in the UV–vis experimental data, apparent at 300 nm in the theoretical calculation, is probably due to n-π* transitions. Regarding the charge transfer on the metal complexes, the overlapping of oxygens p-orbital of the carboxylate group (Fig. S5) should have favored the interligand charge transfer like in HOMO + 1 → LUMO (74 %), HOMO + 2 → LUMO (89 %) for lanthanum and HOMO + 1 → LUMO (69 %), HOMO + 2 → LUMO (89 %) for cerium. The main contributions of UV–vis radiation absorption occur through the aromatic system and the carboxylate group interactions, although singlet states of charge transfer of ligand-metal can also contribute. Anyway, those contributions are discussed in the fluorescence section.

3.5. Fluorescence study

The molecular orbitals (HOMO/LUMO) with the highest probability of charge transfer on the 3,5-dimethoxybenzoate lanthanum and cerium complexes were obtained by Time-Dependent Density Functional (TD-DFT) Theory. However, lanthanum (III) ion, in contrast to other lanthanide ions, is theoretically non-fluorescent because of its $3d^{10}4f^{\circ}$ electronic configuration, so only the fluorescence for the cerium complex is discussed in this section. The emission (fluorescence) of the Ce (III) results from 4f-5d optical transitions, which gives rise to much more intense bands than intraconfiguration transitions of 4f-4f type and the emission is generally observed in the ultraviolet region, although it may also occur in the visible region [39].

In Fig. 8(a, b), the major HOMO →LUMO orbitals contributions and experimental excitation and emission spectra are shown, which are correlated with each other to identify the electronic transitions responsible for the system's fluorescence. The H-1(93 %) and H-2(98 %) → L + 3 transitions (Fig. 8(a)) show that there is one ligand-metal charge transfer (LMCT), as well as contributions of intraligand charge transfer (ILCT and LMCT) originated from a mixture of transitions H-1(69 %); H-2 (88 %); H-4 (93 %) and H-5 (86 %) → LUMO. The contributions ILCT and LMCT, especially the LMCT, can be justified since the orbital of the organic part of the molecule has also charge distribution on the metallic center. In addition, from the experimental and theoretical data (Fig. 8(a,b)) and summary in Table S2), we have not excluded the possibility of ligand-ligand charge transfer (LLCT) as a function of this overlapping of orbitals on the metallic center.

The excitation and emission spectra, Fig. 8(b), were obtained respectively by monitoring of λ_{max} at 310 nm and λ_{max} emission at 355 nm. Hence, the emission band in the spectrum observed at 355 nm is an overlapping (summation) of n-π* and π-π* transitions of the ligand, as well as LMCT contributions from the antenna effect, transitions attributed to energy levels of the Ce(III) metal center $^2F_{7/2} \rightarrow {}^2F_{5/2}$.

4. Conclusions

The lanthanum(III) and cerium(III) complexes using a monocarboxylate ligand, 3,5-methoxybenzoate, were synthesized in aqueous medium and characterized in the solid state or solution by thermoanalytical methods, X-ray diffraction, FT-IR and UV–vis.

Based on the thermoanalytical data from the TGA-DSC curves, it was possible to define the stoichiometric ratio of the synthesized complexes as $M(DMBz)_3$, where M represents the lanthanides and DMBz the 3,5-dimethoxybenzoate ligand. Among the complexes synthesized and characterized, only that of lanthanum was obtained in hydrated form. A probable explanation can be attributed to the lower lanthanide contraction effect for lanthanum, which would make the coordination sphere more available. Another relevant information from TGA-DSC/DTG to the study of these materials was the thermal stability, decomposition temperatures, as well as the temperature of formation of the

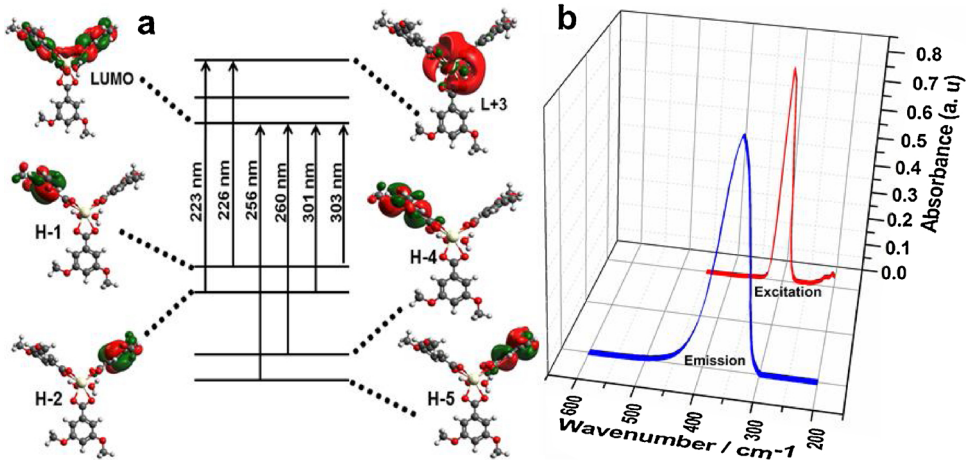

Fig. 8. (a) Molecular orbitals for $[Ce(DMBz)_3]$ according to the TD-DFT calculations, (b) excitation and emission spectra in. UV–vis.

final residue used in the calculation of stoichiometry and the monitoring, by TGA/FT-IR, of the main volatile products related to thermal decomposition and consequently the probable path thermal decomposition follows.

From FT-IR spectroscopic data, it can be suggested that the 3,5-dimethoxybenzoate monocarboxylate ligand coordinates with lanthanide ions in chelating form, while by X-ray diffractograms with Rietveld refinement, it was possible to establish that the monocarboxylate ligand coordinates both in chelating and bridge forms. The result of this coordination mixture generated polymeric and practically isomorphic structures for the complexes, defined as $[M(DMBz)_3]n$ with a monoclinic system of space group $P2_{1/c}$. For cerium(III) complex, through UV–vis absorption calculations using the TD-DFT theory, it was possible to suggest that the charge transfer orientations, according to HOMO and LUMO orbitals, occur by antenna effect of the ligand for $^2F_{7/2}$ and $^2F_{5/2}$ energy levels of the metal ion.

In summary, it is concluded that monocarboxylate ligands can also generate polymeric structures with lanthanide ions as shown in this study. In this sense, it is possible that certain properties, such as those of fluorescence, are altered depending on the type of coordination and/or crystalline structure, as well as on the experimental conditions of synthesis employed. However, this study limited itself to the synthesis, elucidation of the stoichiometry and crystalline structure of the complexes obtained in crystalline powder form.

Declaration of interests

The authors declare that they have no known competing financial interests or personal relationships that could have appeared to influence the work reported in this paper.

Acknowledgements

The authors thank the Brazilian Foundations CNPQ (grant nº 434138/2018-5), FUNDECT, CAPES and FINEP (Contract: 04.13.0448.00/2013) for financial support, and are grateful to Professor Massao Ionashiro for allowing us to carry out measurements in the Ivo Giolito Thermal Analysis Laboratory (LATIG) – UNESP. Daniel M. Brasil and Leandro M. C. Pinto acknowledge CENAPAD–SP (Centro Nacional de Processamento de Alto Desempenho em São Paulo) for granting computing time and Professional Noemi Marques de Carvalho for English reviewing.

Appendix A. Supplementary data

Supplementary material related to this article can be found, in the online version, at doi:https://doi.org/10.1016/j.tca.2020.178662.

References

[1] C.T. Carvalho, G.F. Oliveira, J. Fernandes, A.B. Siqueira, E.Y. Ionashiro, M. Ionashiro, Rare-earth metal compounds with a novel ligand 2-methoxycinnamylidenepyruvate: a thermal and spectroscopic approach, Thermochim. Acta 637 (2016) 17–23, https://doi.org/10.1016/j.tca.2016.05.008.

[2] A.L.C.S. do Nascimento, J.A. Teixeira, W.D.G. Nunes, F.X. Campos, O. Treu-Filho, F.J. Caires, M. Ionashiro, Thermal behavior, spectroscopic study and evolved gas analysis (EGA) during pyrolysis of picolinic acid, sodium picolinate and its light trivalent lanthanide complexes in solid, J. Anal. Appl. Pyrolysis 119 (2016) 242–250, https://doi.org/10.1016/j.jaap.2016.01.010.

[3] W. Ferenc, A. Walków-Dziewulska, J. Chruciel, Spectral and thermal behaviours of rare earth element complexes with 3,5-dimethoxybenzoic acid, J. Serb. Chem. Soc. 68 (2003) 751–763.

[4] J. sienkiewicz-gromiuk, I. Rusinek, L. Kurach, Z. Rzaczynka, Thermal and spectroscopic \(I.R., XPS) properties of lanthanide(III) benzene-1,3,5-triacetate complexes, J. Therm. Anal. Calorim. 126 (2016) 327–342, https://doi.org/10.1007/s10973-016-5521-8.

[5] R. Decadt, K.V. Hecke, D. Depla, K. Leus, D. Weinberger, I.V. Driessche, P.V. Der Voort, R.V. Deun, Synthesis, crystal structures, and luminescence properties of carboxylate based rare-earth coordination polymers, Inorg. Chem. 51 (2012) 11623–11634, https://doi.org/10.1021/ic301544q.

[6] Z. Ling-Yan, R. Li, L. Li-Wei, W. Li-Na, Synthesis, structure, and character of two rare earth carboxylic acid complexes, J. Coord. Chem. 70 (2017) 4008–4018, https://doi.org/10.1080/00958972.2017.1415431.

[7] J.-Ru Zheng, N. Ren, Jian-Jun Zhang, Da-Hai Zhang, Li-Zhen Yan, Shu-Ping Wang, Crystal structures, luminescence, and thermodynamic properties of lanthanide complexes with 3,5-dimethoxybenzoic acid and 1,10-phenanthroline, J. Chem. Thermodyn. 57 (2013) 169–177, https://doi.org/10.1016/j.jct.2012.08.015.

[8] Yan-Zu Du, Jin-Min Zheng, Syntheses, structures and magnetic properties of a series of lanthanide complexes based on p-methoxybenzoic acid, Inorg. Chem. Commun. 66 (2016) 59–63, https://doi.org/10.1016/j.inoche.2016.01.020.

[9] Xiao-Xia Qi, Wu Jun-Chen, NingRen, Chun-Li Zhao, Jian-Jun Zhang, Guang-Cai Zong, Jie Gao, Novel lanthanide complexes constructed from 3,4-dimethoxybenzoic acid: crystal structures, spectrum and thermochemical properties, Thermochim. Acta 615 (2015) 1–7, https://doi.org/10.1016/j.tca.2015.07.003.

[10] K.V. Tenório, J.A. Teixeira, L.M.C. Pinto, F.J. Caires, O. Treu-Filho, F.A. Santos, T.A.D. Colman, A. Cuin, C.T. Carvalho, Synthesis and structure of a praseodymium (III) complex with carboxylate ligand: a thermal and spectroscopic study, J. Rare Earths (2018) 1–8, https://doi.org/10.1016/j.jre.2018.03.019.

[11] A.A. Coelho, Indexing of powder diffraction patterns by iterative use of singular value decomposition, J. Appl. Cryst. 36 (2003) 86–95, https://doi.org/10.1107/S0021889802019878.

[12] (TOPAS-R). Version 4.2, General Profile and Structure Analysis Software for Powder Diffraction Data (Bruker AXS, Karlsruhe, Germany), 2009.

[13] G.S. Pawley, Unit–cell refinement from powder diffraction scans, J. Appl. Cryst. 14 (1981) 357–361, https://doi.org/10.1107/S0021889881009618.

[14] A.L. Spek, Structure validation in chemical crystallography, Acta Cryst. 65 (2009) 148–155, https://doi.org/10.1107/S090744490804362X.

[15] A.A. Coelho, Whole-profile structure solution from powder diffraction data using simulated annealing, J. Appl. Cryst. 22 (2000) 899–908, https://doi.org/10.1107/S002188980000248X.

[16] D.E. Lynch, G. Smith, K.A. Byriel, C.H.L. Kennard, 3,5–dimethoxybenzoic acid and the second polymorph of the 2:1 adduct of 3,5-dinitrobenzoic acid with ethylenediamine, Acta Cryst. 50 (1994) 1259–1262, https://doi.org/10.1107/S0108270193012259.

[17] L.F. Marques, A. Cuin, G.S.G. de Carvalho, M.V. dos Santos, S.J.L. Ribeiro, F.C. Machado, Energy transferprocess in highly photoluminescent binuclear hydrocinnamate of europium, terbium 1,10-phenanthroline as ancillary ligand, Inorg. Chim. Acta Rev. 441 (2016) 67–77, https://doi.org/10.1016/j.ica.2015.11.009.

[18] T.C. de Oliveira, H.P. Santos, M.G. Lahoud, D.F. Franco, R.O. Freire, J.D.L. Dutra, A. Cuin, J.F. de Lima, L.F. Marques, Elucidating the energy transfer process in mononuclear and binuclear lanthanide complexes of the anti-inflammatory drug ibuprofen: From synthesis to high luminescence emission, J. Lumin. 181 (2017) 196–210, https://doi.org/10.1016/j.jlumin.2016.09.024.

[19] R.A. Young, The Rietveld Method. (IUCr Monograph No 5), Oxford University Press, New York, 1981.

[20] A.D. Becke, Thermochemistry. III. The role of exact exchange, J. Chem. Phys. 98 (1993) 5648–5652, https://doi.org/10.1063/1.464913.

[21] C. Lee, W. Yang, R.G. Parr, Development of the Colle-Salvetti correlation-energy formula into a functional of the electron density, Phys. Rev. B 37 (1988) 785, https://doi.org/10.1103/PhysRevB.37.785-789.

[22] M.J. Frisch, G.W. Trucks, H.B. Schlegel, G.E. Scuseria, M.A. Robb, J.R. Cheeseman, G. Scalmani, V. Barone, et al., Gaussian 09, Revision A.02, Gaussian, Inc., Wallingford CT, 2009.

[23] D.Z. Goodson, S.K. Sarpal, P. Bopp, M. Wolfsberg, Influence on isotope effect calculations of the method of obtaining force constants from vibrational data, J. Phys. Chem. 86 (1982) 659–663, https://doi.org/10.1021/j100394a014.

[24] J. Bertrán, I.G. Csizmadia, New Theoretical Concepts for Understanding Organic Reactions, first ed., Springer, Netherlands, 1989, https://doi.org/10.1007/978-94-009-2313-3.

[25] R. Dennington, T. Keith, J. Millam, Gauss View. Shawnee Mission, Semichem. Inc., Version 5.0.8, KS, 2009.

[26] F. Weigend, R. Ahlrichs, Balanced basis sets of split valence, triple zeta valence and quadruple zeta valence quality for H to Rn: design and assessment of accuracy, Phys. Chem. Chem. Phys. 7 (2005) 3297–3305, https://doi.org/10.1039/B508541A.

[27] M. Dolg, H. Stoll, A. Savin, H. Preuss, Energy-adjusted pseudopotentials for the rare earth elements, Theor. Chim. Acta 75 (1989) 173–194, https://doi.org/10.1007/BF00528565.

[28] M. Dolg, H. Stoll, H. Preuss, A combination of quasirelativisticpseudopotential and ligand field calculations for lanthanoid compounds, Theor. Chim. Acta 85 (1993) 441–450.

[29] F. Neese, The ORCA program system, Wiley Interdisc. Rev. – Comput. Mol. Sci. 2 (2012) 73–78, https://doi.org/10.1002/wcms.81.

[30] M.D. Hanwell, D.E. Curtis, D.C. Lonie, T. Vandermeersch, E. Zurek, G.R. Hutchison, Avogadro: an advanced semantic chemical editor, visualization, and analysis platform, J. Cheminformatics. (2012) 1–17, https://doi.org/10.1186/1758-2946-4-17.

[31] C.F. Almeida, R.C. Andrade, L.W. Aguiar, F.J. Caires, E.A. Falcão, C.T. Carvalho, Thermal and spectroscopic study of the lanthanide 2-aminoterephthalate compounds in the solid state, J. Therm. Anal. Calorim. 117 (2014) 251–258, https://doi.org/10.1007/s10973-014-3721-7.

[32] P. Janoš, T. Hladík, M. Kormunda, J. Ederer, M. Šťastný, Thermal Treatment of Cerium Oxide and Its Properties: Adsorption Ability Versus Degradation Efficiency, (2014), https://doi.org/10.1155/2014/706041.

[33] R.M. Silverstein, F.X. Webster, D.J. Kiemle, Spectrometric Identification of Organic Compounds, 7th ed., John Wiley & Sons, Hoboken, 2005.

[34] K. Nakamoto, Infrared and Raman Spectra of Inorganic and Coordination

Compounds, 4th ed., Wiley, New York, 1986.
[35] J.G. Smith, Chapter 13 mass spectrometry and infrared spectroscopy, Organic Chemistry, 3rd ed., McGraw-Hill, New York, NY, 2011.
[36] G.B. Deacon, R.J. Phillips, Relationships between the carbon-oxigen stretching frequencies of carboxylate complexes and the type of carboxylate coordination, Coord. Chem. Rev. 33 (1980) 227–250, https://doi.org/10.1016/S0010-8545(00)80455-5.
[37] O.V. Dolomanov, L.J. Bourhis, R.J. Gildea, J.A.K. Howard, H. Puschmann, OLEX2: a complete structure solution, refinement and analysis program, J. App. Cryst. 42 (2009) 339–341, https://doi.org/10.1107/S0021889808042726.
[38] Heinz-Helmut Perkampus, UV-VIS Spectroscopy and Its Applications, Ed., Springer Science & Business Media, 2013.
[39] S.V. Eliseeva, J.C.G. Buunzli, Rare earths: jewels for functional materials of the future, New J. Chem. 35 (2011) 1165–1176, https://doi.org/10.1039/c0nj00969e.